Understanding the Impacts of ENSO Patterns on Droughts over Southern Africa using SPEEDY

Michelle Jacqueline Gore

Dissertation presented for the degree of Master of Science

In the Department of Environmental and Geographical Science

University of Cape Town

Supervisor: Assoc. Prof. Babatunde Abiodun

February 2019

Declaration

1. I know that plagiarism is wrong. Plagiarism is to use another's work and pretend that it is one's own.
2. I have used the Harvard convention for citation and referencing. Each contribution and quotation in this dissertation from the works of other people has been attributed and has been cited and referenced.
3. This dissertation is my own work.
4. I have not allowed, and will not allow, anyone to copy this work with the intention of passing it off as his or her own.

Signature: Signed by candidate

Name: Michelle Gore

Student No: GRXMIC001

Date: 10 February 2019

Acknowledgements

There are several people who I would like to thank for helping me through this journey. First and foremost, I would like to thank my supervisor, Assoc. Prof. Babatunde Abiodun, for his consistent support and guidance throughout my Master's degree. I truly appreciate the time he took to ensure that my best interests and wellbeing were a priority as well as the invaluable and vast knowledge he shared in the project. He always managed to simplify challenging concepts and tasks, making them more manageable.

I am also grateful for the financial support from the Alliance for Collaboration on Climate and Earth Systems Science (ACCESS) and the National Research Foundation (NRF), without which this degree would not have been possible. I would also like to extend my gratitude to Dr. Fred Kucharski and the International Centre for Theoretical Physics in Italy, for making SPEEDY available to me and for providing technical support and guidance. I would like to thank Philip Mukwenha as well for always making himself available to assist in any technical related issues, no matter how small.

I would like to thank my fellow postgraduate students, particularly those who were part of the weekly peer review meetings. The constant motivation went a long way in helping me to refine my work. Finally, I would like to thank my parents and family for always supporting me and believing in my abilities.

Abstract

The El Niño Southern Oscillation (ENSO) is a major driver of southern Africa droughts, but the nonlinearity of ENSO variation inhibits accurate prediction of droughts. While studies have identified multiple patterns of ENSO, most drought predictions over southern Africa are still based on only two ENSO patterns. This study examines the relationship between southern African droughts and eight ENSO patterns: four El Niño SST conditions (EN1 - EN4) and four La Niña SST conditions (LN1 - LN4). In this study we analyzed multi-forcing ensemble simulations from SPEEDY (a general circulation model from the International Centre for Theoretical Physics) and used two drought indices (SPEI: Standardized Precipitation Evapotranspiration Index; SPI: Standardized Precipitation Index) to characterize drought. The capability of SPEEDY in reproducing southern Africa climate was evaluated by comparing the historical simulations (1979-2008) with the Climate Research Unit (CRU) observation. To obtain the influence of ENSO patterns, we forced the SPEEDY simulations with SST of each ENSO pattern, analyzed the impacts on the simulated drought indices (SPEI and SPI), and studied the atmospheric dynamics that link each ENSO pattern to southern Africa droughts.

The results show that SPEEDY generally captures the temporal and spatial distribution of climate variables over southern Africa well, although with warm and wet biases across the region. However, in most cases, these results are comparable with those from more complex atmospheric models. In agreement with previous studies, the results show that El Niño SST conditions weaken the Walker circulation and cause drier conditions over parts of southern Africa, whilst La Niña SST conditions strengthen the Walker Circulation and cause wetter conditions. However, the results show that the differences in the El Niño SST conditions (EN1 - EN4) alter the circulation, thereby influencing the spatial pattern and intensity of drought over the region. For instance, while EN2 induces the most severe drought in the tropical area, EN4 produces it in the southwestern region, because the two patterns feature different characteristics of anticyclonic moisture flux over southern Africa. The same is true of the La Niña SST conditions. Although, LN1 and LN4 show wet conditions across the southern part of the region, LN1 produces drought in the northern part, while LN4 induces it along the western coast. Hence, this study shows that accounting for the differences in El Niño (or La Niña) conditions may improve drought predictions in southern Africa.

List of Figures

List of Tables

List of Abbreviations

AAO	Antarctic Oscillation
CAM5	Community Atmospheric Model version 5
CMB	Climate Moisture Balance
CRU	Climate Research Unit
ENSO	El Niño Southern Oscillation
GCM	General Circulation Model / Global Climate Model
HadGEM3	Hadley Centre Global Environment Model version 3
ICTP	International Centre for Theoretical Physics
IOD	Indian Ocean Dipole
ITCZ	Intertropical Convergence Zone
MEI	Multivariate ENSO Index
MJO	Madden Julian Oscillation
MSLP	Mean Sea Level Pressure
PDSI	Palmer Drought Severity Index
PET	Potential Evapotranspiration
RCM	Regional Climate Model
SADC	Southern Africa Development Community
SAM	Southern Annular Mode
SICZ	South Indian Convergence Zone
SIOD	Subtropical Indian Ocean Dipole
SPEEDY	Simplified Parameterizations, primitivE-Equation DYnamics
SPEI	Standardized Precipitation Evapotranspiration Index
SPI	Standardized Precipitation Index
SST	Sea Surface Temperature
TTT	Tropical Temperate Trough

Table of Contents

Chapter 1: Introduction

1.1 Southern Africa

Southern Africa is broadly defined as the southernmost region of Africa, however, there are variations in the precise definition concerning the countries which constitute this region. The United Nations (UN) consider the region to include Botswana, Eswatini (formerly Swaziland), Lesotho, Namibia and South Africa, whilst the African Union extend their definition also to include Angola, Malawi, Mozambique, Zambia and Zimbabwe. On the other hand, the Southern African Development Community (SADC) consists of 16-member states, including the above-mentioned countries as well as the Democratic Republic of Congo (DRC), Tanzania and the island nations, Comoros, Madagascar, Mauritius and Seychelles. For this study, southern Africa will be defined as the African region which lies south of the equator.

Southern Africa is bounded by the Atlantic Ocean to the west and the Indian Ocean to the east. The cool Benguela current flows along the western coast, while the warm Agulhas current flows along the eastern and southern coast. The topography of southern Africa is dominated by a high-lying central plateau in the interior of the region with an altitude of 1000m - 1600m. Steep slopes, known as the Great Escarpment, connect the plateau to lower lying coastal plains in Angola, Namibia, South Africa and Mozambique. The Great Escarpment is most prevalent in the southeastern region which consists of the Drakensberg Mountain Range with peaks exceeding 2000m in Lesotho. There is also complex topography in the eastern equatorial region which forms part of the mountain ranges associated with the East African Rift, including Mount Kilimanjaro and Mount Kenya. There are two notable deserts in southern Africa, the Namib Desert and the Kalahari Desert. The Namib Desert is an extremely dry and narrow region located along the coast of Namibia, whilst the Kalahari Desert is located within a depression in the central plateau, extending over the majority of Botswana and parts of South Africa and Namibia.

1.2 Southern Africa Climate

The climate of southern Africa is characterised by high spatio-temporal rainfall variability and moderate temperatures. There is a meridional rainfall gradient across the region, with highest rainfall amounts in the humid tropics which decrease southwards towards the southwestern semi-arid region (Figure 1.1; Nicholson, 2000). The majority of southern Africa experiences a distinct wet season, receiving most of its rainfall during austral summer (December - February; DJF), whilst the dry season occurs during winter (June - August; JJA). However, some areas in the eastern equatorial region have bimodal seasonality, experiencing two rainfall seasons: a long rainfall season (March - June) and a shorter rainfall season (November - January) (Davis-Reddy & Vincent, 2017). In contrast, the southwestern region of South Africa is characterized by dry summers, receiving the majority of its rainfall during austral winter as a result of mid-latitude cyclones and cut-off lows (Reason, Landman & Tennant, 2006; Davis-Reddy & Vincent, 2017).

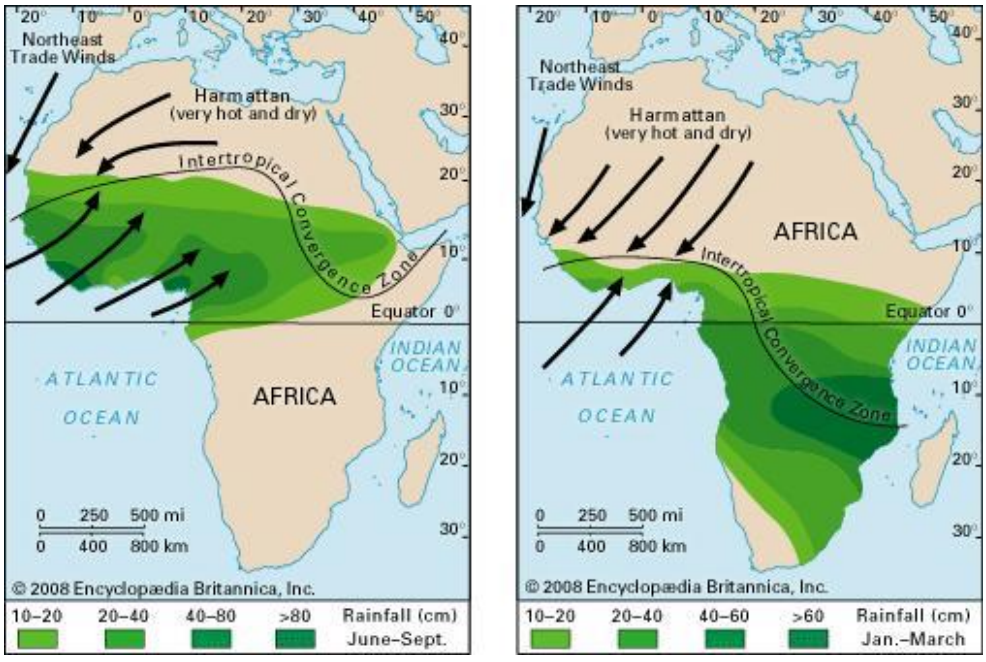

Figure 1.1 Position of the ITCZ and its associated precipitation in austral winter (left) and austral summer (right) (source: Encyclopedia Britannica)

Summer rainfall over southern Africa is primarily driven by the southward shift of the Intertropical Convergence Zone (ITCZ) and synoptic scale tropical-extratropical interactions, known as tropical temperate troughs (TTT). The ITCZ is where the north-easterly and south-easterly trade winds

converge, resulting in convective activity and substantial rainfall in the tropical region. This convergence zone is thermally driven following the region of maximum insolation, and as a result, shifts seasonally. In austral summer the ITCZ is at its southernmost position, located over Zambia, Mozambique and Madagascar, producing heavy rainfall in those regions (Nicholson, 2000; Reason, Landman & Tennant, 2006). On the other hand, TTT cloud bands form diagonally across the subcontinent, stretching from Angola to the southwest Indian Ocean, producing heavy rainfall across the region (Tyson & Preston-Whyte, 2000; Hart, Reason & Fauchereau, 2010; Nicholson, 2011; Macron *et al*., 2014). These systems link tropical perturbations with upper tropospheric troughs in the mid-latitudes, and are typically embedded within the South Indian Convergence Zone (SICZ; Cook, 2000; Ratna *et al*., 2013; Macron *et al*., 2014). The SICZ is the region where westerlies from the tropical Atlantic Ocean converge with easterlies from the tropical and subtropical Indian Ocean (Cook, 2000), making this region critical in supplying moisture to TTT. Nevertheless, there is high variability between TTT events in terms of their intensity, frequency and position, which is thought to be the difference between anomalously dry and wet years. Generally, TTT develop over southern Africa when there is easterly flow over the tropical region, however if westerly flow prevails, TTT develop in a more eastward position, over the Mozambique Channel and Indian Ocean (Nicholson, 2011).

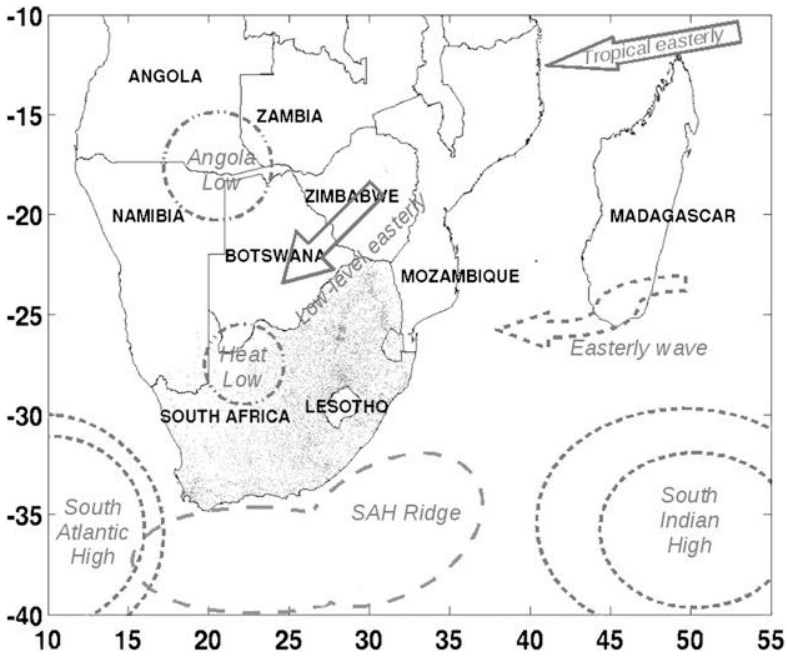

Figure 1.2 Southern Africa summer synoptic features (source: Hart, Reason & Fauchereau, 2010)

The synoptic pressure patterns also have an important role in the southern African climate (Figure 1.2). The southern region falls within the subtropical high-pressure belt, formed by the downward limb of the Hadley Cell. As a result, southern Africa is characterized by two quasi-stationary high-pressure cells, namely the South Atlantic High and the South Indian High, located over their respective ocean basins (Nicholson, 2011). During winter, these high-pressure cells shift northward, ridging across the subcontinent, causing dry, stable conditions. However, during summer, the high-pressure cells shift southward again while dry thermal lows and moist tropical low pressure systems develop over the subcontinent, forming the Angola Low, and supplying moisture to the subcontinent (Nicholson, 2011; Howard & Washington, 2018). However, southern Africa has high inter-seasonal and inter-annual rainfall variability as a result of numerous oceanic and atmospheric processes influencing the climate. The most prevalent mode of variability is the El Niño Southern Oscillation which often results in drought conditions throughout southern Africa.

1.3 Drought

1.3.1 What is Drought?

Drought is a naturally occurring feature of the climate system, which generally refers to a deficiency in precipitation for an extended period of time. Unlike aridity, which is a permanent feature of low rainfall regions, drought is a temporary aberration which can occur in any climatic zone (Wilhite & Glantz, 1985). However, it is difficult to have one universal definition as the socio-economic impacts and characteristics of drought vary from region to region and between social groups (Wilhite & Glantz, 1985; Hayes *et al*., 2012). While all definitions of drought stem from a deficiency in precipitation, they are also defined according to an individual or group's perspective (e.g. political, economic, scientific, agricultural, social) (Wilhite & Glantz, 1985; UNISDR, 2009; USGS, 2016). For instance, a meteorologist simply understands drought to be a lack of precipitation; a farmer might consider drought to be a period of insufficient soil moisture which impacts crop success; and a water resource manager may identify drought as a notable decrease in the water supply (USGS, 2016). In order to address these differences, drought has been categorized into four main types: meteorological, agricultural, hydrological, and socio-economic (Wilhite & Glantz, 1985; Hayes *et al*., 2012).

Meteorological drought is defined as an extended period of time during which precipitation is below a specified threshold (Wilhite & Glantz, 1985). This definition varies between regions as they have different atmospheric conditions and rainfall characteristics. For example, a reduction of 100 millimeters in precipitation would potentially put a semi-arid region at risk of drought, but would not have the same impact on a tropical region.

Agricultural drought occurs when there is a deficiency in the soil moisture available to support the growth of crops and forage, resulting in crop failures and affecting agricultural productivity. The available soil moisture is not directly proportional to the amount of precipitation as other factors can impact infiltration rates, such as evapotranspiration, soil type, slope and precipitation intensity (Wilhite & Glantz, 1985). This type of drought is also dependent on the water demand of the specific plant type and its stage of growth (Wilhite & Glantz, 1985;).

Hydrological drought ensues when there is a significant decrease in surface and subsurface waters, such as reservoirs, lakes, streams and aquifers (Wilhite & Glantz, 1985). These water supplies are critical to water resource management systems and, as such, this type of drought can adversely impact hydroelectric power production, tourism and industrial and domestic water supplies. Hydrological drought does not arise immediately following a precipitation deficit, but rather manifests after several months of dry conditions and is dependent on the water demands of the activities consuming those water resources (UNISDR, 2009).

Socio-economic drought occurs when the demand for an economic good or commodity, which is rain or water dependent (e.g. water, food and hydroelectric power), exceeds the supply, thereby impacting the region's economy and the livelihoods of its population. In this type of drought supply is periodically reduced as a result of a precipitation deficit. In contrast, increased demand can exacerbate this type of drought through urban and population growth as well as the development of the agricultural and energy sectors (Wilhite & Glantz, 1985).

The impact, timing and rate of recovery differs between these types of drought (Hayes *et al*., 2012). While meteorological drought focuses on the physical manifestation of drought, the agricultural, hydrological and socio-economic types emphasize the social impact, thereby highlighting the link

between precipitation and societal needs. The impacts of a precipitation deficit on surface and subsurface water supplies is not immediate and, as such, dry conditions usually need to persist for several weeks to impact soil moisture and for several months to impact water resources (e.g. streamflow, lakes and reservoirs) (UNISDR, 2009; Hayes *et al*., 2012). Figure 1.3 highlights the relationship between the different drought types and their impacts.

Beside the amount of precipitation, other climate variables are important in determining the frequency and severity of drought, such as temperature, wind, relative humidity and precipitation characteristics (e.g. duration, intensity, onset). In particular, they help to establish a positive feedback mechanism which reinforces the drought conditions (Mishra & Singh, 2010). For example, a deficit in precipitation leads to a reduction in soil moisture which, in turn, lessens evapotranspiration rates and subsequently decreases relative humidity, resulting in a reduced probability of future precipitation. In this situation, it would require moisture from an external source to be transported over the region to alleviate the drought (Mishra & Singh, 2010).

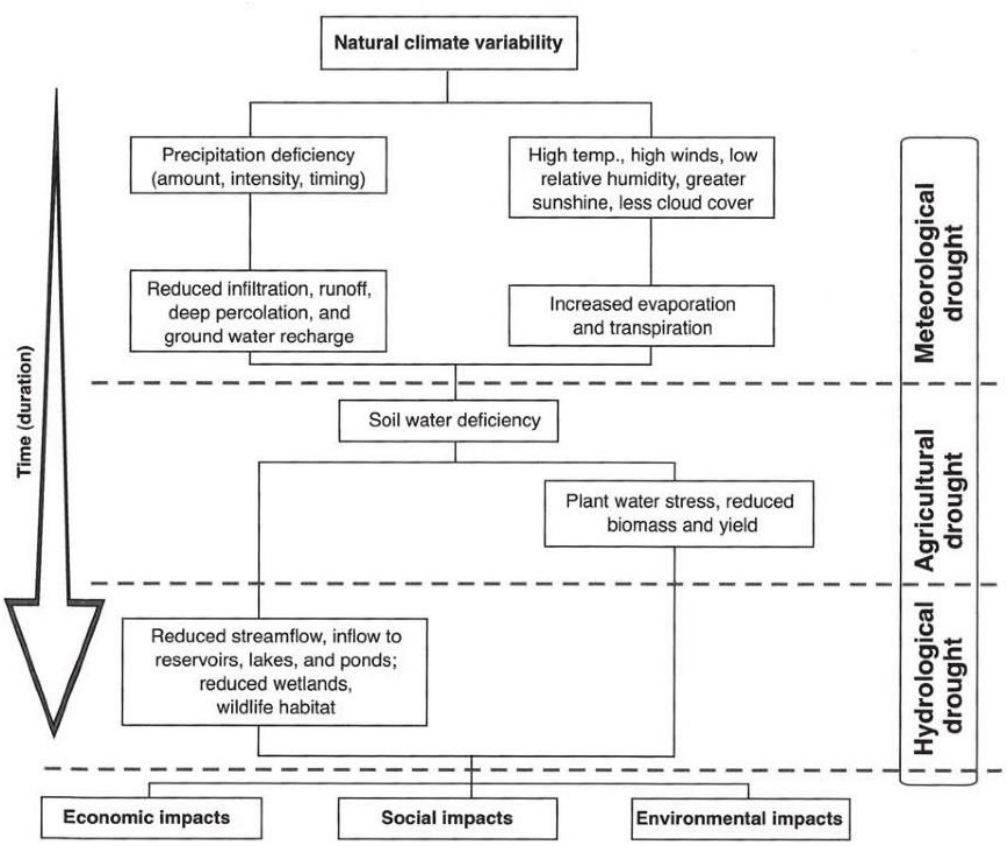

Figure 1.3 Types of drought and their associated characteristics (source: Wilhite, 2000)

1.3.2 Impacts of Drought

Drought is a recurrent, complex and widespread phenomenon impacting millions of people, making it one of the most devastating, prevalent and costly natural hazards (Wilhite, 2000; Hayes *et al*., 2012; Masih *et al*., 2014). It has many socio-economic and agricultural repercussions, ranging from the individual to regional scale (Figure 1.4). Drought particularly impacts the agricultural sector, resulting in crop failures and livestock deaths, which can lead to extensive food shortages, malnutrition and, in severe cases, famine (Vogel & Drummond, 1993; Wilhite, 2000; Calow *et al*., 2010; Hayes *et al*., 2012; Masih *et al*., 2014). There is also a significant economic loss associated with food shortages as food prices escalate and gross domestic product (GDP) is affected by decreased productivity and increased food imports (FAO, 2004; Calow *et al*., 2010). The agricultural sector in southern Africa is particularly vulnerable to drought due to its semi-arid climate and dependence on rain-fed agriculture (FAO, 2004; Davis-Reddy & Vincent, 2017). In 2015/16, the majority of southern Africa experienced a 25% reduction in summer rainfall as well as abnormally high temperatures (Figure 1.5), which led to one of the worst droughts on record, affecting 39 million people (FEWS NET, 2016; SADC, 2016). This had serious repercussions for the community, as 70% of the population rely on agriculture for food and employment (SADC, 2018). A large proportion of maize crops failed during the 2015/16 season, which resulted in a regional cereal deficit of 7.4 million tonnes (11% decrease) (FEWS NET, 2016; SADC, 2016; Davis-Reddy & Vincent, 2017). Consequently, grain prices were significantly inflated, especially in Malawi and Mozambique where prices were increased by more than 75% (FEWS NET, 2016). There was another extensive drought in 1991/92 during which there was a 70% decrease in crop output across southern Africa (Vogel & Drummond, 1993; Davis-Reddy & Vincent, 2017). This resulted in an estimated US$ 500 million loss of GDP in South Africa as well as 50 000 jobs lost in the agricultural sector (FAO, 2004).

Figure 1.4 Image showing the extensive dry conditions and crop failures associated with drought in southern Africa (source: ClimateSignals.org)

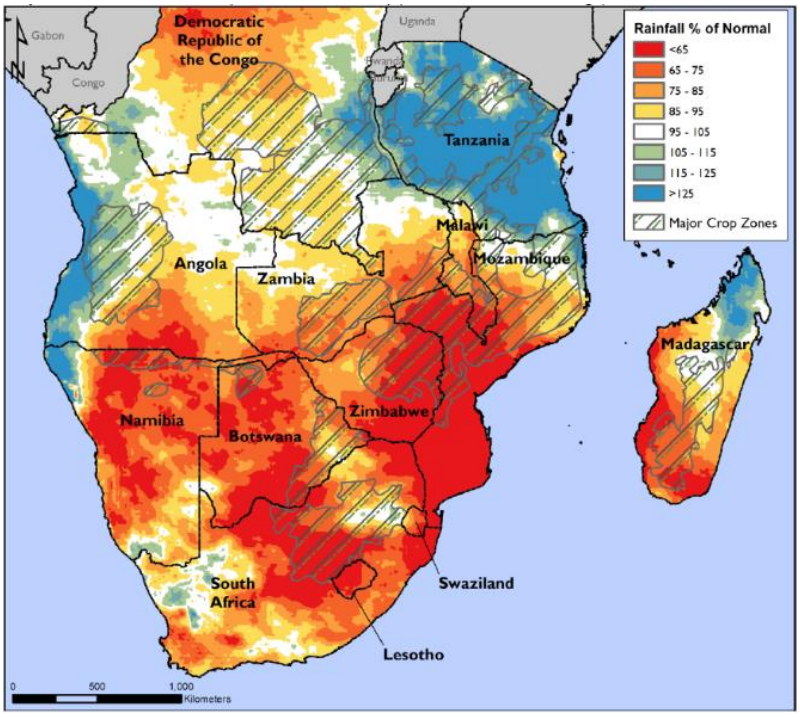

Figure 1.5 Map showing the percentage of normal rainfall during the summer season of 2015/16 (source: FEWS NET, 2016)

Water scarcity is another consequence of drought with many detrimental impacts (Figure 1.6). Insufficient surface and subsurface water supplies can lead to low dam and reservoir levels, creating a shortage of water for human and animal consumption, as well as other industries. This often results in communities using unsafe water sources, which can promote the spread of waterborne diseases. This was seen during the 1991/92 drought, where it was estimated that 3 million people in Malawi had little or no access to clean water, resulting in outbreaks of cholera, typhoid and dysentery. Similar impacts were also seen in parts of South Africa, Lesotho and Zimbabwe during this time (Calow *et al*., 2010; SADC, 2016). In addition, reduced water levels can significantly affect the generation of hydroelectric power, as was the case in Zambia where hydroelectric power production was reduced by 35% during the 1991/92 drought (Davis-Reddy & Vincent, 2017). Diminished hydroelectric power can lead to power outages which disrupt households and industries, as well as public services, such as hospitals and schools (SADC, 2016). Drought can also cause significant damage to the environment through land degradation which can put a region at risk of desertification and aridity (Masih *et al*., 2014). There is also increased risk of fire in instances where drought is accompanied by extreme temperatures (Davis-Reddy & Vincent, 2017). The culmination of these impacts can be devastating for a community and, in severe cases, may also result in conflict over resources, mass migration and loss of life (Calow *et al*., 2010; Masih *et al*., 2014).

Figure 1.6 Before and after photos of the Theewaterskloof Dam following the 2016 drought.

1.4 El Niño Southern Oscillation

El Niño Southern Oscillation (ENSO) is a major driver of southern Africa drought because of its influence on inter-annual rainfall variability over the subcontinent (Goddard & Graham. 1999; Reason *et al*., 2000; Tyson & Preston-Whyte, 2000; Johnson, 2013; Anyamba *et al*., 2014; Yuan *et al*., 2014). It is an ocean-atmosphere phenomenon that consists of large-scale warming (El Niño) or cooling (La Niña) of the equatorial eastern Pacific sea surface temperatures (SST). It was first identified in the 19th century by Peruvian sailors as an anomalous southward flowing warm current along the coast which occurred periodically around Christmas, hence the name 'El Niño' referring to the Christ Child (Trenberth, 1997). Subsequently, it was discovered that these warm SST anomalies extend right across the tropical eastern Pacific Ocean, fluctuating on a 2 - 7 year cycle with anomalously cold SST phases, known as La Niña (meaning 'girl child'). These SST anomalies across the Pacific Ocean affect the lower tropospheric pressure fields, resulting in fluctuations which are characteristic of the Southern Oscillation (Trenberth, 1997; Hoell *et al*., 2015). Hence, this coupled ocean-atmosphere phenomenon is known as the El Niño Southern Oscillation. The Walker Circulation is a series of zonal cells stretching across the southern hemisphere (Figure 1.7), primarily driven by the zonal overturning circulation over the equatorial Pacific Ocean, creating atmospheric links between distant regions (Tyson & Preston-Whyte, 2000). These links are known as teleconnections and enable ENSO to influence temperature and rainfall variability globally (Larkin & Harrison, 2005; Chretien *et al*., 2015; Hoell *et al*., 2015). The global impacts associated with ENSO teleconnections can be seen in Figure 1.8.

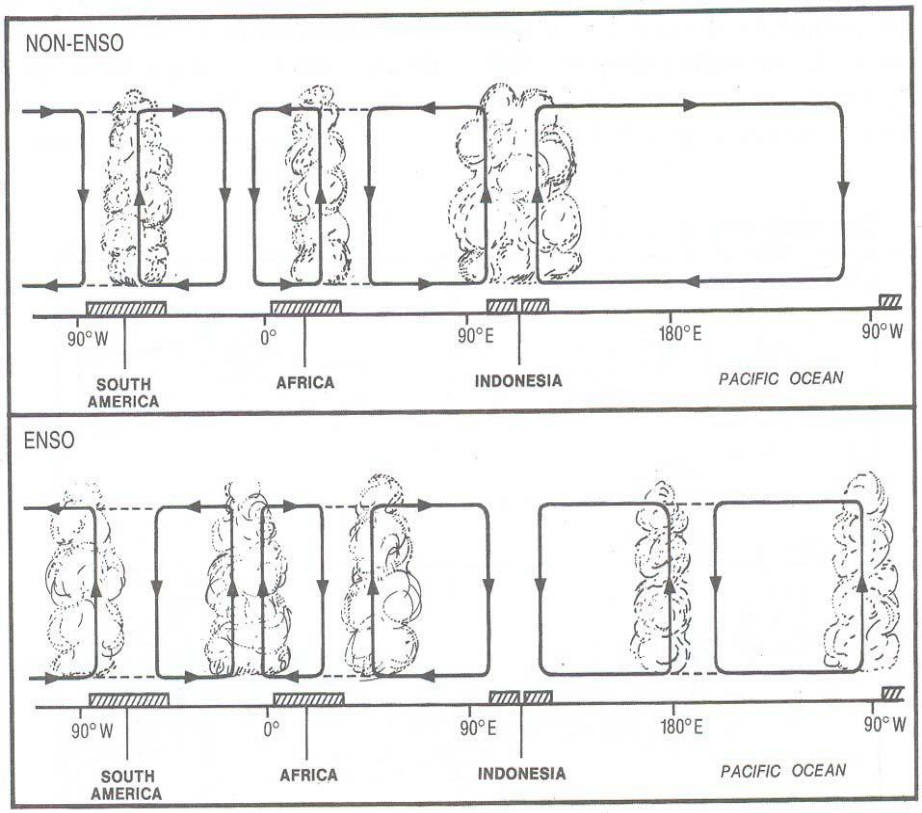

Figure 1.7 The Walker circulation during non-ENSO (normal or La Niña) and ENSO years (source: Tyson & Preston, Whyte, 2000)

Typically, an El Niño event will reduce precipitation over Southern Africa, resulting in drought conditions, while a La Niña event will intensify precipitation (Tyson & Preston-Whyte, 2000; Larkin & Harrison, 2005; Ashok et al., 2007; Davis, 2011; Johnson, 2013; Hoell et al., 2015; Yuan et al., 2014). An El Niño event is characterized by anomalous warm water in the eastern equatorial Pacific Ocean, resulting in a lower pressure over the eastern Pacific Ocean compared to that over Indonesia. This weakens the Walker circulation, resulting in surface convergence over the eastern Pacific and surface divergence over Indonesia. Southern Africa experiences a high pressure as the descending limb of the Walker circulation falls over the continent producing dry, stable conditions (Tyson & Preston-Whyte, 2000). On the other hand, La Niña is characterized by cool SST anomalies across the eastern equatorial Pacific Ocean, resulting in increased pressure over the eastern Pacific Ocean compared to that over Indonesia. This enhances the Walker circulation, resulting in divergence over the eastern Pacific and convergence over Indonesia. Southern Africa

experiences a low pressure as the ascending limb of the Walker circulation falls over the continent, promoting convective activity (Tyson & Preston-Whyte, 2000). However, the above descriptions are a generalised and basic understanding of ENSO and the relationship with southern Africa rainfall is not linear. There is high variability of ENSO SST anomalies, resulting in varying climatic outcomes. Therefore, it is important to consider different patterns of ENSO in order to fully understand and predict the influence on regional climate conditions.

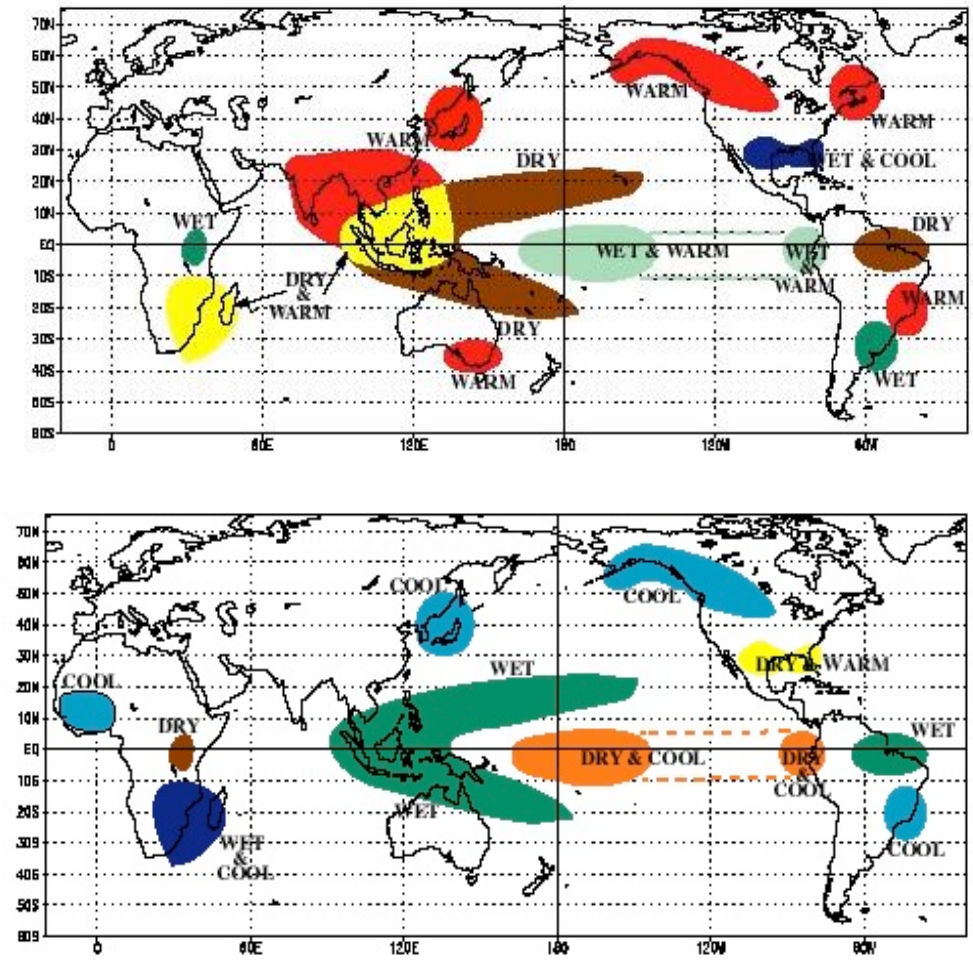

Figure 1.8 Teleconnections associated with El Niño (top) and La Niña (bottom) (source: NOAA)

1.5 Aims & Objectives

Although research has made great progress in determining circulation and precipitation over Southern Africa during El Niño and La Niña phases, there is a lack of understanding as to the influence of different ENSO patterns on drought over Southern Africa. The aim of this study is to investigate the link between drought and different patterns of ENSO. To achieve this aim, the following objectives are addressed:

- Examine the capability of a global climate model (called SPEEDY) in simulating the southern African climate and the influence of ENSO on southern African droughts
- Study the sensitivity of SPEEDY's performance to the inclusion of dynamic vegetation parameters
- Investigate the relative performance of SPEEDY to those of more complex global climate models
- Examine the sensitivity of southern African droughts to various ENSO patterns in SPEEDY's ensemble simulations.
- Understand the atmospheric dynamics or circulations that link each ENSO pattern with drought over southern Africa

This dissertation consists of six chapters. Chapter 1 introduces the southern African region and key concepts used in this study. Chapter 2 presents a literature review of the methods used to quantify drought, discussion on the influence of different modes of rainfall variability over southern Africa as well as a review of climate modelling teleconnections to southern Africa rainfall. Chapter 3 describes the data and model used in the study as well as the experiment design. Chapter 4 presents the model evaluation of SPEEDY, comparing vegetation schemes and performance against more complex GCMs. Chapter 5 presents the results and discussion of the multi-forcing ensemble simulations of the ENSO patterns. A summary and concluding remarks are given in Chapter 6.

Chapter 2: Literature Review

This chapter provides a comprehensive review of the literature relating to droughts in southern Africa. Section 2.1 gives an overview of the main drought indices which have been used in studies to characterize drought in southern Africa. Section 2.2 focuses on different modes of variability and their influence on southern Africa rainfall. Section 2.3 briefly summarizes the different approaches to simulating ENSO teleconnections and southern Africa climate.

2.1 Quantifying Drought

Due to the complexity of drought, previous studies have introduced indices as a method of quantifying drought characteristics (such as duration, spatial extent, magnitude and intensity), which are important for monitoring and management (Mishra & Singh, 2010; Vicente-Serrano *et al*., 2010; Hayes *et al*., 2012). However, the subjective nature of drought has resulted in the development of multiple indices. For instance, meteorological drought can be monitored using the Palmer Drought Severity Index (PDSI; Palmer, 1965), Standardized Precipitation Index (SPI; McKee *et al*., 1993) and Standardized Precipitation Evapotranspiration Index (SPEI; Vicente-Serrano *et al*., 2010). Agricultural drought can be monitored using the Crop Moisture Index (CMI; Palmer, 1968), Root Stress Anomaly Index (RSAI; Trambauer *et al*., 2014) and Evapotranspiration Deficit Index (ETDI; Narasimhan & Srinivasan, 2005). Lastly, hydrological drought can be monitored using the Standardized Runoff Index (SRI; Shukla & Wood, 2008), Groundwater Resource Index (GRI; Mendicino *et al*., 2008) and Surface Water Supply Index (SWSI; Shafer & Dezman, 1982; Garen, 1993). While some indices are based solely on precipitation (e.g. SPI, deciles and percentage of normal), other indices include a combination of other climatic (e.g. SPI, CMI, ETDI and PDSI) and hydrometeorological variables (e.g. GRI, SRI and SWSI) (Mishra & Singh, 2010; Hayes *et al*., 2012). These drought indices are summarized in Table 2.1. While many drought indices have been mentioned in the literature, the most widely used indices are PDSI, SPI and SPEI, which are discussed in further detail below.

Table 2.1 Summary of drought indices (adapted from Ntale & Gan, 2003 and Trambauer et al., 2014). Variables: P: precipitation; T: temperature; ET: evapotranspiration; PET: potential evapotranspiration; L: soil moisture; RO: runoff; sn: snowpack

Index	Variables	Brief Description	Reference
Meteorological Drought Indices			
Deciles	*P*	The decile method groups monthly precipitation occurrences into deciles.	Gibbs & Maher, 1967
Percentage of normal (PN)	*P*	PN is calculated by dividing P with the mean value.	
Palmer Drought Severity Index (PDSI)	*P*, *T*, *L*, ET	PDSI is a soil moisture algorithm, based on moisture inflow, outflow and storage. It is calibrated for relatively homogeneous regions.	Palmer, 1965
Standardized Precipitation Index (SPI)	*P*	An index based on the probability of precipitation at specific time scales.	McKee *et al*., 1993
Standardized Precipitation Evapotranspiration Index (SPEI)	*P*, PET	An extension of SPI, based on the probability of the climate moisture balance (P - PET).	Vicente-Serrano *et al*., 2010
Agricultural Drought Indices			
Crop Moisture Index (CMI)	*P*, *T*, ET, *L*, RO	Derived from PDSI, CMI is a measure of the moisture supply in the short term. Primarily used in major crop-producing regions.	Palmer, 1968
Evapotranspiration Deficit Index (ETDI)	PET, ET	ETDI computes the water stress anomaly in terms of water availability for evaporation.	Narasimhan & Srinivasan, 2005
Root Stress Anomaly Index (RSAI)	*L*	RSAI computes the anomaly of soil moisture available at the root zone, which impacts root growth and yield.	Trambauer *et al*., 2014

Hydrological Drought Indices			
Surface Water Supply Index (SWSI)	*P*, sn, RO, reservoir storage	Similar to SPI, SWSI is based on a probability distribution which also includes snow pack, runoff and reservoir storage.	Shafer & Dezman, 1982; Garen, 1993
Standardized Runoff Index (SRI)	RO	SRI is based on the probability of hydrologic runoff accumulated over a specific time.	Shukla & Wood, 2008
Groundwater Resource Index (GRI)	Groundwater	GRI is based on a simple water balance model which standardizes monthly groundwater storage.	Mendicino *et al*., 2008

2.1.1 Palmer Drought Severity Index (PDSI)

PDSI, developed by Palmer (1965), has been one of the most widely used drought indices in the literature, particularly in the United States of America (USA; Ntale & Gan, 2003). This drought index is based on the soil water balance equation, estimating the supply and demand of moisture from precipitation, soil moisture, temperature and evapotranspiration (Mishra & Singh, 2010; Vicente-Serrano *et al*., 2010). This makes it a useful tool, particularly in climate change studies, as it accounts for sensitivities to both precipitation and temperature (Mishra & Singh, 2010). However, there are some shortcomings to PDSI, which include the assumption that rainfall is the only form of precipitation, and its limited application as it is calibrated for a particular region. These shortcomings have led to the development of modified versions, such as the Palmer Hydrological Drought Index (PHDI; Karl, 1986), the Crop Moisture Index (CMI; Palmer, 1968) and the self-calibrated PDSI (SC-PDSI; Wells, Goddard & Hayes, 2004). Despite these improvements, the main limitation remains the fixed temporal scale (9 - 12 months) which does not allow for the distinction between drought types (Mishra & Singh, 2010; Vicente-Serrano *et al*., 2010; Trambauer *et al*., 2014). PDSI has been used in numerous drought studies globally, including the investigation of temporal and spatial characteristics of drought in the USA (e.g. Karl & Koscielny, 1982) and variability of drought in China (e.g. Zou, Zhai & Zhang, 2005). Although southern Africa has been included in global drought studies using SC-PDSI (e.g. Zhao & Dai, 2015), there are not many studies which use PDSI specifically in southern Africa. Nevertheless, it

has been implemented in studies over East Africa, such as Ntale & Gan (2003) who used a modified PDSI in their evaluation of drought indices over the region. Their findings showed that SPI was a more suitable drought index for East Africa.

2.1.2 Standardized Precipitation Index (SPI)

Many studies have made use of SPI, an alternative drought index to PDSI, which was developed by McKee *et al*. (1993). It is obtained by fitting a probability distribution function (usually gamma distribution) to the long-term precipitation record, transforming to a normal distribution and then measuring the standardized deviation of a period from the long term mean (Ntale & Gan, 2003; Mishra & Singh, 2010; Trambauer *et al*., 2014). Therefore, SPI measures both extremely dry and extremely wet conditions on a scale from -2 (and less) to 2 (and above), respectively (see Table 2.2). SPI is a popular method to calculate drought as it can be easily adapted to any climatic region, and is relatively simple to compute as it only requires precipitation data. The fundamental advantage of SPI, however, is its ability to calculate drought at various time scales, making it relevant to all drought types (Ntale & Gan, 2003; Mishra & Singh, 2010; Vicente-Serrano *et al*., 2010; Hayes *et al*., 2012; Trambauer *et al*., 2014). For instance, SPI at 3- and 6-month time scales captures changes in soil moisture and water supplies, making it suitable to monitor meteorological and agricultural drought. In addition, it can also capture changes in long-term water supplies at 6-, 12-, 24- and 48-month time scales, making it ideal for hydrological drought as well. In southern Africa, SPI has been used in a multitude of studies. Rouault & Richard (2005) and Richard *et al*. (2001) used SPI to investigate the spatial extent of drought in southern Africa throughout the 20th century, while Malherbe *et al*. (2015) studied the decadal variability of South African droughts. In Zimbabwe, the spatiotemporal characteristics of drought (Manatsa *et al*., 2010) as well as drought predictors (Manatsa *et al*., 2008) have been investigated using SPI. In addition, SPI has been used in seasonal forecasts of drought in African river basins (Dutra *et al*., 2013). Nevertheless, SPI is limited by using only precipitation in its calculation. While precipitation is the main factor defining drought, other climate variables are also important in determining the frequency and severity of drought, such as temperature, wind, relative humidity and precipitation characteristics (e.g. duration, intensity, onset) (Mishra & Singh, 2010; Vicente-Serrano *et al*., 2010; Trambauer *et al*., 2014). A modification of SPI, known as SPEI, has been developed to address this shortcoming.

Table 2.2 SPI Classification (source: Fuchs et al., 2014)

SPI	Drought category
2.0 and above	Extremely wet
1.5 to 1.99	Very wet
1 to 1.49	Moderately wet
-0.99 to 0.99	Near normal
-1 to -1.49	Moderately dry
-1.5 to -1.99	Severely dry
-2 and less	Extremely dry

2.1.3 Standardized Precipitation Evapotranspiration Index (SPEI)

SPEI is a more recent drought index developed by Vicente-Serrano *et al*., (2010). Similar to SPI, SPEI is obtained by fitting a probability distribution (usually log-logistic distribution) to the climate moisture balance (CMB), from which the standardized deviation of a period is measured against the long term mean (Trambauer *et al*., 2014). It has a similar classification to SPI, ranging from ≤ -2 for extreme drought to ≥ 2 for extreme wet conditions (see Table 2.3). CMB is the difference between precipitation and potential evapotranspiration (PET), taking into account the influence of both precipitation and temperature. Therefore, SPEI combines the strengths of PDSI and SPI, showing sensitivity to evaporative demand as well as computational efficiency and multi-temporal capabilities, making it a popular tool for drought studies. Ujeneza & Abiodun (2014) used SPEI to analyze the spatio-temporal variability of drought in southern Africa, while Abiodun *et al*. (2018) investigated future projections of drought over southern Africa river basins. Abiodun *et al*. (2018) found that the use of SPEI is particularly important in climate change projections as the use of only precipitation (SPI) could underestimate the magnitude and robustness of the drought signal. Trambauer *et al*. (2014) used multiple drought indices to investigate the spatio-temporal variability of drought over the Limpopo river basin. They found that 3-month SPEI was a good alternative to monitor agricultural drought in the absence of adequate information to calculate more complex indices, such as ETDI and RSAI. Meque & Abiodun (2015) demonstrated that ENSO has a stronger correlation with temperature and SPEI than with precipitation in parts of southern Africa, highlighting the importance of using SPEI in ENSO related drought studies.

For this study, both SPI and SPEI will be used at the 3-month time scale to characterize drought over southern Africa.

Table 2.3 SPEI classification (source: Wang et al., 2014)

SPEI	Drought category	Probability (%)
≥ 2	Extreme wet	2.3
1.5 to 1.99	Severe wet	4.4
1 to 1.49	Moderate wet	9.2
0 to 0.99	Mild wet (near-normal)	34.1
0 to -0.99	Mild drought (near-normal)	34.1
-1 to -1.49	Moderate drought	9.2
-1.5 to -1.99	Severe drought	4.4
≤ -2	Extreme drought	2.3

2.2 Modes of Variability Influencing Southern Africa Rainfall

Many studies have identified that southern Africa is particularly susceptible to droughts because of its high inter-seasonal and inter-annual rainfall variability (Mason & Joubert, 1997; Goddard & Graham, 1999; Yuan *et al*., 2014). Various atmospheric and oceanic features have been shown to modulate rainfall over southern Africa, including El Niño Southern Oscillation (ENSO; Cook, 2001; Meque & Abiodun, 2015), Indian Ocean Dipole (IOD; Saji *et al*., 1999), Subtropical Indian Ocean Dipole (SIOD; Behera & Yamagata, 2001), Benguela Niño (Shannon *et al*., 1986; Rouault *et al*., 2003), Madden Julian Oscillation (MJO; Pohl, Richard & Fauchereau, 2007; Pohl *et al*., 2010) and Southern Annular Mode (SAM; Reason & Rouault, 2005; Gillett, Kell & Jones, 2006). While some studies have identified ENSO as the leading mode of rainfall variability in southern Africa (Reason *et al*., 2000; Tyson & Preston-Whyte, 2000; Johnson, 2013; Yuan *et al*., 2014), others have highlighted the role of other climate features (Goddard & Graham, 1999; Reason, 2001; Behera & Yamagata, 2001; Rouault *et al*., 2003). This section will discuss the various oceanic and atmospheric features and processes that modulate the spatio-temporal distribution of rainfall over southern Africa.

2.2.1 Indian Ocean Dipoles

Studies (e.g. Behera & Yamagata, 2001; Reason 2001; Reason 2002) have identified the Indian Ocean Dipole (IOD) and subtropical Indian Ocean Dipole (SIOD) as two prominent modes of variability in the Indian Ocean, consisting of anomalous fluctuations in SST which present in a dipole pattern. The IOD was first identified by Saji *et al*. (1999) as a feature of the tropical Indian Ocean which altered the Walker Circulation. The positive (negative) phase is characterized by warm (cool) SST anomalies off the coast of East Africa and cool (warm) SST anomalies in the eastern Indian Ocean. Saji *et al*. (1999) and Saji & Yamagata (2003) found that the positive (negative) IOD is associated with increased (decreased) precipitation over East Africa. Saji & Yamagata (2003) also found that positive IOD is linked to decreased precipitation over South Africa. In contrast, SIOD is a subtropical feature during austral summer, with the positive (negative) phase characterized by warm (cool) SST anomalies in the southwest Indian Ocean, south of Madagascar, and cool (warm) SST anomalies in the southeast Indian Ocean. Behera & Yamagata (2001) found that the positive SIOD caused a strengthening of the South Indian High pressure, resulting in enhanced precipitation over southeastern Africa. This was confirmed by Reason (2001; 2002) and Reason & Jagadheesha (2005) who attributed the enhanced precipitation to increased moisture flux convergence over the subcontinent as well as favourable conditions for TTT formation. On the other hand, the negative SIOD is associated with decreased precipitation over southern Africa as a result of reduced moisture flux and low-level divergence over the region (Reason, 2002).

2.2.2 Benguela Niño

Benguela Niño is an intermittent phenomenon which is characterized by strong SST anomalies (2 - 4˚C) off the western coast of southern Africa, usually during late austral summer (Shannon *et al*., 1986). This occurs when the trade winds over the western Atlantic Ocean weaken resulting in an eastward propagating equatorial Kelvin wave. This disrupts the Benguela upwelling, resulting in the advection of warm water from the Angola current southwards (Florenchie et al., 2003; Rouault *et al*., 2003; Rouault *et al*., 2018). Studies have identified the link between Benguela Niño and increased precipitation over the southwestern region of Africa, due to increased moisture flux from the Indian and Atlantic Oceans (Hirst & Hastenrath, 1983; Rouault *et al*., 2003). However,

Hansingo & Reason (2009) and Reason & Smart (2015) highlight that this relationship is nonlinear and is sensitive to SST anomalies in the south western Indian Ocean.

2.2.3 Madden Julian Oscillation (MJO)

The Madden–Julian oscillation (MJO) is one of the leading modes of intra-seasonal variability in the tropical atmosphere. It develops as a result of large-scale coupling between tropical deep convection and atmospheric circulation. MJO is an eastward propagating (4 - 8 m/s) system of large scale convective clusters which propagate across the tropical Indian and Pacific Oceans on a 30- to 90-day cycle (Madden & Julian, 1971). In southern Africa, MJO produces convective clusters which propagate across the region, resulting in significant dry and humid phases with a strong 30- to 60-day periodicity (Pohl, Richard & Fauchereau, 2007; Pohl *et al*., 2010). The dry (humid) phases are associated with southerly (northerly) moisture flux anomalies which inhibit (favor) atmospheric convection over the subcontinent and weaken (strengthen) mid-tropospheric easterly flow over the Congo basin. Hart, Reason & Fauchereau (2013) investigated the influence of MJO on TTT intensity over southern Africa, while Liebman, Hendon & Glick (1994) and Bessafi & Wheeler (2006) analyzed the influence on tropical cyclone development over the west Indian Ocean.

2.2.4 Southern Annular Mode (SAM)

Studies have shown the Southern Annular Mode (SAM; otherwise known as Antarctic Oscillation, AAO) to be the primary mode of atmospheric variability between the high- and mid-latitudes in the Southern Hemisphere (Thompson & Wallace, 2000; Reason & Rouault, 2005; Gillett, Kell & Jones, 2006; Pohl *et al*., 2010). It is essentially a fluctuation in pressure between the Antarctic and the mid-latitudes. The positive phase is characterized by low (high) pressure anomalies over Antarctica (southern mid-latitudes), with a southward shift in the westerly winds and subtropical jet. Reversed conditions are seen during the negative phase (Thompson & Wallace, 2000; Reason & Rouault, 2005; Gillett, Kell & Jones, 2006; Pohl *et al*., 2010). Gillett, Kell & Jones (2006) found the SAM to influence summer precipitation in southeastern Africa, resulting from increased moisture advection from the Indian Ocean due to easterly anomalies. Pohl *et al*. (2010) found this relationship to be strongest during La Niña phases. In addition, it was found by Reason & Rouault

(2005) that there is a southward shift in the mid-latitude cyclone track during positive SAM, thereby reducing winter precipitation in the southwestern region.

2.2.5 El Niño Southern Oscillation (ENSO)

Many researchers consider ENSO to be the dominant mode of interannual climate variability. It consists of large-scale warming (El Niño) or cooling (La Niña) of the equatorial Pacific Ocean, affecting the Walker Circulation and moisture transport globally. In southern Africa, studies consider ENSO to be the teleconnection with the greatest impact on summer rainfall, often resulting in drought (Nicholson & Entekhabi, 1987; Lindesay, 1988; Nicholson & Kim, 1997; Reason et al., 2000; Cook, 2001; Reason and Jagadheesa, 2005). For instance, Rouault & Richard (2005) investigated the spatio-temporal characteristics of drought throughout the 20th century in southern Africa, and found that over 66% of severe droughts could be attributed to ENSO. Furthermore, it was noted that the influence of ENSO on southern Africa climate has strengthened since the 1970s. Studies (e.g. Tyson & Preston-Whyte, 2000; Ashok et al., 2007; Davis, 2011; Hoell et al., 2015; Yuan et al., 2014; Meque & Abiodun, 2015) agree that El Niño (La Niña) typically reduces (intensifies) precipitation over the southeastern region of Africa, resulting in dry (wet) conditions, while increasing (decreasing) precipitation over the northeastern tropical region. These precipitation anomalies can be attributed to changes in various synoptic-scale atmospheric features, such as the Angola low (Reason & Jagadheesha, 2005), Walker Circulation (Lindesay, 1988) and tropical cyclones (Ash & Matyas, 2012). Most notably, Cook (2000; 2001) and Meque & Abiodun (2015) found that the weakening of the south Indian high pressure during El Niño resulted in a northeastward shift of the SICZ and fewer TTT developing over the subcontinent. In contrast, Manhique *et al*. (2011) found that during La Niña the SICZ was located predominantly over the subcontinent, resulting in significant TTT formation and precipitation increases. Tyson & Preston-Whyte (2000) describe the common circulation patterns associated with El Niño and La Niña events over southern Africa, as shown in Figure 2.1.

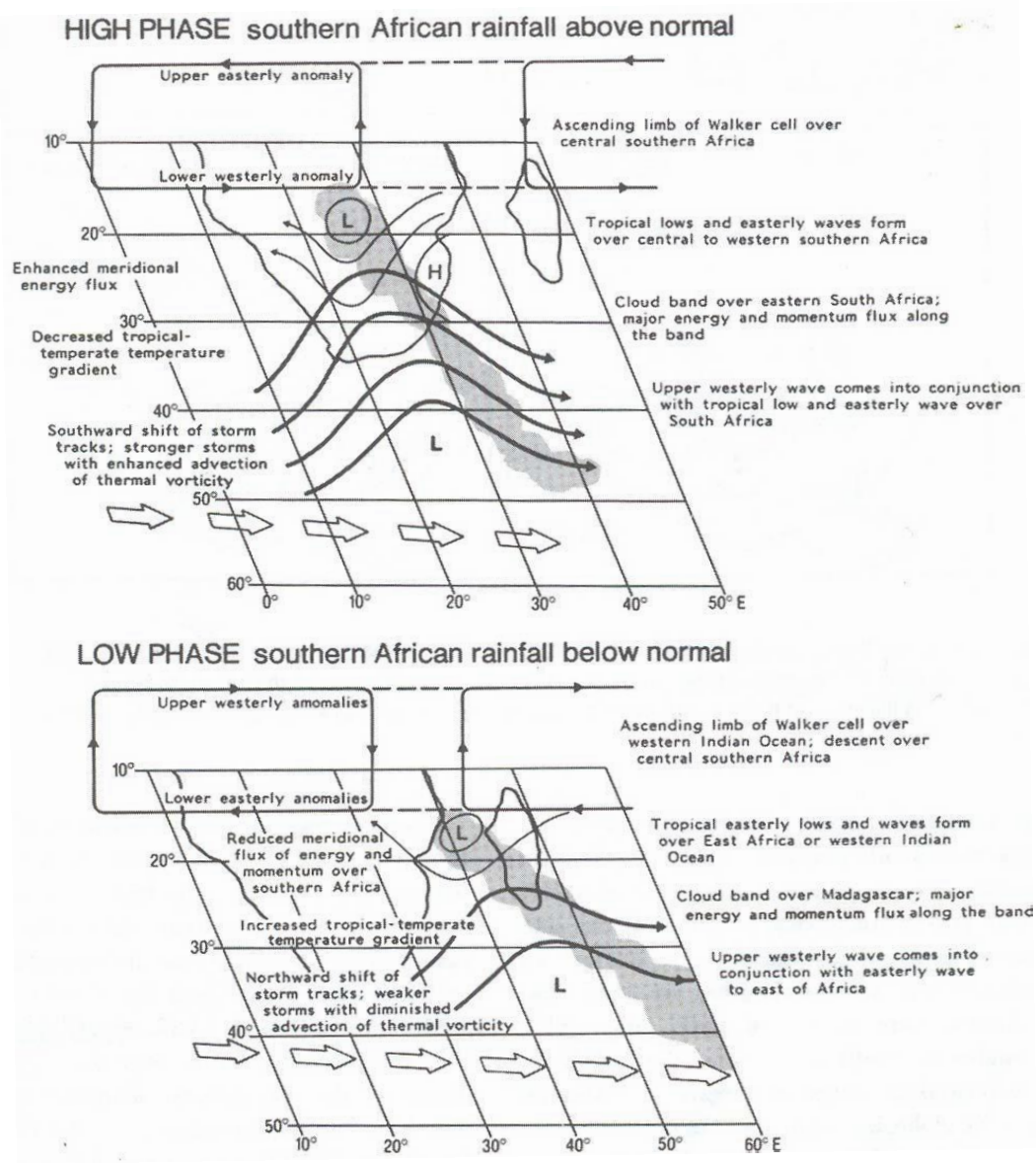

Figure 2.1 Schematic representation of anomalous circulation associated with La Niña phases (top) and El Niño phases (bottom) (source: Tyson & Preston-Whyte, 2000)

Nevertheless, many studies identify that the relationship between ENSO and southern Africa rainfall is nonlinear (Tyson & Preston-Whyte, 2000; Reason & Jagadheesha, 2005; Fauchereau *et al*., 2009; Yuan et al., 2014). There is high variability in the spatial extent, timing and intensity of the impacts. For example, the strong El Niño of 1997 was expected to produce severe drought conditions across southern Africa, but ultimately had little to no impact (Tyson & Preston-Whyte,

2000). This nonlinear relationship can be explained by the complex interactions between the different modes of variability. For instance, Reason & Jagadheesha (2005) attribute the lack of response to the 1997 strong El Niño, to a positive IOD and warm SST off the west coast of southern Africa. Tyson & Preston-Whyte (2000) also explain that the influence of ENSO is highly dependent upon the phase of the stratospheric quasi-biennial oscillation. However, the nonlinear relationship can also be explained by internal variability of ENSO. Kao & Yu (2009) state that ENSO patterns or 'flavours' can be distinguished by variations in their periods, onset time, or Pacific SST anomalies. The two most popular ENSO patterns are Eastern Pacific (EP, also called 'canonical ENSO') and Central Pacific ENSO (CP; also known as 'dateline ENSO', 'warm pool ENSO' or 'ENSO Modoki') (Larkin & Harrison, 2005; Ashok et al., 2007; Kao & Yu, 2009; Johnson, 2013; Yeh et al., 2015). Ratnam *et al*. (2012; 2014) investigated the teleconnections associated with each pattern and found EP ENSO to produce more severe droughts over southern Africa due to stronger modification of the Walker Circulation.

Johnson (2013) found that these two ENSO classifications remained limited and subjective, which led him to identify eight ENSO SST patterns over the Pacific Ocean (Figure 2.2; four El Niño SST conditions EN1 - EN4; and four La Niña SST conditions LN1 - LN4). Johnson (2013) used self-organizing maps (SOMs) (a neural network-based cluster analysis) to determine eight statistically distinct ENSO SST patterns for the tropical Pacific Ocean. This method is superior because it portrays ENSO as a continuum of patterns, making it easier to interpret (Johnson, 2013). However, some studies have highlighted the role of the other ocean basins and modes of variability in southern Africa climate (e.g. Goddard & Graham, 1999; Behera & Yamagata, 2001; Reason, 2001; Rouault et al., 2003). Therefore, to further the work, Hoell et al. (2015) examined the influence of each ENSO pattern on tropical SST, global atmospheric circulation, and southern Africa precipitation during the period 1950-2010. The study clearly showed that the four El Niño SST conditions produce different rainfall patterns over southern Africa; and the same is true for the four La Niña SST conditions. While Hoell *et al.* (2015) focus their study on precipitation anomalies, the main factor when considering drought, studies have shown that other climate variables (e.g. temperature, wind, relative humidity, precipitation duration, intensity and onset) can also influence the frequency and severity of drought (Mishra & Singh, 2010; Vicente-Serrano *et al.*, 2010; Trambauer *et al.*, 2014). For instance, Meque & Abiodun (2015) showed that the

influence of evapotranspiration on southern Africa drought is significant, particularly when investigating ENSO impacts. Therefore, the results of Hoell et al. (2015) might have underestimated the influence of ENSO patterns on droughts over southern Africa, as they only considered precipitation. Additionally, the number of observations for each ENSO pattern is small, which makes it difficult to discern a robust influence of ENSO on southern Africa drought. Therefore, this study aims to build on the observational evidence presented by Hoell *et al.* (2015) by using an ensemble modelling framework. This can be obtained with multi-ensemble simulations from a general circulation model (GCM). Such simulations will improve the distinction between the external forcing and the internal variability, and at the same time reduce the uncertainty of the signal (Bracco et al., 2004, Kucharski et al., 2013). To address these concerns, the present study intends to investigate the link between ENSO patterns and southern Africa drought by performing multi-ensemble simulations using SPEI to quantify drought.

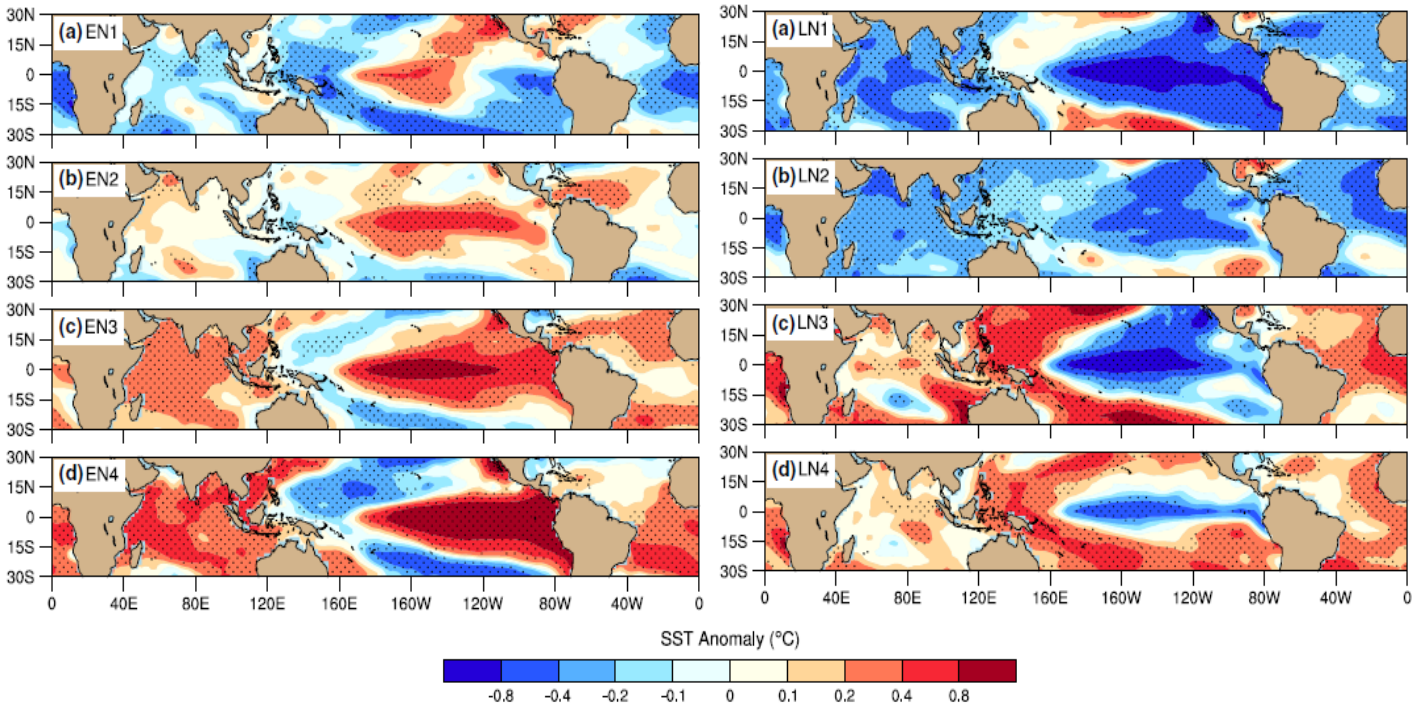

Figure 2.2 Composite SST anomalies (˚C) for El Niño and La Niña SST conditions during austral summer 1950 - 2010. Stippling indicates anomalies significant at $p < 0.05$ (Hoell *et al.*, 2015).

2.3 Simulating Teleconnections to Southern Africa Drought

The literature shows that climate modelling has become a popular approach for studying the climate system, particularly over Africa where observation data is often limited. While some studies have used climate models to understand the drivers of interannual rainfall variability in southern Africa (e.g. Richard *et al*., 2000; Reason, Jagadheesha & Tadross, 2003; Hansingo & Reason, 2009; Klutse *et al*., 2015), others have used them to improve seasonal forecasting (e.g. Landman & Goddard, 2002; Landman & Beraki, 2012) and to investigate the impacts of climate change (e.g. Joubert & Hewitson, 1997; Mason & Joubert, 1997; Abiodun *et al*., 2018). General Circulation Models (GCM) and Regional Climate Models (RCM) have both been used extensively to study southern Africa rainfall variability, however with varying levels of success. For example, Reason & Jagadheesha (2005) used a GCM to investigate the impacts of ENSO on southern Africa. While the GCM managed to accurately simulate large-scale modulations to the Walker Circulation over the Pacific and Indian Oceans, it struggled to capture regional circulation and precipitation anomalies associated with the Angola low. This arises due to the coarse horizontal resolution of GCMs (usually 100 - 300 km) which does not always capture the regional scale processes associated with precipitation sufficiently (Mason & Joubert, 1997; Landman & Beraki, 2012). This is an inherent problem of GCMs which can be addressed by using RCMs with higher resolution to downscale the GCM output. However, RCMs are not without their own shortcomings, particularly concerning lateral boundary conditions which can interfere with the ENSO teleconnections to southern Africa (e.g. Boulard *et al*., 2013; Meque & Abiodun, 2015). For instance, Meque & Abiodun (2015) evaluated the capability of RCMs in reproducing the link between ENSO and Southern Africa drought (SPEI). Despite the strong relationship found between ENSO and SPEI over southern Africa, several of the RCMs did not capture this signal. They concluded that in some cases GCMs can simulate the relationship between ENSO and southern Africa drought sufficiently, without the need to downscale.

Kucharski *et al*. (2013) highlight the importance of ensemble simulations to reduce uncertainty and create a more robust signal. Previous studies have usually approached this one of two ways: either they will use a multi-model approach (e.g. Dieppois, Rouault & New, 2015; Meque & Abiodun, 2015) or they perform multiple simulations using the same model with slight perturbations in the initial conditions (e.g. Dogar, Kucharski & Azharuddin, 2017). Due to the high

computational costs of complex GCMs, substantial ensemble simulations are usually only possible with GCMs of intermediate complexity, such as the ICTPAGCM, known as SPEEDY (Simplified Parameterizations, primitivE-Equation DYnamics) (Molteni, 2003; Kucharski, Molteni & Bracco, 2006). SPEEDY has been successfully used to simulate large-scale features like the Indian and African monsoons (e.g. Bracco *et al*., 2007; Kucharski *et al*., 2009; Kucharski *et al*., 2011; Feudale & Kucharski, 2013), East African rainfall variability (e.g. Bahaga *et al*., 2015) and ENSO studies (e.g. Yadav *et al.*, 2010; Bulić & Kucharski, 2012; Dogar, Kucharski & Azharuddin, 2017). Dogar, Kucharski & Azharuddin (2017) recently used SPEEDY to investigate the impact of ENSO on tropical and mid-latitude regions. They found that SPEEDY performed reasonably well in all regions (except South Asia), showing stronger ENSO impacts on tropical circulation (ITCZ, Hadley and Walker Circulation) which decrease (increased) precipitation over tropical Africa during El Niño (La Niña). Although SPEEDY has been used in many global studies, its capability in simulating southern Africa rainfall has not yet been evaluated, which is an objective of the present study. Previous studies (e.g. Zeng *et al*., 1999; Wang & Eltahir, 2000a; Wang & Eltahir, 2000b; Zeng & Yoon, 2009; Kucharski, Zeng & Kalanay, 2013) have identified that the climate variability can also be enhanced by vegetation interactions (e.g. evapotranspiration, albedo, roughness and leaf area index) which modify the atmospheric energy and water balance. While many studies have shown vegetation feedbacks to be important in the Sahel region (e.g. Zeng *et al*., 1999; Wang & Eltahir, 2000a; Wang & Eltahir, 2000b; Kucharski, Zeng & Kalanay, 2013), their role is unclear in southern Africa climate. Naik & Abiodun (2016) have shown that the southern Africa climate is sensitive to vegetation feedbacks, however Nicholson (2000) disagrees, stating that land-surface interactions are not present in the subcontinent. Therefore, this study will also assess the influence of coupling SPEEDY with a dynamic vegetation model.

Chapter 3: Data & Methodology

This chapter provides a description of the climate model used in this study as well as other datasets used in the evaluation of SPEEDY. A breakdown of the evaluation process is given as well as the model setup for the multi-forcing ensemble simulations.

3.1 Model Description

The model used in this study is the ICTPAGCM (version 41.5), known as SPEEDY (Simplified Parameterizations, primitivE-Equation DYnamics), developed at the Abdus Salam International Center for Theoretical Physics (ICTP) (see Molteni, 2003; Kucharski, Molteni & Bracco, 2006). It is an intermediate complexity model based on a hydrostatic spectral dynamical core (see Held & Suarez, 1994) and uses the vorticity-divergence form described by Bourke (1974). It has several simplified physical parameterization schemes including convection, large-scale condensation, vertical diffusion, short and longwave radiation and surface fluxes of momentum, heat and moisture. SPEEDY uses a mass flux scheme to represent convection processes, which is activated by the presence of conditional instability, and boundary layer fluxes are determined by stability-dependent bulk formulae. Additionally, SPEEDY is coupled with a simple one-layer thermodynamic model to determine land and ice temperature anomalies. Despite the simplified parameterizations, SPEEDY has reasonable performance and has been successfully implemented in a wide variety of climate research, including ENSO studies (e.g. Yadav *et al*., 2010; Bulić & Kucharski, 2012; Dogar, Kucharski & Azharuddin, 2017). Its computational efficiency and flexibility make it an ideal tool for this study. A more detailed description of SPEEDY is provided by Molteni (2003) and Kucharski *et al.* (2006) and information about the model versions, performance, users and access can be found at http://users.ictp.it/~kucharsk/speedy-net.html.

3.2 Data

SPEEDY simulations were conducted at T63 spectral truncation resolution (~ 1.875° x 1.875°) with 8 vertical levels, using monthly mean climatological SST data derived from ERA-Interim over the period 1979-2008 and observed SST anomalies from the Met Office Hadley Centre (HadISST). Studies (e.g. Zeng et al., 1999; Kucharski, Zeng & Kalnay, 2013; Li et al., 2018) have shown that vegetation dynamics (e.g. evapotranspiration, albedo, roughness and leaf area index)

can influence the climate by modifying the atmospheric energy and water balance. Therefore, it is important to incorporate vegetation feedbacks to enable two-way vegetation-climate interactions. This study used two different land-surface schemes: a dynamic vegetation scheme (SPEEDY-DV) and a non-dynamic vegetation scheme (SPEEDY-NDV). The SPEEDY-DV simulations coupled SPEEDY with the dynamic vegetation model VEGAS (Vegetation-Global-Atmosphere-Soil) which enabled fully interactive vegetation. VEGAS simulates the dynamics of vegetation growth and competition among four plant functional types (broadleaf tree, needleleaf tree, cold grass and warm grass) with different photosynthetic pathways (Kucharski, Zeng & Kalnay, 2013; Li et al., 2018). The SPEEDY-NDV simulations prescribed climatological vegetation cover and only coupled SPEEDY with land temperature and soil moisture changes.

Observed and simulated monthly climate data was used to evaluate the performance of the SPEEDY simulations. The observed data used in this study is from the Climate Research Unit (CRU). It consists of monthly climate data which has been re-gridded to a 0.5° x 0.5° spatial resolution. Monthly climate data from the National Center for Atmospheric Research (NCAR) Community Atmospheric Model version 5 (CAM5, spatial resolution ~ 1° x 1°) and the UK Met Office Hadley Centre Global Environment Model version 3 (HadGEM3, spatial resolution ~ 0.556° x 0.833°) were also included in the model evaluation. The CAM5 (see Angélil *et al.*, 2017; Stone *et al.*, 2018) and HadGEM3 (see Christidis *et al.*, 2013; Ciavarella *et al.*, 2017) simulations are from the Climate of the 20th Century Plus Detection and Attribution project (C20C+ D&A) undertaken by the World Climate Research Program's CLIVAR (available from https://portal.nersc.gov/c20c/). These historical ensemble simulations ("All-Hist") are CMIP5-style simulations forced with prescribed radiative forcing, sea surface temperatures and sea ice conditions (see Stone *et al.* 2019 for detailed experimental design). For consistency, all the simulated data (SPEEDY, CAM5 and HadGEM3) was re-gridded to the same resolution as CRU (0.5° x 0.5°) and only one ensemble member was used from CAM5 and HadGEM3.

3.3 Model Evaluation

The capability of SPEEDY in simulating the climate of southern Africa (5°E - 52°E; 0°S - 40°S) was evaluated over a historical period of 30 years (1979 - 2008). Throughout the model evaluation, we compared the SPEEDY simulations (SPEEDY-DV and SPEEDY-NDV) with CRU observation using statistical analysis. The inclusion of CAM5 and HadGEM3 served as a benchmark in order to compare the error of SPEEDY with the error of more complex GCMs with higher resolution. Analysis of the seasonal and spatial climate variability was done to evaluate the performance of SPEEDY over three distinct areas - tropical (30°E - 40°E; 0.5°S - 8°S), subtropical (25°E - 33°E; 18°S - 26°S) and semi-arid (15°E - 23°E; 22°S - 30°S) (Figure 3.1). This study focused on the austral summer season (December - February, DJF) as this is the main rainy season for the majority of southern Africa (Tyson & Preston-Whyte, 2000; Davis, 2011). The climate variables which were analyzed include temperature (mean, maximum and minimum), precipitation, potential evapotranspiration (PET) and the climate moisture balance (CMB). CMB is the difference between precipitation and PET, taking into account the influence of both precipitation and temperature. There are various formulations to calculate PET, including Hargreaves, Thornthwaite, and Penman-Monteith methods. In this paper PET will be calculated using the Hargreaves method.

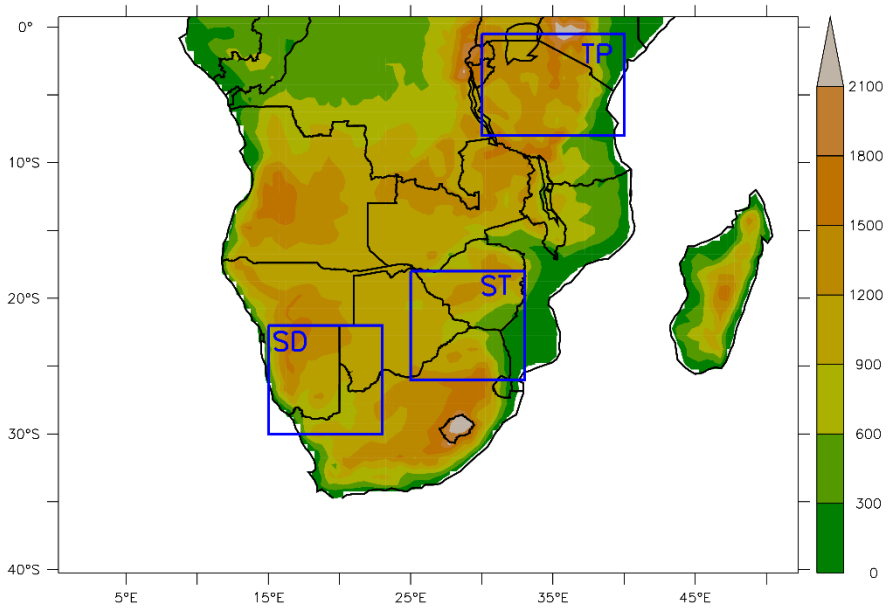

Figure 3.1 The study domain showing southern African topography and the selected three areas for model evaluation. The designated areas are semi-arid (SD), subtropical (ST) and tropical (TP)

SPI and SPEI were used in this study to identify meteorological drought (3-month timescale). SPI (SPEI) is obtained by fitting a gamma (log-logistic) distribution to precipitation (CMB) and is a measure of the standardized deviation from the long term mean. This provides an indication of the intensity of dryness on a scale from -2 to 2, with negative (positive) values depicting dry (wet) conditions. The advantage of using SPEI over SPI is the inclusion of evapotranspiration which has been shown to play a crucial role in drought severity (Meque & Abiodun, 2015; Ujeneza & Abiodun, 2015). SPEI and SPI were computed at a 3-month scale over southern Africa using the SPEI library available in R software (Beguería and Vicente-Serrano 2013).

In order to evaluate the capability of SPEEDY in capturing the impact of tropical Pacific ENSO SST anomalies on southern Africa climate, the Multivariate ENSO Index (MEI) was used. This is a bimonthly ENSO index where positive values indicate El Niño phases and negative values indicate La Niña phases. It is determined by six climate variables (pressure, zonal and meridional winds, SST, surface air temperature and total cloudiness) measured over the tropical Pacific Ocean. In this study, the temporal correlation was calculated between MEI and various climate variables (SPEI, precipitation and PET) to determine if SPEEDY could capture the fundamental influence of ENSO on summer climate in southern Africa.

There is high variability between ENSO events, therefore we also evaluated the capability of SPEEDY in simulating the impact of specific patterns of ENSO on southern Africa drought (SPEI). This study used eight ENSO patterns that were previously defined by Johnson (2013) through self-organizing map analysis. They consist of four El Niño SST conditions (EN1 - EN4) and four La Niña SST conditions (LN1 - LN4) which are statistically distinct in terms of the magnitude and position of the associated SST anomalies in the tropical Pacific Ocean. Johnson (2013) also identified the years in which each ENSO pattern occurred for the period 1950-2011. The capability of SPEEDY in reproducing the mean SPEI associated with each ENSO pattern was evaluated. However, due to the limited time frame of the CRU, CAM5 and HadGEM3 data, only two events per ENSO pattern were considered to ensure consistency. The two events which occurred in all the datasets and had the highest MEI were selected for this analysis.

Table 3.1 Austral summer occurrences of El Niño and La Niña SST conditions (from Johnson, 2013)

EN1	EN2	EN3	EN4	LN1	LN2	LN3	LN4
1953-1954	1951-1952	1957-1958	1972-1973	1950-1951	1956-1957	1998-1999	1983-1984
1958-1959	1963-1964	1965-1966	1982-1983	1954-1955	1964-1965	1999-2000	1995-1996
1977-1978	1968-1969	1986-1987	1997-1998	1955-1956	1971-1972	2007-2008	2000-2001
	1969-1970	1987-1988		1970-1971	1974-1975	2010-2011	2005-2004
	1976-1977	1991-1992		1973-1974			
	2004-2005	1994-1995		1975-1976			
		2002-2003		1988-1989			
		2006-2007					
		2009-2010					

3.4 Experimental Design

This study used eight ENSO SST patterns previously identified by Johnson (2013) and Hoell *et al.* (2015) through self-organizing map analysis (Figure 2.2). They consist of four El Niño conditions (EN1 - EN4) and four La Niña conditions (LN1 - LN4) which are statistically distinct in terms of the magnitude and position of the associated SST anomalies in the tropical Pacific Ocean. Johnson (2013) also identified the years in which each ENSO pattern occurred for the period 1950-2011 (Table 3.1). The global SST composites for each ENSO pattern were created by averaging the HadISST data for the years in which that pattern occurred (as identified by Johnson, 2013). There are some notable differences between the ENSO SST patterns which are discussed in detail in Hoell *et al.* (2015). The El Niño SST patterns (EN1 – EN4) show a significant warm anomaly in the tropical Pacific Ocean, with increasing size and intensity from EN1 to EN4. The warm SST anomaly has a more central position during EN1, EN2 and EN3, characteristic of Central Pacific ENSO, whereas EN4 is characteristic of Eastern Pacific ENSO with the warm anomaly extending across the eastern Pacific Ocean (Hoell *et al.*, 2015). The western Pacific Ocean is characterized by significant cool SST anomalies during EN1, EN3 and EN4. EN1 also features cool SST anomalies in the Indian Ocean and tropical Atlantic Ocean, whilst EN3 and EN4 display significant warm SST anomalies in these ocean basins. The warm Indian Ocean SST anomalies in EN4 are

characteristic of a positive Indian Ocean dipole. EN2 shows minimal SST anomalies in the Atlantic Ocean, Indian Ocean and western Pacific Ocean (Hoell *et al.*, 2015). The La Niña SST patterns (LN1 – LN4) are characterized by significant cool SST anomalies across the central and eastern Pacific Ocean, with decreasing size from LN1 to LN4. LN1 and LN2 are classified as Eastern Pacific ENSO events, while LN3 and LN4 are classified as Central Pacific ENSO events (Hoell *et al.*, 2015). Significant warm SST anomalies are present in the western Pacific Ocean, tropical Atlantic Ocean as well as parts of the Indian Ocean during LN3 and LN4, with LN3 featuring a significant negative Indian Ocean Dipole. In contrast, LN1 and LN2 feature cool SST anomalies across the Atlantic Ocean, Indian Ocean and western Pacific Ocean, except for the western Pacific Ocean in LN1 which shows no significant SST anomalies.

In this study, eight sensitivity experiments were conducted - one for each ENSO SST pattern. In each case, SPEEDY was forced with the composite global SST anomalies associated with that pattern. Each experiment consisted of a 50-member ensemble with perturbations in the start date. We simulated an 18-month period (July to the following December) for each ensemble member whereby the ENSO anomaly occurred during the interim DJF period, which was the focus of our analysis. Through the evaluation it was seen that the simulation with the non-dynamic vegetation scheme performed better and was therefore used in these sensitivity experiments. In order to investigate the link between southern Africa drought and the ENSO patterns, SPEI, SPI and the atmospheric dynamics were analysed. This analysis included anomalies in the vertical motion, mean sea level pressure (MSLP), horizontal winds, velocity potential, eddy stream function and integrated moisture flux with statistical significance determined through a student t-test (99^{th} percentile).

Chapter 4: Model Evaluation

This chapter provides the results of the model evaluation. The capability of SPEEDY in simulating southern Africa climate is discussed. Complex GCMs are also included in the analysis to provide a 'benchmark' of GCM error. Two vegetation schemes are compared (dynamic and non-dynamic) and the capability of SPEEDY in reproducing the link between ENSO and southern Africa drought is also evaluated.

4.1 Annual cycle of climate variables over selected areas

In general, SPEEDY captures the annual cycle of the southern Africa climate well (Figure 4.1). As in CRU observation, the model simulates a warm wet summer season (December, January and February) and a cold dry winter season (June, July, August) characteristic of the selected three areas, although the simulated annual cycle is about one month earlier than observed, as evident in the temperature (Figure 4.1 a, b, d, and e) and precipitation (Figure 4.1 j, k, and l) cycles. In the tropical (TP) area, SPEEDY credibly simulates the observed temperatures, which show low annual variability, as well as the bimodal rainfall pattern, which is driven by the seasonal movement of the Intertropical Convergence Zone (ITCZ) that controls the seasonal rainfall over most parts of southern Africa. In agreement with CRU, SPEEDY shows that the tropical area experiences its first rainy season in September to November (during the southward progression of the ITCZ) and its second rainy season in February to April (during the northward retreat of ITCZ). The model also reproduces the relatively low precipitation over the semi-arid area (relative to the other two areas), caused by a lack of moisture in the atmosphere due to the nearby cold Benguela current and dry continental winds.

Nevertheless, there are some noticeable biases in the seasonal cycle produced by SPEEDY. Generally, the model produces a warm and wet bias across the region (Figure 4.1). In the subtropical and semi-arid areas the warm bias varies throughout the year (Figure 4.1 b, c, e, f, h, i), typically showing the least bias in the summer months (~ 0˚C - 2˚C) and the highest bias in the winter months (~ 3˚C – 5˚C). On the other hand, SPEEDY simulates minimal temperature bias in the tropical area (Figure 4.1 a, d, g). In terms of precipitation, the subtropical area shows maximum precipitation bias during the spring (~ 100mm/month; Figure 4.1 k), whilst the semi-arid area

shows precipitation bias throughout the year (30 – 100mm/month; Figure 4.1 l), reaching maximum in the summer (DJF). However, the tropical area shows the biggest precipitation bias, particularly during the two rainy seasons (September – November and February - March) for which SPEEDY simulates more than double that of CRU observed precipitation (100 – 180mm/month; Figure 4.1 j). SPEEDY simulates PET relatively well in both the subtropical and semi-arid areas, showing notably less error than the CAM5 and HadGEM3 simulations. However, in the tropical area SPEEDY underestimates PET, although this is not dissimilar to the more complex models. The simulated SPEEDY CMB reflects the above analysis by a shift in the climatology of one month and overestimation of the CMB due to high simulated values of precipitation. However, these results are similar if not better than the complex models (CAM5 and HadGEM3), particularly in the subtropical and semi-arid areas during the summer. The biases in SPEEDY simulations could be due to the coarse resolution, the simplified parameterization schemes. However, the error is comparable to more complex models and when considering the computational efficiency and flexibility of SPEEDY, it has reasonable performance.

The performance of SPEEDY depends upon the vegetation scheme used. While the simulation with dynamic vegetation (SPEEDY-DV) and the one without dynamic vegetation (SPEEDY-NDV) show similar performance across the three selected areas, the SPEEDY-NDV performs better than SPEEDY-DV in most instances, especially in the tropical and subtropical areas. For instance, the SPEEDY-NDV shows less bias than SPEEDY-DV in simulating summer precipitation in the tropical area (about 50 mm month^{-1}; Figure 4.1 j), summer and autumn temperature in the subtropical area (1^{o}C; Figure 4.1 e), and winter temperature in the semi-arid area (1^{o}C; Figure 4.1 f and i). However, SPEEDY-DV features a better performance than SPEEDY-NDV in reproducing maximum temperature in the tropical area (1^{o}C; Figure 4.1 d). Overall, SPEEDY performs better without the dynamic vegetation scheme. This implies that the implementation of dynamic vegetation scheme in SPEEDY does not improve the performance of the model in southern Africa. In theory, the dynamic vegetation option should perform better than the static vegetation (Strengers *et al*., 2010; Li *et al*., 2018), and several studies have shown that the southern Africa climate is sensitive to changes in vegetation (Naik, 2015).

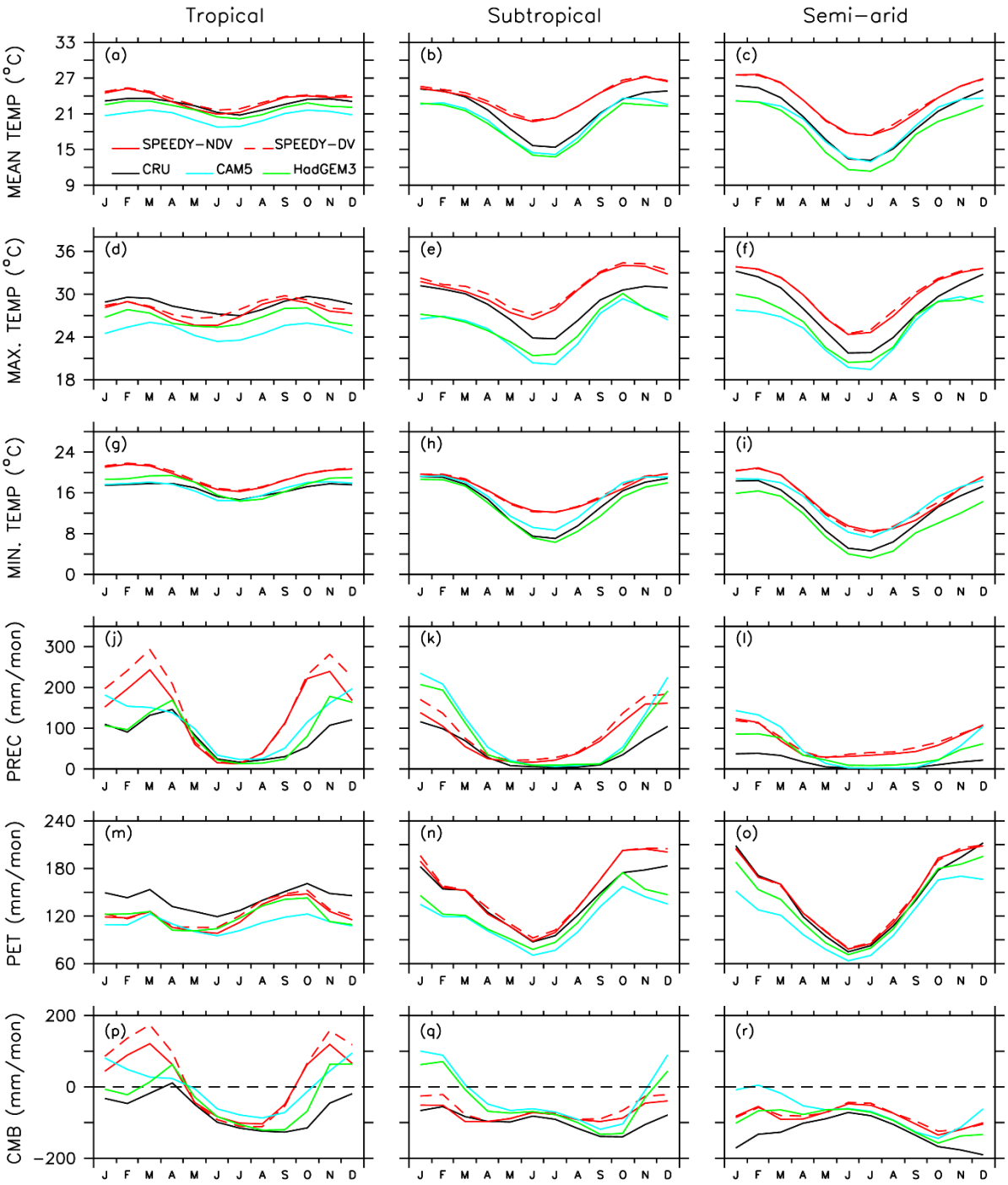

Figure 4.1 The annual cycle of temperature (mean, max and min), precipitation (prec), potential evapotranspiration (PET) and climate moisture balance (CMB) over the three selected areas: semi-arid (SD), subtropical (ST) and tropical (TP) in southern Africa (1979 – 2008), as observed by CRU and simulated by SPEEDY (dynamic and non-dynamic vegetation versions: SPEEDY_DV and SPEEDY_NDV) and other more complex GCMs (HadGEM3 and CAM5)

4.2 Spatial distribution of climate variables over southern Africa

SPEEDY generally captures the spatial distribution of the climate variables across southern Africa in the summer (DJF). It gives a realistic representation of the spatial pattern of temperature with high correlation (r = 0.8), albeit with some temperature bias (Figure 4.2). The spatial pattern of temperature across the region is largely determined by the topography (Figure 3.1), with both CRU and SPEEDY showing lower temperatures in areas of higher altitude, such as the Drakensberg mountain range and the East African Rift. The ocean currents also have an influence on the climate in the coastal regions (Nicholson & Entekhabi, 1987). SPEEDY simulates moderate temperatures and low precipitation along the western coast of the Namib Desert, and intensified temperatures and precipitation along the tropical eastern coast. This is expected because of the cold Benguela current and warm Agulhas/Mozambique current, respectively. Elements of the spatial distribution of summer precipitation are slightly captured in the SPEEDY simulations (r = 0.6), although it is highly variable. SPEEDY captures the southern position of the ITCZ during January, which drives most of the summer precipitation in southern Africa. Other summer rain-bearing systems which are suggested in the SPEEDY simulations include the Angola-Kalahari trough, the tropical temperate trough (TTT, which lies diagonally across the subcontinent).

However, SPEEDY produces some notable biases in the spatial distribution of summer climate variables (Figure 4.2). The warm and wet bias seen in Figure 4.1 is evident across most of the region (Figure 4.2). A substantial precipitation bias (about 300 mm month^{-1}) located over southern Tanzania, Zambia and southern DRC, which suggest that SPEEDY simulates stronger ITCZ convergence. This has been reported globally in Dogar, Kucharski & Azharuddin (2017) who also reported a precipitation bias located diagonally across the subcontinent in their SPEEDY simulations. Their simulations were performed at T30 resolution, which confirm that the precipitation bias is not a result of increased sensitivity to topography at the higher T63 resolution. The precipitation bias could be a result of SPEEDY simulating a stronger tropical temperate trough, or the warm bias in the region causing enhanced convection and increased precipitation over Botswana. The more complex models, CAM5 and HadGEM3, also show a precipitation bias in these regions, although the magnitude is not as large that of SPEEDY; they also simulate a more realistic spatial distribution (r = 0.7 and r = 0.8 respectively).

SPEEDY shows the warm bias (mean temp and min temp) predominantly over the western half of the subcontinent, especially over the Kalahari Desert region and the Congo basin. There is a slight cool bias in minimum temperature (Figure 4.2 g and h) over the Drakensberg region of South Africa, although this doesn't seem to affect precipitation in the region which is orographically driven. The warm bias in maximum temperature is not as widespread and is notably weaker in parts of southern Africa, although there is a significant bias along the western coast and Mozambique (Figure 4.2 l and m). However, the bias along the western coast is also evident in the more complex models, CAM5 (HadGEM3 and CAM5). The model bias (with reference to CRU) is shown in contours while the coefficient of spatial correlation (r) between the simulation and observation is indicated in brackets and HadGEM3. The PET is largely influenced by the maximum temperature bias as it is used in the Hargreaves method for calculating PET.

The SPEEDY simulations show a slight negative bias in PET in the northern region and a more notable positive bias along the coastal regions in the SPEEDY simulations. However, the PET bias is minimal and the spatial correlations are more comparable to CAM5 and HadGEM3. The SPEEDY CMB outputs are also relatively poor and erratic as they are entirely dependent on precipitation and PET. The SPEEDY simulation without dynamic vegetation (SPEEDY-NDV) shows a slightly weaker temperature bias over the equatorial region, although there is no difference between the correlations of SPEEDY-NDV and SPEEDY-DV. There is also no significant difference in the spatial pattern of SPEEDY-DV and SPEEDY-NDV when simulating summer precipitation ($r = 0.6$), however the simulation with dynamic vegetation (SPEEDY-DV) has a slightly better correlation when simulating PET ($r = 0.7$).

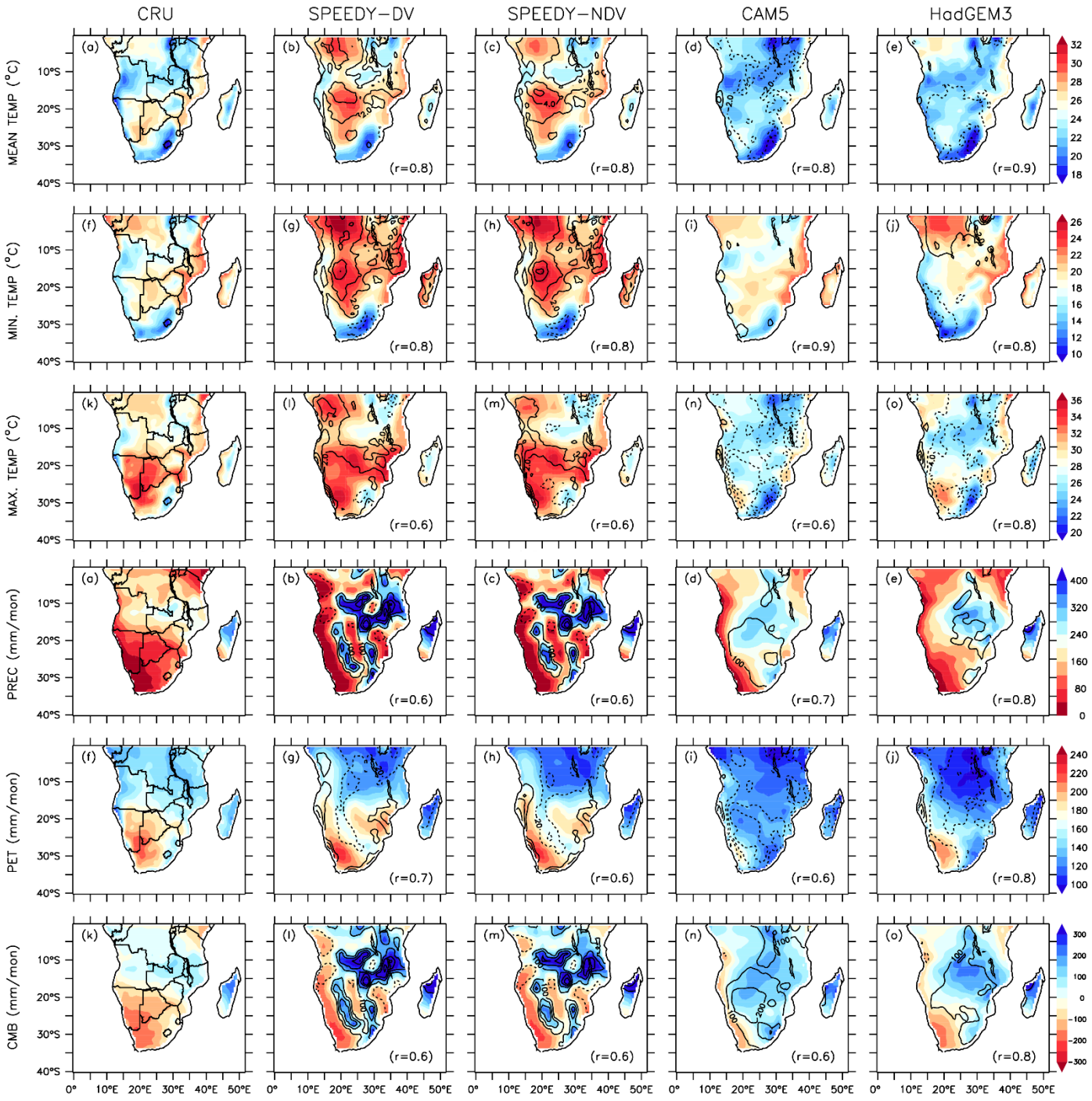

Figure 4.2 The spatial variation of DJF temperature (mean, max and min), precipitation (prec), potential evapotranspiration (PET) and climate moisture balance (CMB) over southern Africa (1979 – 2008), as observed by CRU and simulated by SPEEDY (dynamic and non-dynamic vegetation versions: SPEEDY_DV and SPEEDY_NDV) and other more complex GCMs

4.3 SPEI variability over southern Africa

SPEEDY captures the interannual variability of summer SPEI with varied capability across regions in southern Africa (Figure 4.3 and 4.4). The model features its worst performance in the tropical area with correlation as low as 0.1 and 0.2 (for SPEEDY-DV and SPEEDY-NDV, respectively) and a low normalized standard deviation of ~0.63 (for both SPEEDY-DV and SPEEDY-NDV). In most cases it underestimates the SPEI or produces the wrong signal altogether. Most notable in Figure 4.3 is the peak in 1998 and the low in 1999 – 2000, which corresponds with a strong El Niño and La Niña event, respectively, which SPEEDY was unable to capture. The performance of SPEEDY is notably better in the subtropical area with correlation ranging between 0.2 and 0.4. SPEEDY manages to capture most of the variation with high normalized standard deviation (SPEEDY-DV = ~0.9 and SPEEDY-NDV = ~1.05). It is important to note that SPEEDY exaggerated the negative signal in 1995 and 1998, which corresponds with El Niño events. Despite the strong El Niño in 1998, it had little impact in southern Africa (Tyson & Preston-Whyte, 2000; Hoell et al., 2017) as shown by the CRU result. SPEEDY has average performance in the semi-arid area with correlation between 0.1 and 0.3 for SPEEDY-DV and SPEEDY-NDV, respectively. It has less variability than CRU observation, with normalized standard deviations of ~0.85 and ~0.9. Overall the correlations are relatively low and SPEEDY doesn't always capture the correct signal, but the results, particularly the SPEEDY-NDV simulation, are comparable to the more complex models, CAM5 and HadGEM3.

SPEEDY generally captures the observed correlations with Multivariate ENSO Index (MEI). As Figure 4.5 shows, a positive (negative) MEI is associated with negative (positive) SPEI, low (high) precipitation and high (low) evapotranspiration, which is characteristic of El Niño (La Niña) and drought (heavy rainfall) in the region. SPEEDY manages to simulate a reasonable representation of this relationship ($r = 0.3 – 0.5$), nevertheless, there are some biases. These biases are particularly noticeable in the equatorial region and typically consist of a weaker and sometimes opposite correlation being simulated across all three variables (SPEI, PREC and PET). However, the more complex models, CAM5 and HadGEM3, show similar biases and are even bigger in some cases (e.g. CAM5). SPEEDY-NDV generally has less bias than SPEEDY-DV, particularly when correlating MEI and SPEI. This is reflected in the spatial correlation where SPEEDY-NDV performs significantly better ($r = 0.5$ and $r = -0.1$ respectively). SPEEDY-NDV also has better

correlation than CAM5, however falls short when compared to the more complex HadGEM3 model.

SPEEDY generally captures the correct signal of SPEI for each of the ENSO patterns. As expected in the southern region, it produces a negative SPEI during the El Niño SST conditions (Figure 4.6), indicating dry conditions, and positive SPEI during the La Niña SST conditions (Figure 4.7), indicating wet conditions. The opposite occurs in the equatorial region with a positive signal for the El Niño SST conditions and negative signal for the La Niña SST conditions. EN4 produces the strongest and most widespread dry conditions, which corresponds with the results of Hoell *et al*. (2015). Nevertheless, there are some notable biases. SPEEDY tends to simulate a negative bias for all the El Niño SST conditions, which is mostly concentrated over the eastern equatorial region. However, there is a notable positive bias in the Congo basin in EN1 and EN2. EN2 also shows a distinct positive bias along the western coast which is indicative of the Angola-Kalahari trough, which was also seen in the precipitation bias in Figure 4.2. The SPEEDY-DV simulation also shows a positive bias in the south-western region for EN3 and EN4. On the other hand, SPEEDY generally simulates a negative bias in the southern region and a positive bias in the northern region for the La Niña SST conditions. The positive bias seen in the La Niña SST conditions is similar to the precipitation bias seen in Figure 4.2. Although HadGEM3 has higher correlation with CRU observation in most cases, it produces similar biases as those seen in the SPEEDY simulations. Overall the SPEEDY-NDV simulation produces a more realistic result and performs better than the SPEEDY-DV simulation in terms of spatial correlation.

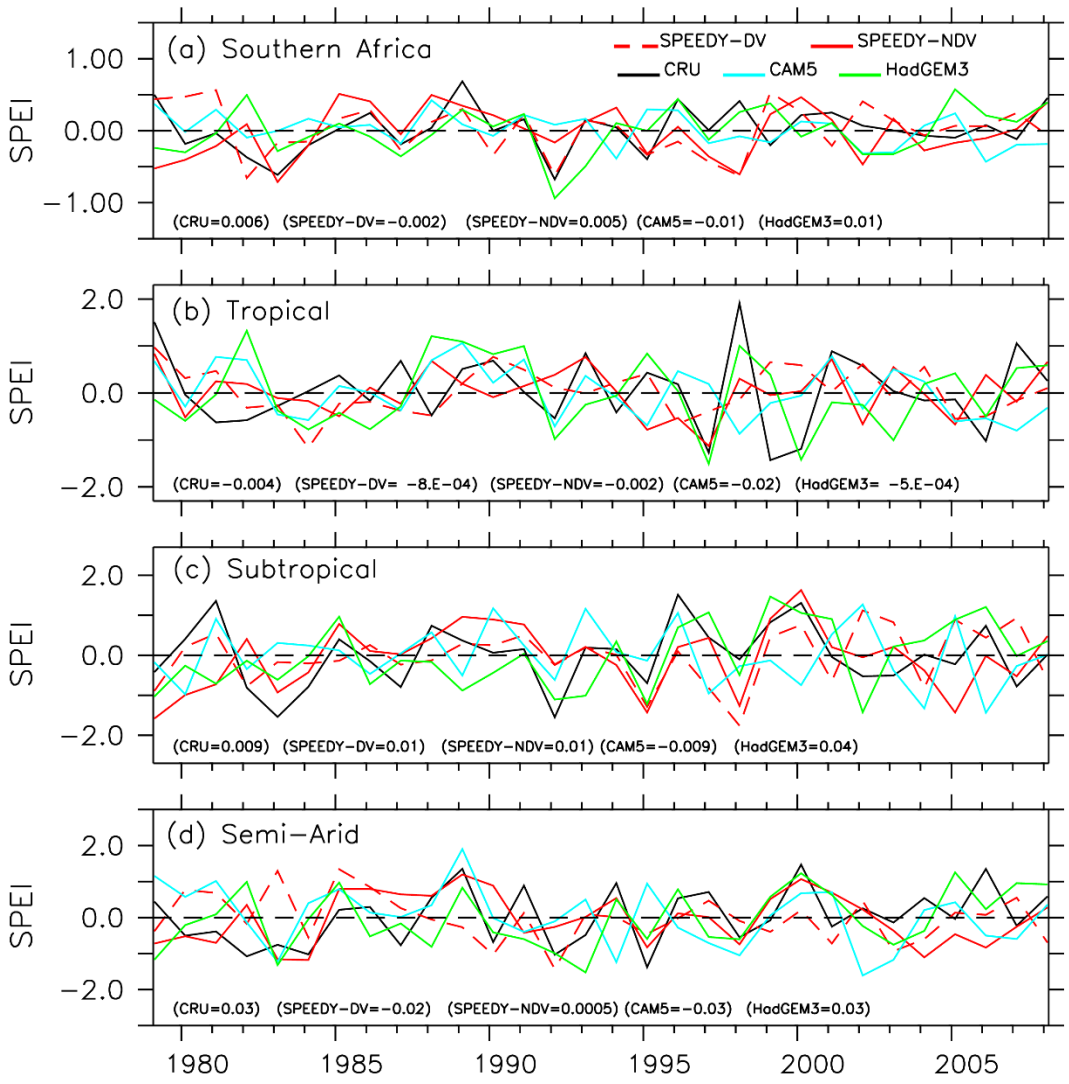

Figure 4.3 Time-series of 3-month DJF SPEI over (a) southern Africa, (b) the tropical area, (c) subtropical area and (d) semi-arid area in the period 1979 – 2008, as observed by CRU and simulated by SPEEDY (dynamic and non-dynamic vegetation versions: SPEEDY_DV and SPEEDY_NDV) and other more complex GCMs (HadGEM3 and CAM5). The trend of each time series is indicated in brackets

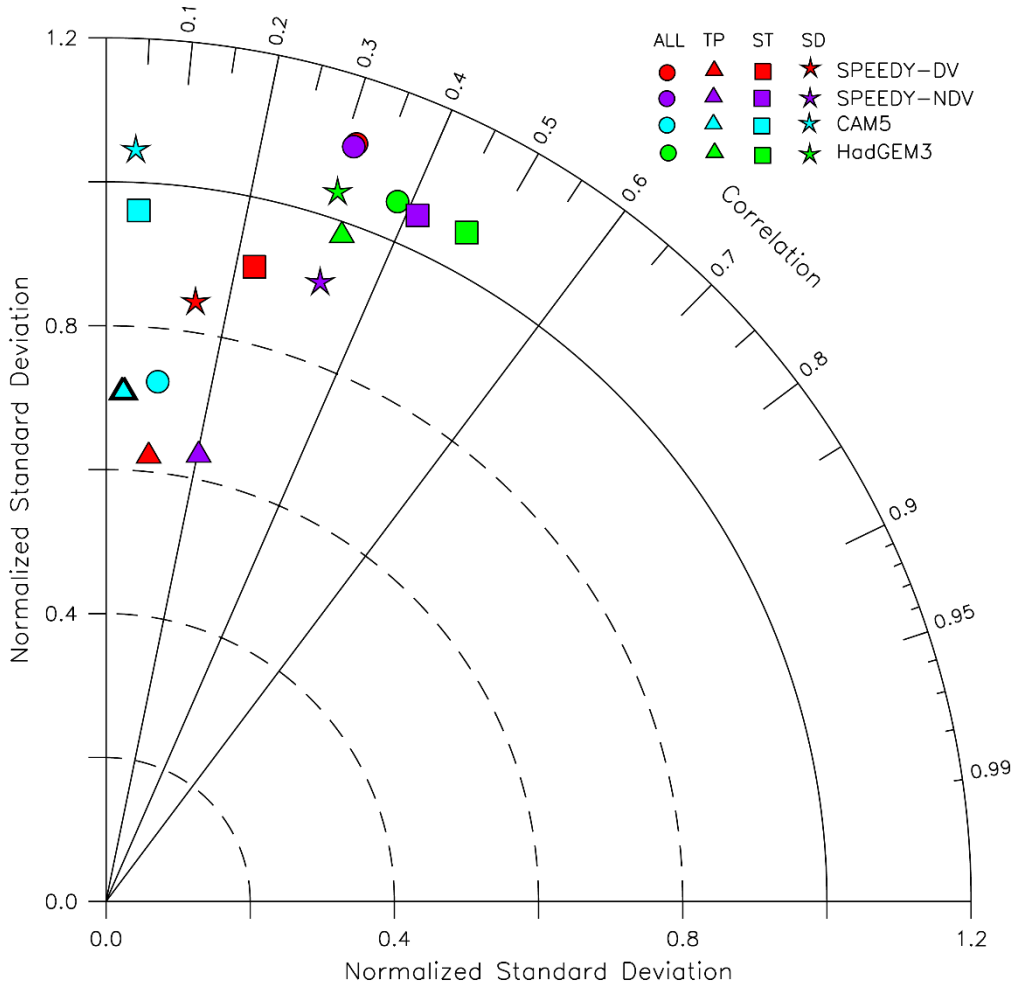

Figure 4.4 Taylor diagram for comparing the observed (CRU) and simulated (CRU SPEEDY-DV, SPEEDY-NDV, CAM5 and HadGEM3) 3-month DJF SPEI over southern Africa, the tropical area (TP), subtropical area (ST) and semi-arid area (SD) from 1979 – 2008. Note: the bold triangle for TP CAM5 indicates negative correlation

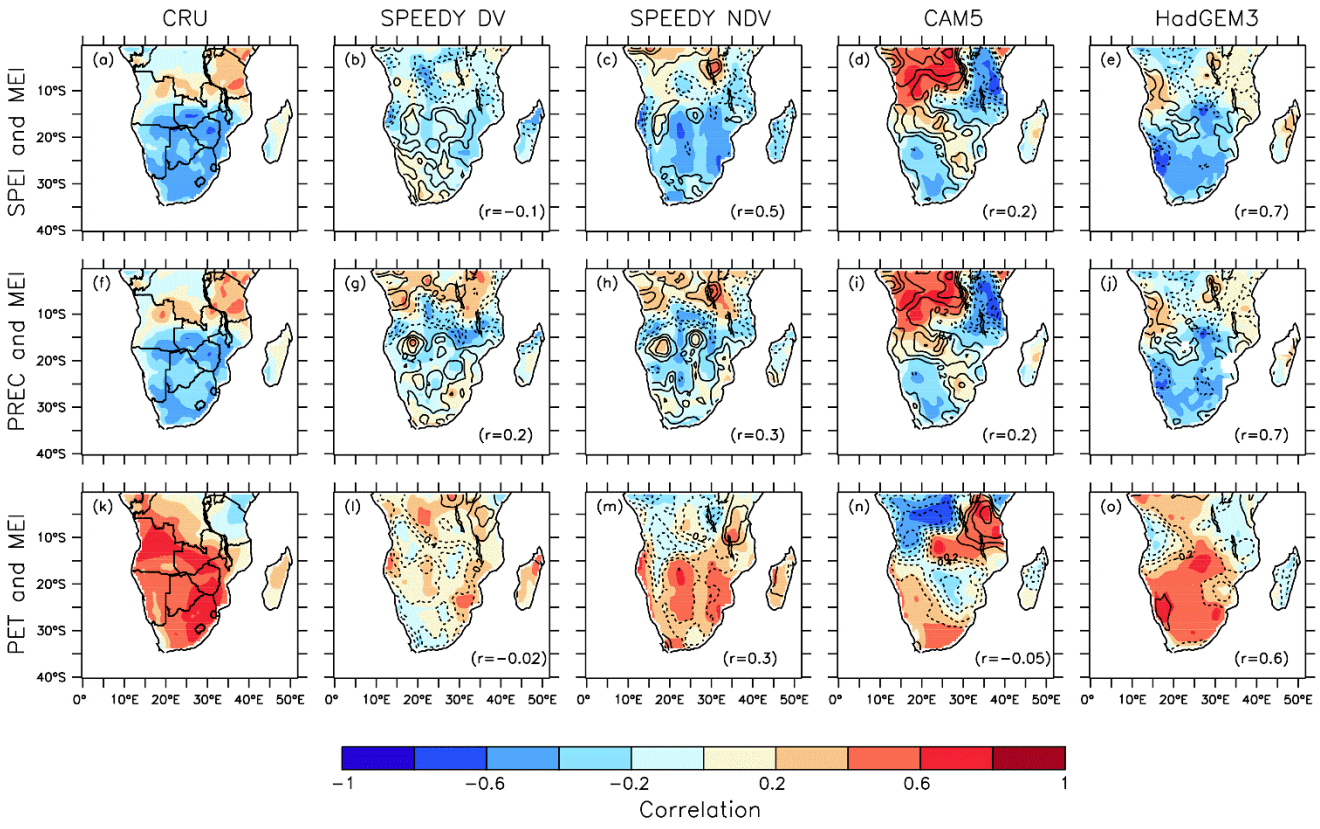

Figure 4.5 The spatial distribution of temporal correlation of MEI with 3-month SPEI, precipitation, and PET for the summer season (DJF) during the period 1979 – 2008, as observed by CRU and simulated by SPEEDY (dynamic and non-dynamic vegetation versions: SPEEDY_DV and SPEEDY_NDV) and other more complex GCMs (HadGEM3 and CAM5). The contours show the correlation bias at intervals of 0.2 and the spatial correlation (r) between the simulation and observation is indicated in brackets

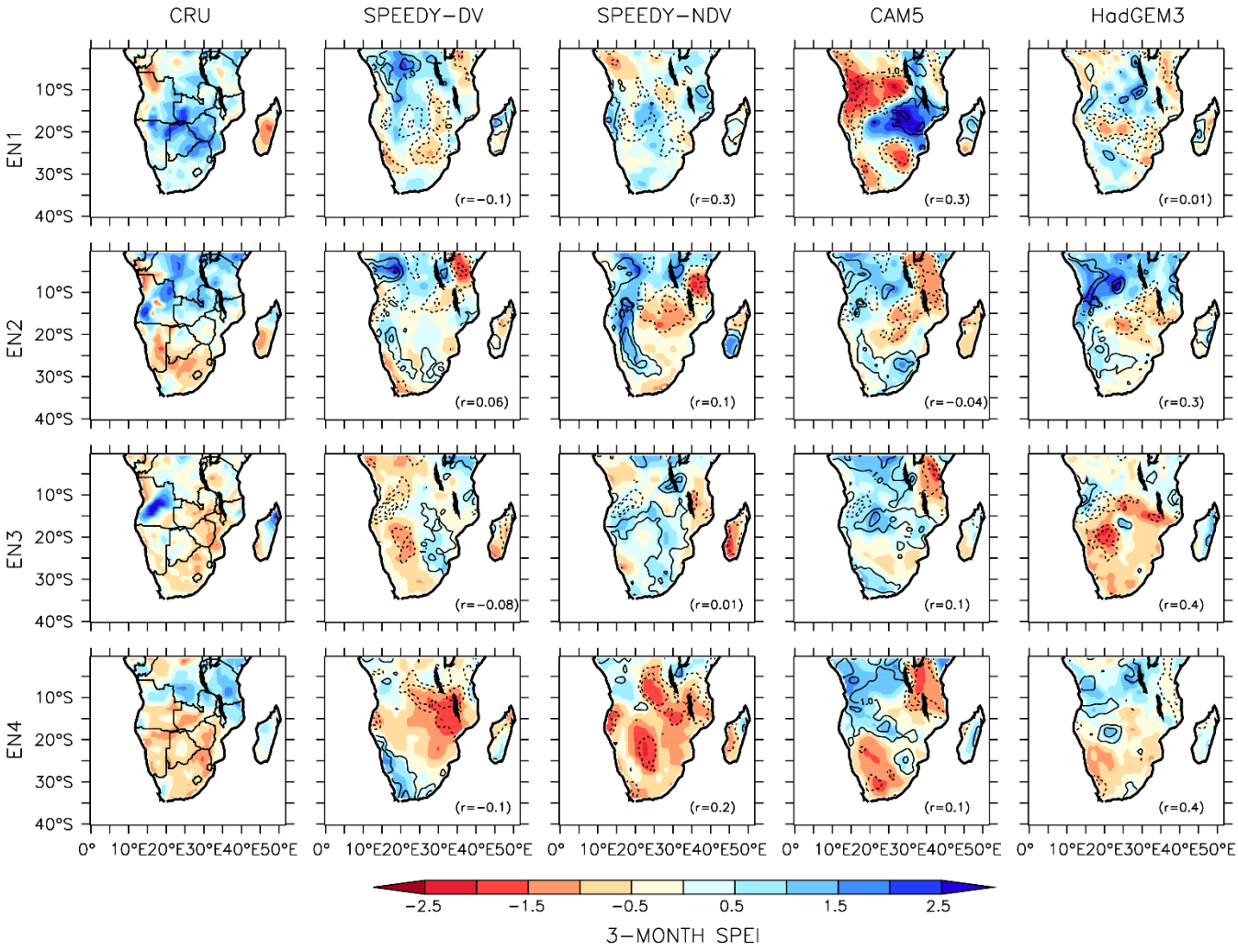

Figure 4.6 Spatial distribution of average DJF 3-month SPEI for two events from each of the El Niño SST conditions occurring between 1950 – 2010 as observed by CRU and simulated by SPEEDY (dynamic and non-dynamic vegetation versions: SPEEDY-DV and SPEEDY-NDV) and other more complex models (CAM5 and HadGEM3). The contours show the SPEI bias and the spatial correlation (r) between the simulation and observation is indicated in brackets. Note: due to the time period of the CAM5 and HadGEM3 datasets, only one event was used for the EN1 pattern

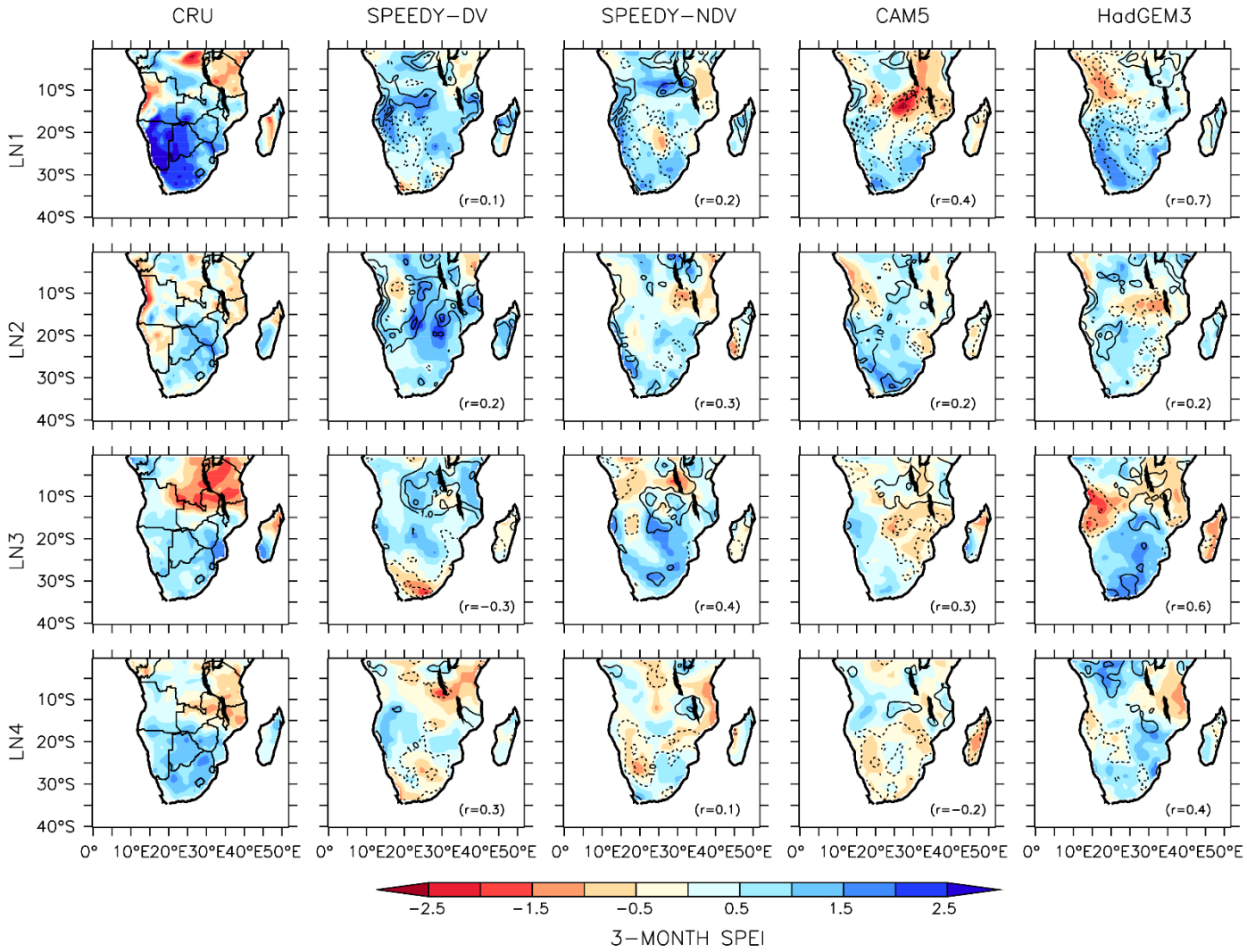

Figure 4.7 Same as figure 4.6, but for two events from each of the La Niña SST conditions

Chapter 5: Results & Discussion

Chapter 5 presents the results of the multi-forcing ensemble simulations. The sensitivity of southern Africa drought to eight different ENSO conditions is discussed and the robustness of the signal is analyzed. The atmospheric dynamics that link each ENSO condition with southern Africa drought is then investigated further. Section 5.1 focuses on the El Niño SST conditions, whilst Section 5.2 focuses on the La Niña SST conditions.

5.1 El Niño

5.1.1 Drought associated with El Niño SST conditions

The spatial pattern and intensity of SPEI drought varies between the El Niño SST conditions (Figure 5.1). EN1 and EN2 (Figure 5.1 a and b) show SPEI drought in the equatorial area, with significant values over Angola and Tanzania. This contradicts some previous studies (Tyson & Preston-Whyte, 2000; Cook, 2001; Hoell *et al*., 2015) that attributed El Niño SST conditions with a wet anomaly in the eastern equatorial region. On the other hand, EN3 and EN4 (Figure 5.1 c and d) show significant SPEI drought condition along the south west of the region, as well as increased drought across central Mozambique and Madagascar. All the conditions show a similar positive SPEI across Botswana and north eastern South Africa, however, these wet conditions are not seen in the results of Hoell *et al*., (2015), except in EN1. This discrepancy may be a result of the precipitation bias in the SPEEDY simulation, as shown in Figure 4.2. There are few differences when comparing the results of SPEI with SPI. The most notable difference is that SPI shows less drought intensity along the western coastline in EN2, EN3 and EN4 (Figure 5.1 f, g and h). This agrees with the results of Meque and Abiodun (2015), which indicate that temperature has a stronger relationship with ENSO in the semi-arid area, whereas the tropical area has a stronger relationship with precipitation.

Although there are similarities in the ensemble spread, there are some notable differences between the El Niño SST conditions across the different areas (Figure 5.2). In the tropical area there is relatively strong agreement within the ensemble spread, where at least 75% of the ensembles have a negative SPEI for EN1, EN2 and EN3 (Figure 5.2 a). However, this contradicts the literature

(Tyson & Preston-Whyte, 2000; Hoell *et al*., 2015) that found a wet anomaly in this area during El Niño phases. This is also seen in the CRU observation which typically shows positive SPEI values. Despite this, the CRU observation generally falls within the upper quartile of the ensemble spread. The signal of EN4 in the tropical area remains fairly uncertain. In the subtropical area, most of the ensembles (> 50%) have a positive SPEI for EN1, EN2 and EN3, which is unexpected as drought typically occurs in this area during El Niño phases (Tyson & Preston-Whyte, 2000; Hoell *et al*., 2015). As previously mentioned, this is likely due to the SPEEDY precipitation bias in this area. CRU observation highlights this as well, with most of the observed SPEI falling within the lower two quartiles and below. However, this is not the case for EN1 which only shows positive values for observed SPEI. The semi-arid area shows the biggest ensemble spread and the most uncertainty in the signal. Only EN4 shows some certainty with 75% of the ensembles below zero. The model simulation for this area also has the best agreement with CRU observation, with most of the observations falling within the ensemble range. In the subtropical and semi-arid areas, there is a decrease in the ensemble spreads when only considering precipitation (SPI; Figure 5.2b). This creates a slightly more robust signal, particularly with EN1 and EN3. Overall, EN2 produces the strongest drought (lowest SPEI) in the tropical area, whereas EN4 shows the strongest drought in the subtropical and semi-arid areas, although the signal in the subtropical area is uncertain. These results suggest that the scale at which SPEEDY captures the ENSO signal may be larger than the dimensions of the 3 areas (tropical, subtropical and semi-arid).

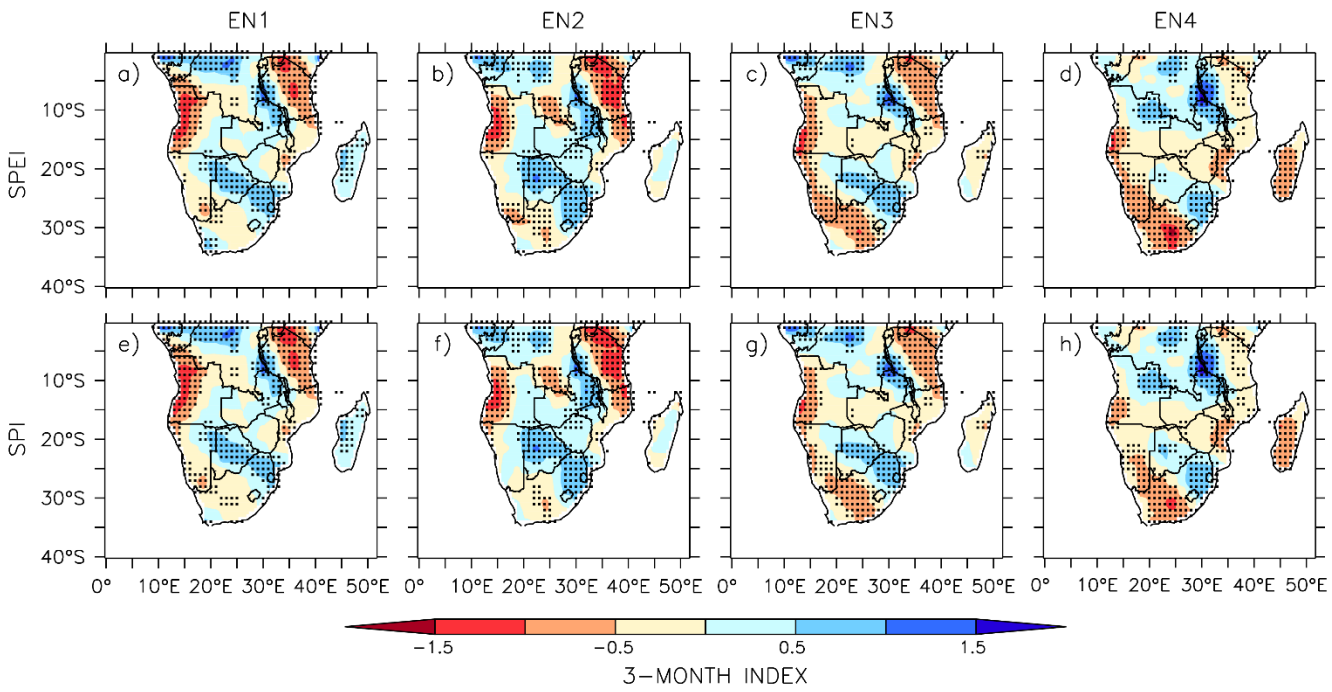

Figure 5.1 Ensemble mean of the DJF 3-month SPEI and SPI for the El Niño SST conditions. Stippling indicates values significant at the 99th percentile

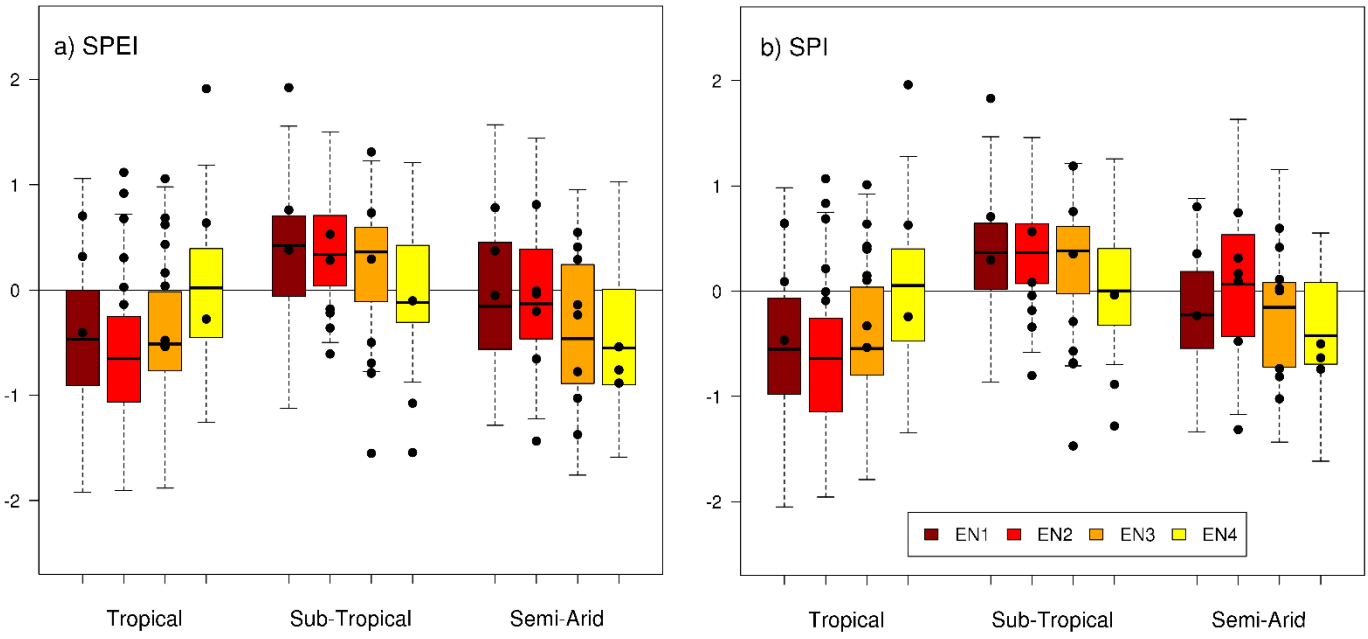

Figure 5.2 Boxplots showing the ensemble spread of the DJF 3-month SPEI and SPI for the El Niño SST conditions in the three areas: tropical, subtropical and semi-arid. The black dots indicate the observed events for each pattern from CRU data

5.1.2 Atmospheric Dynamics of El Niño SST conditions

In order to assess the differences between the ENSO conditions and their associated atmospheric teleconnections, the mean sea level pressure (MSLP), divergent (velocity potential) and rotational (streamfunction) components of flow, horizontal wind and moisture flux anomalies are investigated.

There is strong coupling between the El Niño SST anomalies in the Pacific Ocean and changes in MSLP. Figure 5.3 shows that the El Niño SST conditions decrease MSLP over the central and eastern Pacific Ocean and increase MSLP over the western Pacific Ocean and the Maritime continent, which correspond with warm and cold SST anomalies, respectively. This high-low pressure gradient anomaly across the Pacific Ocean is a typical atmospheric response to El Niño as seen in previous studies (Tyson & Preston-Whyte, 2000; Reason & Jagadheesha, 2005; Ashok et al., 2007; Yuan et al., 2014). However, there is variation in the extent of the pressure gradient anomaly between the different El Niño SST conditions. As the size and intensity of the warm SST anomaly increases across the central and eastern Pacific, MSLP decreases, with EN4 showing the most significant decrease. Similarly, the increase in MSLP over the western Pacific Ocean is strongly associated with the intensity of the cold SST anomaly in the region. For example, EN2 shows the least significant change in the western Pacific Ocean which results from a lack of significant cold SST anomaly. Changes in MSLP over the Indian Ocean are mainly driven by ENSO teleconnections, with increased pressure across most of the region, despite the local SST anomalies. For example, EN4 is characteristic of a positive Indian Ocean Dipole (IOD) with widespread warm SST, however it has the most significant increase in MSLP, spreading across Asia and Africa as well. In contrast, EN1 has significant cold SST anomalies in the Indian Ocean, but has the least significant increase in MSLP. All of the El Niño SST conditions show decreased MSLP over the North Atlantic Ocean, most significant in the tropical western region which typically correspond with warm SSTs. The El Niño SST conditions also show a region of increased MSLP over the Atlantic Ocean, however the position varies between the different conditions. EN1 and EN2 show the positive anomaly over the South Atlantic Ocean, whereas the anomaly is focused over the tropical region in EN3 and EN4 (only EN2 and EN4 are significant). The majority of southern Africa shows an increase in MSLP during the El Niño SST conditions, although only

significant in EN4 and along the south western coast in EN3. In contrast, EN1 shows widespread decrease in MSLP over southern Africa, although the anomaly is not significant.

The El Niño SST conditions also show significant changes in the upper tropospheric divergent flow (velocity potential, Figure 5.4). All of the El Niño SST conditions show a significant upper tropospheric divergence anomaly (negative velocity potential) over the eastern South Pacific Ocean and South America. This negative anomaly extends over the North Atlantic Ocean in EN2, EN3 and EN4. The El Niño SST conditions also show a divergence anomaly over the central Pacific Ocean which coincides with deep convection from the warm SST anomaly, however, only EN4 is significant in this region. In contrast, there is a significant upper tropospheric convergence anomaly (positive velocity potential) over the western Pacific Ocean, including Australia and the Maritime continent, which coincides with the increased MSLP and cool SST anomaly. This upper tropospheric convergence-divergence anomaly pattern across the Pacific Ocean is a clear indication of a weakening or shift in the Walker Circulation, which is expected during El Niño (Tyson & Preston-Whyte, 2000; Reason & Jagadheesha, 2005; Ashok et al., 2007; Yuan et al., 2014). EN4 has the most significant velocity potential anomalies, indicating the most significant weakening of the Walker Circulation. EN2 and EN3 have similar velocity potential anomalies, although not as strong as EN4. In EN2, EN3 and EN4, the upper tropospheric convergence anomaly also extends over the Indian Ocean (significant in EN2 and EN4) and is still significant over southern Africa in EN4. This anomalous convergence over the Indian Ocean results in a north-eastward shift of the South Indian Ocean Convergence Zone (Cook, 2001) and tropical temperate trough systems (Tyson & Preston-Whyte, 2000), contributing to the dry conditions across southern Africa during El Niño. However, the upper tropospheric velocity potential anomalies of EN1 are notably different to the other El Niño SST conditions. EN1 has a significant divergence anomaly across the Indian Ocean and the eastern coast of Africa. It also shows a convergence anomaly in the eastern Pacific Ocean (90ºW – 160ºW), which is significant off the coast of North America, characteristic of a central Pacific El Niño (Wilson *et al*., 2014).

Figure 5.5 shows the eddy streamfunction (zonal mean removed) for each of the El Niño SST conditions which emphasizes the large-scale stationary wave response. Positive streamfunction values indicates clockwise rotation, whilst negative values indicate anticlockwise rotation, which

correspond to cyclonic (anticyclonic) and anticyclonic (cyclonic) rotation in the southern (northern) hemisphere, respectively. All of the El Niño SST conditions show a pair of anticyclonic anomalies in the upper troposphere over the central and eastern Pacific Ocean. This is characteristic of a Gill-Matsuno type response which is expected due to the warm SST anomalies in the tropical Pacific Ocean associated with El Niño (Cook, 2001; Wilson *et al*., 2014). This indicates a significant weakening of the cyclonic flow in the eastern Pacific Ocean and as such a weakening of the Walker Circulation. The strength of the anticyclonic anomaly and weakening of the Walker Circulation is proportional to the intensity of the ENSO SST anomaly associated with each El Niño condition, with EN4 showing the most significant anomaly. There is also a significant pair of cyclonic anomalies in the upper troposphere over the Indian Ocean and Asia, evident in all of the El Niño SST conditions. However, the size and position of these cyclonic anomalies varies between the conditions. EN1, EN3 and EN4 show the cyclonic anomaly positioned over the eastern Indian Ocean, whilst EN2 shows the anomaly over the western Indian Ocean and tropical region of Africa. EN2, EN3 and EN4 show that the pair of cyclonic anomalies also extend across Africa and the Atlantic Ocean. This results in anomalous cyclonic flow in the upper troposphere over southern Africa, weakening the anticyclonic flow seen over the region during austral summer. In contrast, EN1 significantly strengthens the anticyclonic flow in the upper troposphere over southern Africa.

The El Niño SST conditions are associated with significant changes in the global wind circulation. All of the El Niño SST conditions show a significant weakening of the Walker circulation. This is indicated by westerly anomalies in the lower troposphere and easterly anomalies in the upper troposphere across the tropical Pacific Ocean basin (Figure 5.6). This response is typical of El Niño and agrees with previous studies (Tyson & Preston-Whyte, 2000; Reason & Jagadheesha, 2005; Ashok et al., 2007; Yuan et al., 2014). However, the magnitude of this weakening is directly proportional to the strength of the warm SST anomaly in the Pacific Ocean, with EN1 showing the least and EN4 showing the most significant changes. In the upper troposphere, the easterly anomaly in the equatorial region lends itself to anticyclonic circulation across the Pacific Ocean in both hemispheres. This results in the significant strengthening of the subtropical jet stream as seen in EN3 and EN4. Over the tropical Indian Ocean, there is an easterly anomaly in the lower troposphere (most significant in EN1 and EN4), which is a result of diverging air over the Maritime

Continent from the descending limb of the Walker Circulation. This anomaly is strengthened in EN4 by the presence of the positive IOD. Over Africa, EN1 is associated with a significant upper tropospheric easterly anomaly over the equatorial region, which in turn strengthens the Tropical Easterly Jet (TEJ). In the lower troposphere, there aren't any significant changes to the circulation over southern Africa, however, there is a weak cyclonic anomaly over the Mozambique Channel. EN2 is associated with a significant easterly anomaly over the equatorial region at 850 hPa and a weak anticyclonic anomaly over the west coast of southern Africa, which is also seen at 200 hPa. There is also a notable anticyclonic anomaly over the south-western Indian Ocean, which extends over the eastern part of the continent. In the upper troposphere, EN3 and EN4 are associated with westerly anomalies across Africa and the Atlantic and Indian Oceans, although only significant in EN4. There are no clear circulation patterns associated with EN3 in the lower atmosphere, however, EN4 shows a weak anticyclonic anomaly over the Mozambique Channel.

There are variations in the moisture flux divergence over southern Africa associated with each El Niño condition. Figure 5.7 shows that the vertically integrated moisture flux for the El Niño SST conditions is characterized with lower tropospheric anticyclonic anomaly over southern Africa. This results in the typical dry conditions associated with El Niño, previously reported by studies (Tyson & Preston-Whyte, 2000; Ashok et al., 2007; Davis, 2011; Hoell et al., 2015; Yuan et al., 2014). However, the location and intensity of the anticyclonic moisture flux varies between the El Niño SST conditions, resulting in the variations seen in the drought patterns (Figure 5.1). EN1 and EN3 show the anticyclonic moisture flux anomaly over the central region, whereas EN2 shows stronger anticyclonic circulation in a more northerly position and EN4 shows an elongated circulation in a more south easterly position. These anticyclonic moisture flux anomalies are associated with divergence (Figure 5.7), resulting in dry conditions in their respective areas. EN1 shows cyclonic moisture flux anomaly over the Mozambique Channel, whilst EN2 shows anticyclonic moisture flux anomaly in that region. The two anticyclones in EN2 cause significant divergence over Tanzania, resulting in severe drought conditions (seen in Figure 5.1). They also cause an increase in convergence in the central region across Zambia, Botswana and Zimbabwe, resulting in widespread wet conditions seen in this region during EN2. There is a progressive increase in the westerly moisture flux anomaly in the southern region throughout the El Niño SST conditions, with EN1 showing minimal anomaly and EN4 showing the strongest westerly

anomaly. This is associated with a progressive increase in the extent of divergence seen across the southern part of the region, as well as a gradual increase in the intensity and extent of drought in the region (seen in Figure 5.1). Unlike the other El Niño SST conditions, EN4 shows onshore moisture flux from the tropical Atlantic Ocean. This converges with the onshore flux from the Mozambique channel, resulting in notable convergence and wet conditions over Angola and the Congo basin.

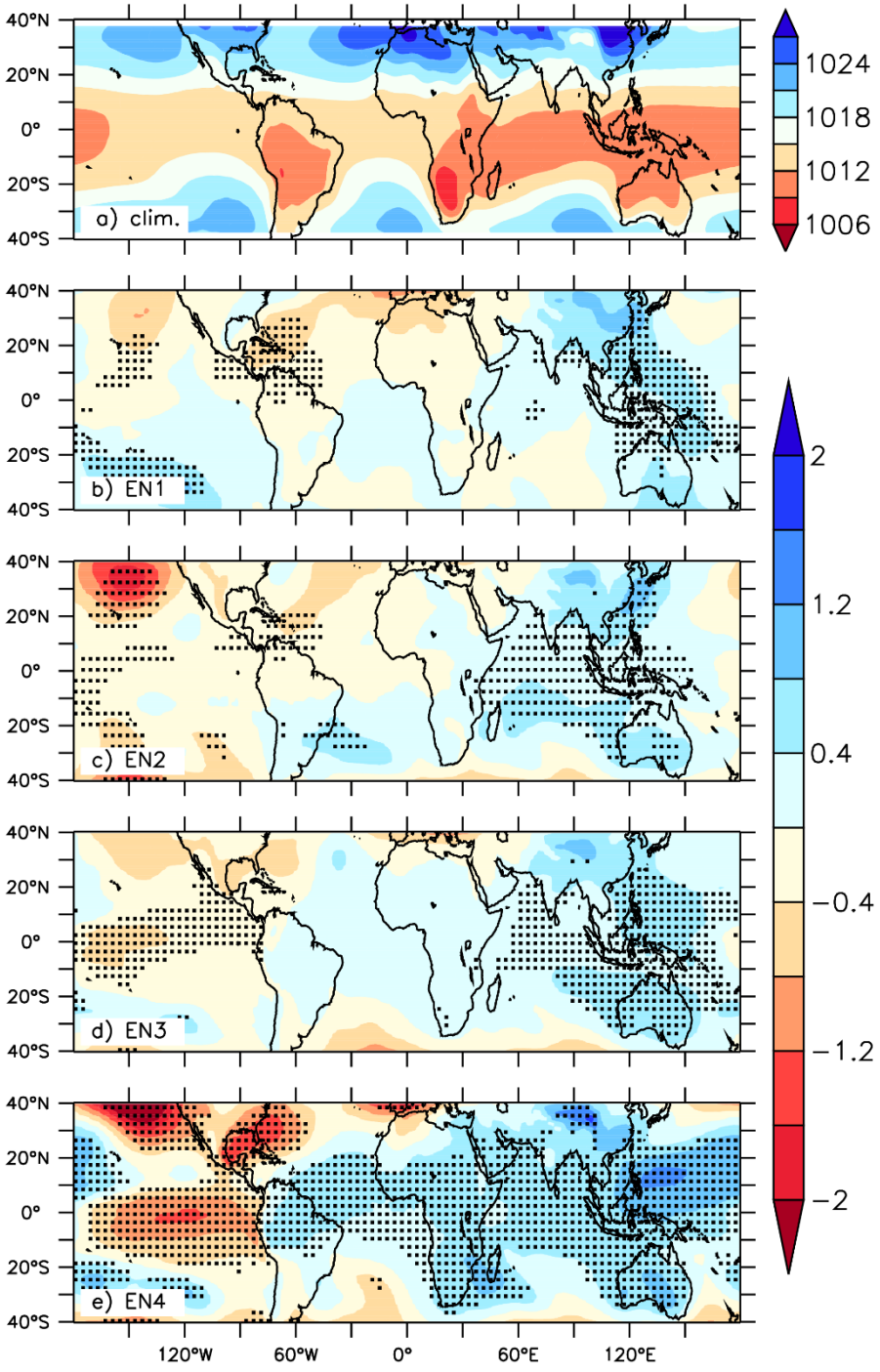

Figure 5.3 Mean sea level pressure (MSLP, hPa) for DJF climatology averaged over the period 1979 – 2008 and composite anomalies for each of the El Niño SST conditions. Shading indicates MSLP anomalies significant at the 99th percentile

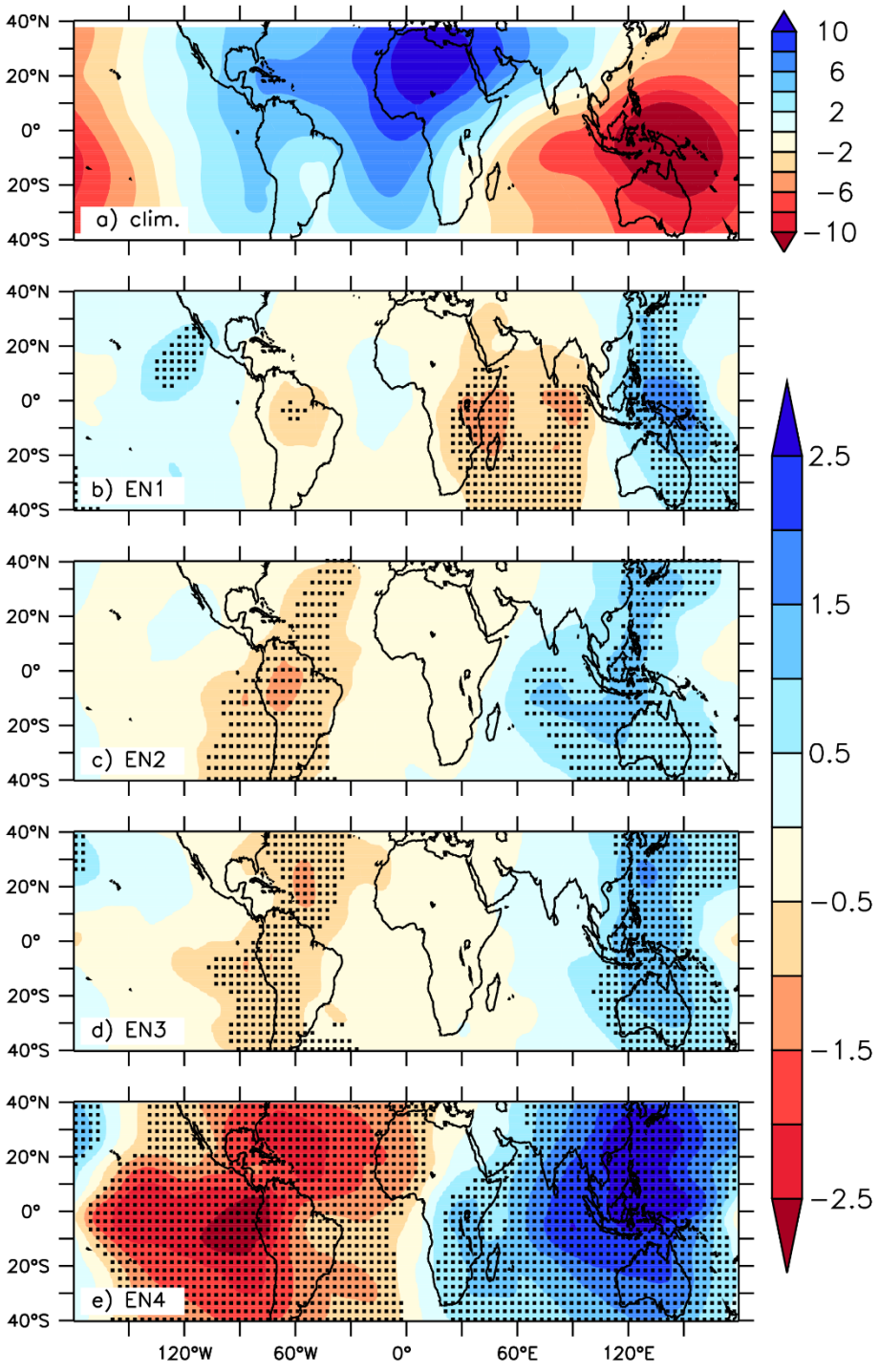

Figure 5.4 200 hPa velocity potential (x10^6 m^2/s) for DJF climatology averaged over the period 1979 – 2008 and composite anomalies for each of the El Niño SST conditions. Positive values indicate convergent flow and negative values indicate divergent flow. Shading indicates DJF velocity potential anomalies significant at the 99th percentile

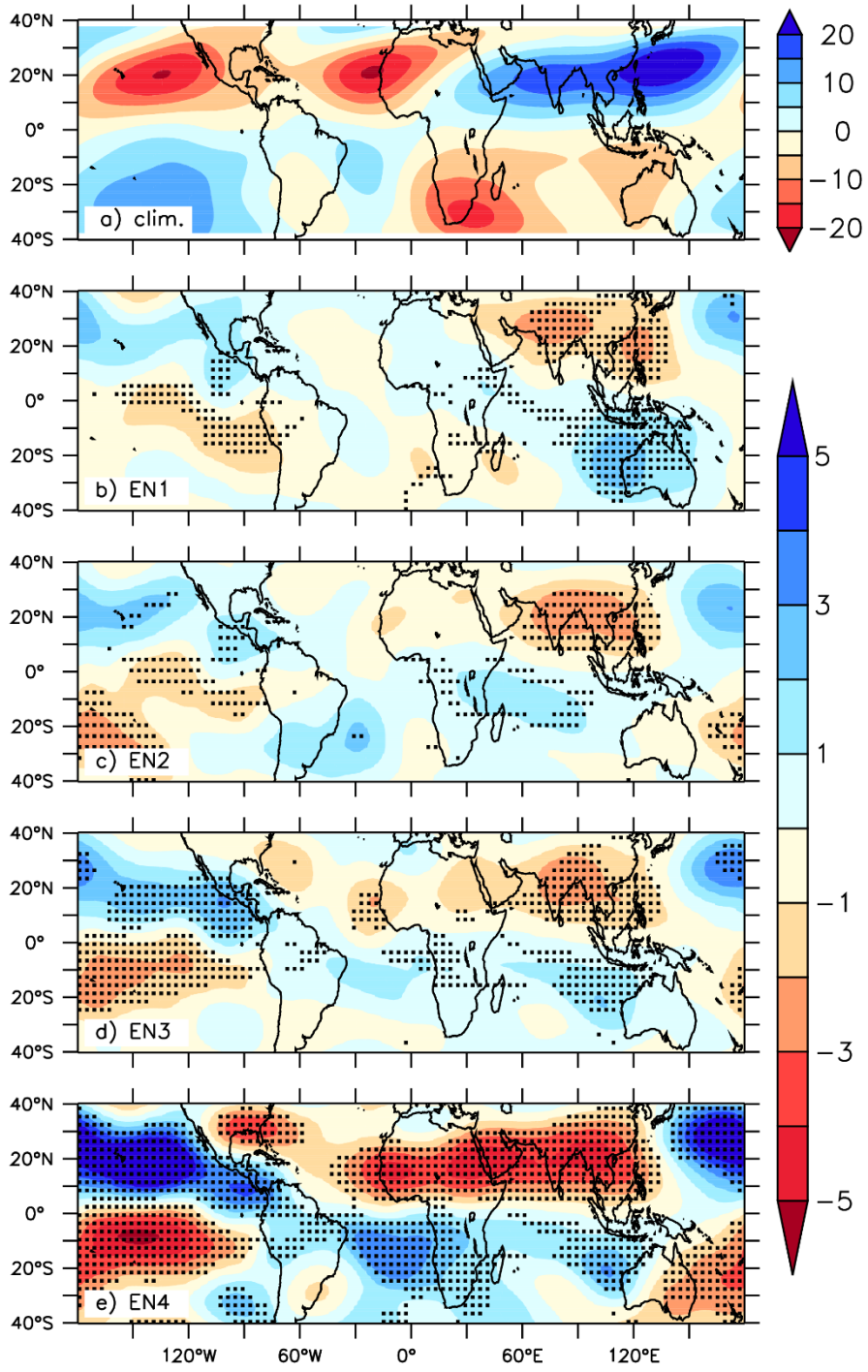

Figure 5.5 200 hPa eddy stream function (x10^6 m^2/s) for DJF climatology averaged over the period 1979 – 2008 and composite anomalies for each of the El Niño SST conditions. Positive values indicate clockwise rotation and negative values indicate anticlockwise rotation. Shading indicates DJF eddy stream function anomalies significant at the 99th percentile

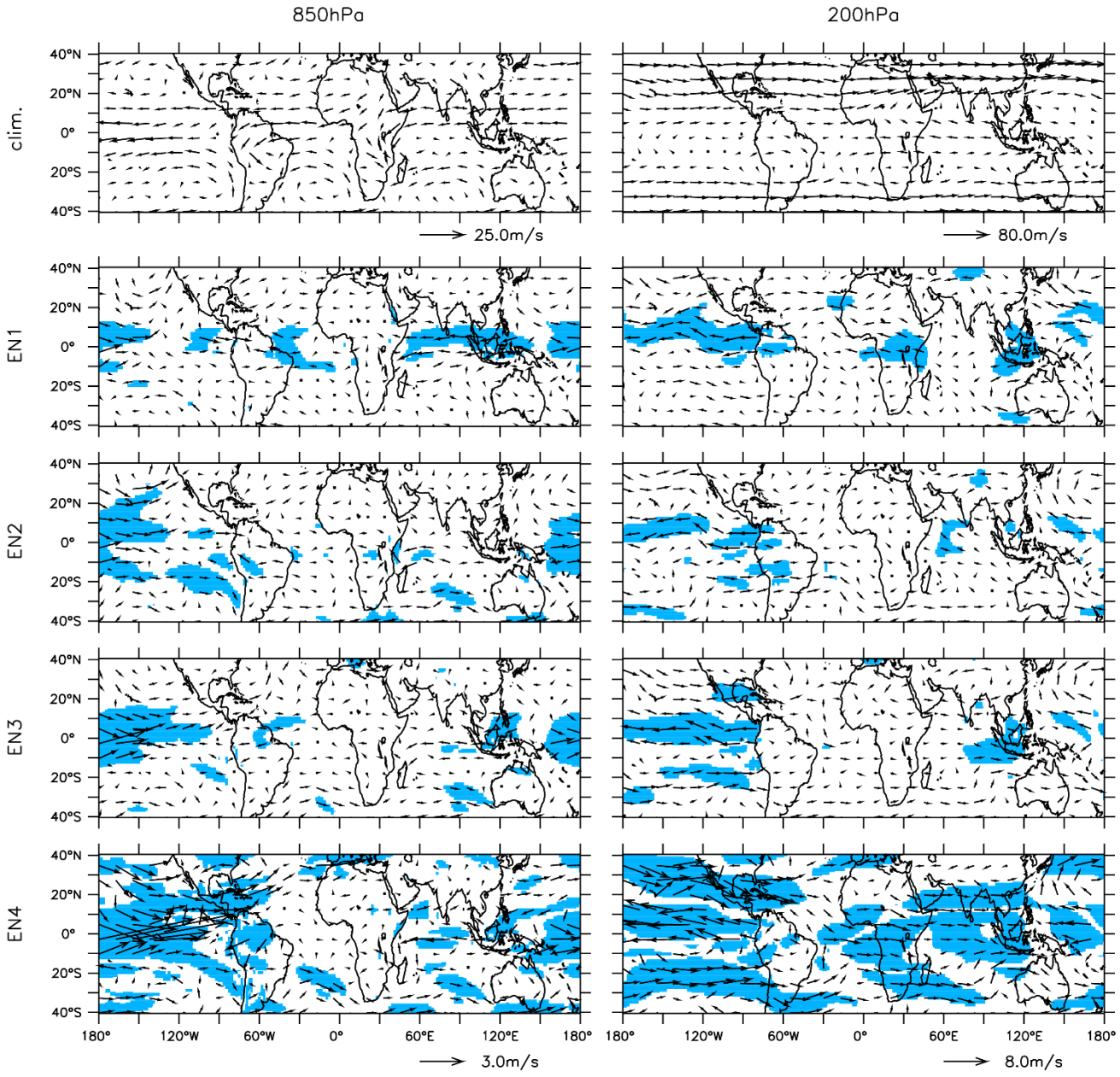

Figure 5.6 850 hPa and 200 hPa wind vectors (m/s) for DJF climatology averaged over the period 1979 – 2008 and composite wind vector anomalies for each of the El Niño SST conditions. Shading indicates DJF wind speed anomalies significant at the 99th percentile

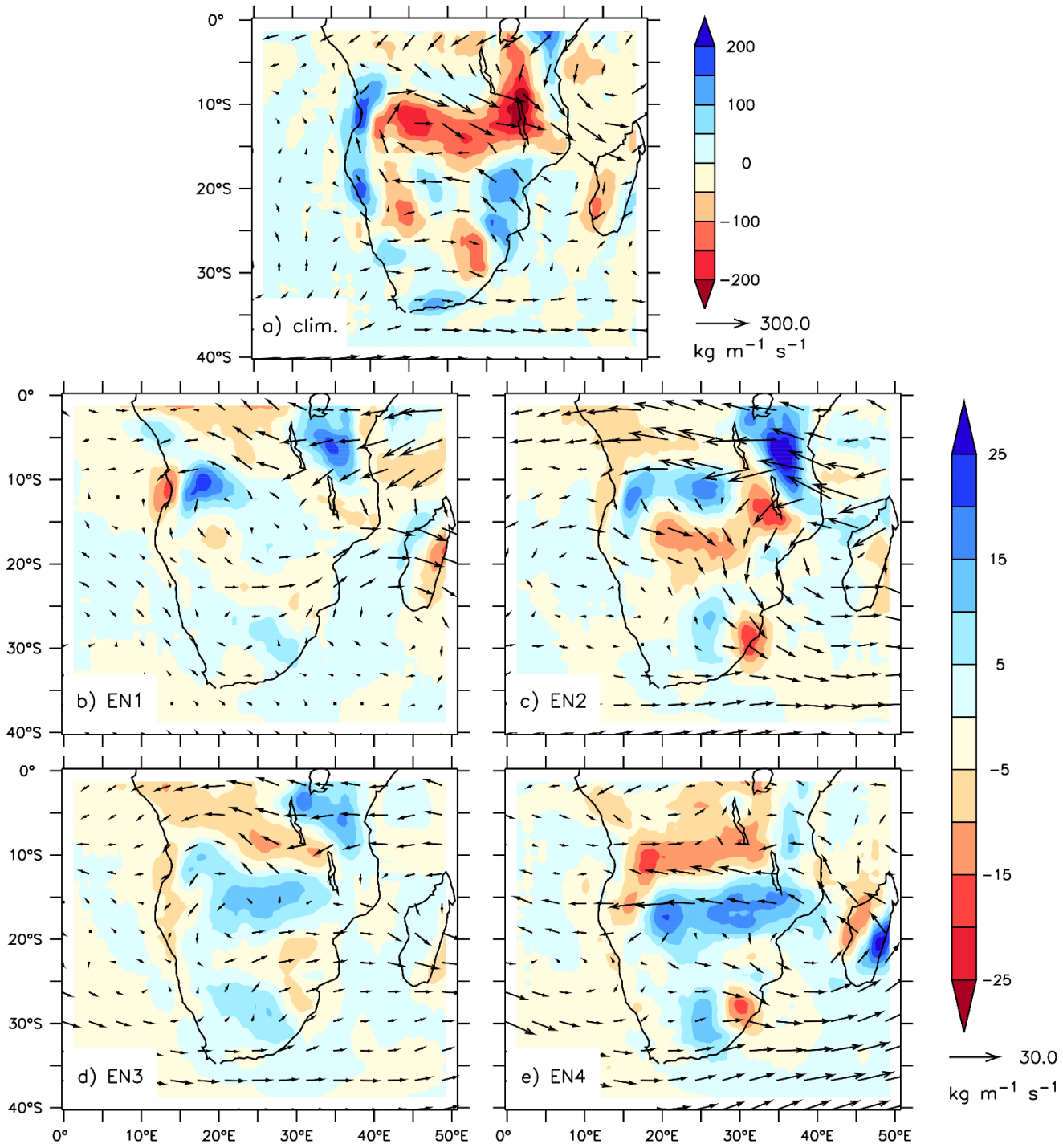

Figure 5.7 Vertically integrated moisture flux divergence (x10^{-6} kg m^{-2} s^{-1}) and vertically integrated moisture flux vectors (kg m^{-2} s^{-1}) for a) DJF climatology averaged over the period 1979 – 2008 and b-e) composite anomalies for each of the El Niño SST conditions

5.2 La Niña

5.2.1 Drought associated with La Niña SST conditions

The La Niña results show a distinct dipole pattern in the SPEI drought, although there is variation in the spatial pattern and intensity between the La Niña SST conditions (Figure 5.8). Across all the La Niña SST conditions there is a significant positive anomaly (99th percentile) in the central/southern region of the subcontinent with a negative anomaly stretching across the tropical region (~ 5-10˚S). The positive anomaly (SPEI > 0.5) is focused over Botswana, Zimbabwe and north-eastern South Africa with LN1 showing the strongest (SPEI > 1) and most widespread signal including the rest of South Africa (Figure 5.8 a). The other La Niña SST conditions all show a similar positive anomaly, however, LN3 (Figure 5.8 c) also shows significant positive SPEI along the southern coast. LN1 shows the strongest negative anomaly in the tropical region with SPEI drought greater than -1.5 in parts of Angola. LN2 (Figure 5.8 b) also shows a significant negative anomaly in the tropical region, although not as widespread in the central areas. On the other hand, LN3 and LN4 (Figure 5.8 c and d) show a weaker (SPEI < -0.5), but still significant negative anomaly in the tropical region. However, the negative anomaly spreads more over the Congo basin and down the western coast into South Africa. Overall, LN1 shows the strongest dipole pattern whilst LN4 shows the weakest signal. The general dipole pattern seen in Figure 5.8 corresponds with the literature (Tyson & Preston-Whyte, 2000; Meque & Abiodun, 2013; Hoell *et al*., 2015), which typically associates La Niña phases with wet conditions across most of the sub-region and dry conditions in the tropical region. There are only a few differences seen between SPEI and SPI, which are mostly focused in the semi-arid area, over Namibia and western South Africa. The influence of evapotranspiration has two different effects on SPEI, depending on the La Niña condition. In LN1 and LN2, SPEI shows a reduced negative anomaly and increased coverage of the wet anomaly in the semi-arid area (Figure 5.8 a and b) compared to SPI (Figure 5.8 e and f). On the other hand, LN3 and LN4 show an increased negative anomaly over Namibia in the SPEI results (Figure 5.8 c and d). This emphasizes the importance of considering evapotranspiration when analysing drought in the semi-arid region as mentioned by Meque & Abiodun (2013).

There is variation in the uncertainty of the drought signal across the different areas as shown in the ensemble spread of the La Niña SST conditions (Figure 2.9). In the tropical area, LN1 and LN2 show a high probability of drought with at least 75% of the ensembles giving a negative SPEI

value. LN2 indicates the most severe drought where approximately 50% of the ensembles have an SPEI value less than -1. This agrees with studies (Nicholson & Selato, 2000; Reason & Jagadheesha, 2005) which show that dry conditions typically develop over the tropical area during La Niña phases. However, this does not fully agree with the observed CRU events which generally show higher SPEI values, mostly within the upper two quartiles of the ensemble spread. On the other hand, LN3 and LN4 remain uncertain in their signal, as the ensemble SPEI values range between 1 and -1. There is a strong probability of wet conditions in the subtropical region during the La Niña phase, with more than 75% of the ensembles showing positive SPEI anomalies across all La Niña SST conditions. However, it is hard to distinguish this signal from the precipitation bias which SPEEDY simulates in this area (as seen in Figure 4.2). Although, this might not be the case as the ensemble spread has very good agreement with the observed CRU events. The SPEI results in the semi-arid area have the biggest ensemble spread and are uncertain. LN1 shows the most definite signal of positive SPEI, although it is less than 75% of the ensembles. The semi-arid area also shows the least agreement with CRU observation, generally producing SPEI values lower than observed. The results in the subtropical and semi-arid areas become more uncertain when only considering precipitation, as in SPI (Figure 5.9 b). This is seen by an increase in the inter-quartile range, particularly in LN1 and LN4. However, in the tropical area LN1 shows a more robust signal in the SPI ensemble spread. This is expected in the tropical area as SPEI is strongly correlated with precipitation, whilst the effect of temperature is low (Meque & Abiodun, 2013).

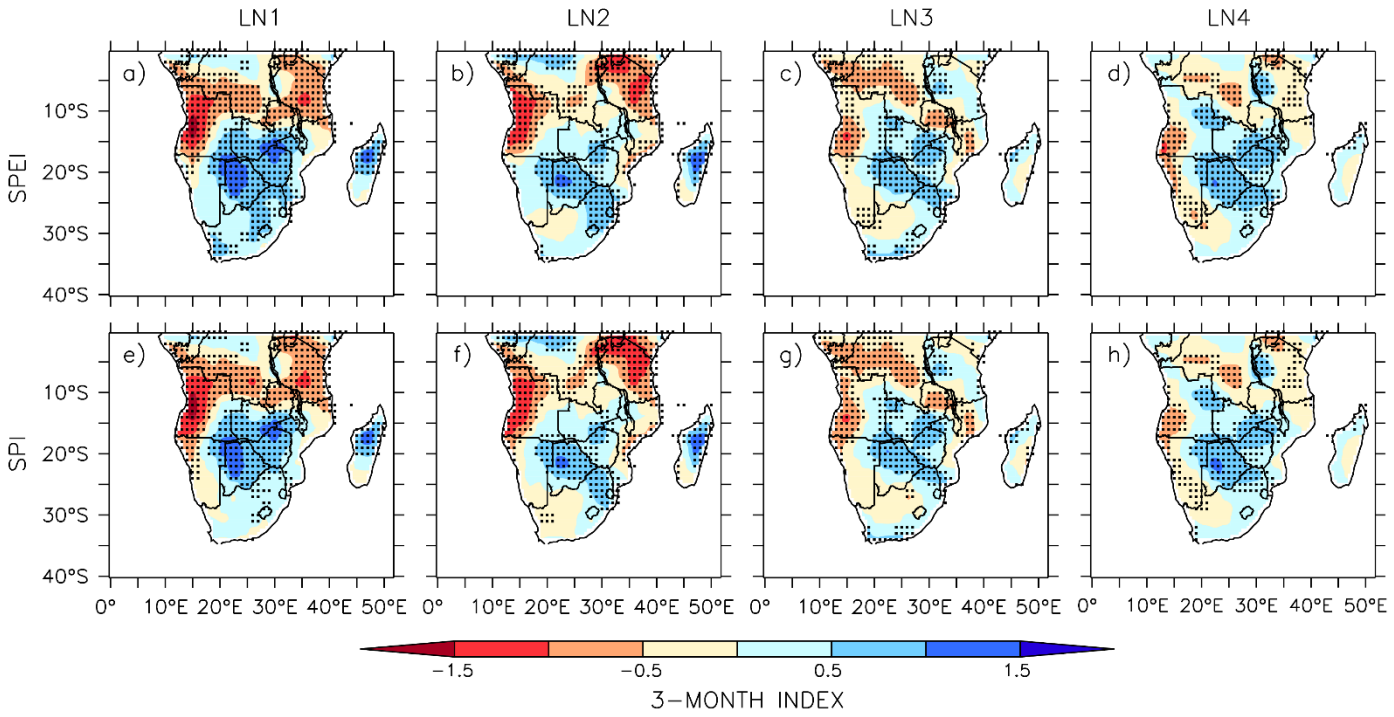

Figure 5.8 Same as figure 5.1, but for the La Niña SST conditions

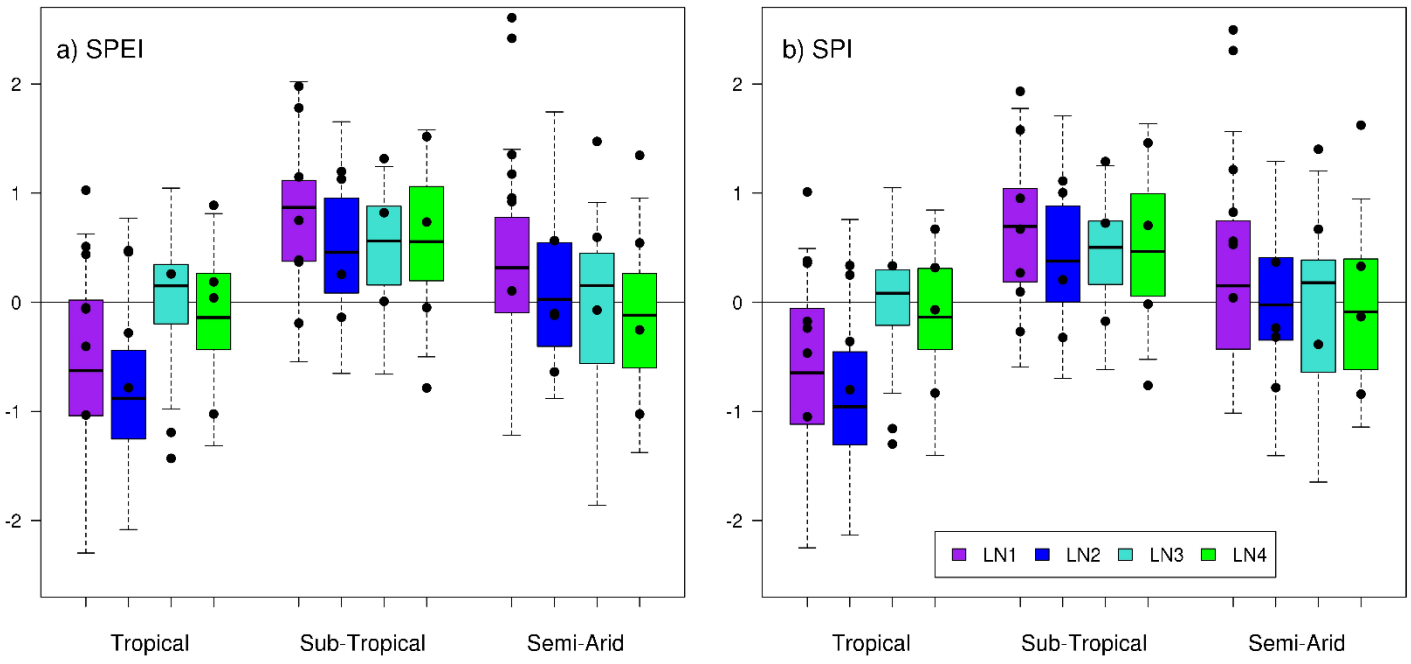

Figure 5.9 Same as figure 5.2, but for the La Niña SST conditions

5.2.2 Atmospheric Dynamics of La Niña SST conditions

There are also significant changes in global MSLP associated with the La Niña SST conditions (Figure 5.10). The central and eastern Pacific Ocean is dominated by a significant increase in MSLP, which is linked to the intensity of the cold SST anomaly in the region. Similarly, there is a decrease in MSLP over the western Pacific Ocean, which is strongly associated with warm SST anomalies in the region. This MSLP anomaly pattern strengthens the pressure gradient across the Pacific Ocean, thereby strengthening the Walker Circulation, which is expected during La Niña (Tyson & Preston-Whyte, 2000; Reason & Jagadheesha, 2005; Ashok et al., 2007; Yuan et al., 2014). LN1 and LN3 show the most significant strengthening of the Walker Circulation, whilst LN2 shows the least change in MSLP across the Pacific Ocean. The negative anomaly over the western Pacific Ocean also extends across the Indian Ocean and Africa during the La Niña SST conditions, and as far as the Atlantic Ocean in LN1, LN3 and LN4. The SST anomalies in the Indian Ocean and Atlantic Ocean have a moderating effect on the ENSO teleconnections. For example, LN3 shows the most significant decrease in MSLP in both ocean basins, as a result of the local warm SST anomalies. In contrast, LN2 shows an increase in MSLP across Asia and the North Indian Ocean (significant), as well as over the South Atlantic Ocean (not significant). The majority of southern Africa shows a decrease in MSLP during the La Niña SST conditions, which is significant in LN1, LN3 and LN4.

The La Niña SST conditions show significant changes in the upper tropospheric divergent flow (velocity potential, Figure 5.11). All of the La Niña SST conditions show a significant upper tropospheric convergence anomaly (positive velocity potential) over the central and eastern Pacific Ocean, with LN2 showing the weakest anomaly and LN3 showing the strongest anomaly. This anomaly strengthens upper tropospheric convergence due to increased subsidence accompanying the underlying cold SST anomalies. There is also a significant upper tropospheric divergence anomaly over the western Pacific Ocean, Australia and the Maritime continent, which corresponds with warm SST anomalies in the region, except that LN2 shows significant divergence over Australia. This upper tropospheric divergence-convergence anomaly across the Pacific Ocean strengthens the austral summer velocity potential pattern and further indicates a strengthening of the Walker Circulation. LN3 shows the most significant strengthening of the Walker Circulation. The convergence anomaly over the eastern Pacific extends across North America and the North

Atlantic Ocean and is strongest in LN3. LN3 and LN4 also show the convergence anomaly over South America which is significant along the western coast. In contrast, LN1 and LN2 show an upper tropospheric divergence anomaly centred over Brazil. There is a significant divergence anomaly extending across the Indian Ocean, Asia and Africa during LN3 and LN4, which are strengthened by the warm SST anomalies in the region. LN1 also shows significant divergence anomalies over the Indian Ocean, but not in the central region due to cold SST anomalies. LN2 also has cold SST anomalies across the Indian Ocean, resulting in minimal changes to velocity potential, except for a small area of significant divergence in the eastern region. Generally, southern Africa experiences anomalous divergent flow in the upper troposphere, which is significant in LN1, LN3 and LN4, with LN3 showing the strongest anomaly. This strengthens the South Indian Ocean Convergence Zone and encourages the formation of tropical temperate troughs during La Niña (Tyson & Preston-Whyte, 2000).

There are significant anomalies in the upper tropospheric rotational flow (eddy streamfunction) of the La Niña SST conditions (Figure 5.12). There is a significant strengthening of the cyclonic flow in the upper troposphere over the central and eastern Pacific Ocean, shown by a pair of cyclonic anomalies, which are associated with the intensity of the cold SST anomaly in the region. LN3 has the strongest anomaly and the cyclonic flow extends as far as the western Pacific Ocean in LN1 and LN3. On the other hand, LN2 has the weakest anomaly and is limited to the eastern Pacific Ocean. There is a pair of significant upper tropospheric anticyclonic anomalies extending across Africa, the Atlantic Ocean and North and South America. LN3 shows the strongest anticyclonic anomalies, whilst LN2 shows the weakest anomalies which are primarily focused over Africa. Generally, the Indian Ocean also experiences anticyclonic anomalies, however they are not as strong as those over the Atlantic Ocean, particularly in LN1, LN3 and LN4. LN1 also shows a significant upper tropospheric cyclonic anomaly over the South Indian Ocean, which is also seen in the other La Niña SST conditions, although not significant. Southern Africa is generally characterized by a significant upper tropospheric anticyclonic anomaly over the tropical region, which is most significant in LN3. However, the southern tip of Africa shows an upper tropospheric cyclonic anomaly in LN1, LN2 and LN4, although not significant. This indicates a northward shift of the anticyclonic flow typically seen over southern Africa in austral summer (Figure 5.5).

The La Niña SST conditions are also associated with significant changes in the global wind circulation. Most notably is the strengthening of the Walker circulation seen in all of the La Niña SST conditions. This is generally shown by easterly anomalies in the lower troposphere and westerly anomalies in the upper troposphere across the tropical Pacific Ocean basin (Figure 5.13). This is a typical atmospheric response to La Niña as shown by previous studies (Tyson & Preston-Whyte, 2000; Reason & Jagadheesha, 2005; Ashok et al., 2007; Yuan et al., 2014), however, the intensity of this anomaly varies between the conditions. LN1 and LN3 show the most significant strengthening of the Walker Circulation, whilst LN2 shows the least change in the lower troposphere and LN4 shows the least change in the upper troposphere over the Pacific Ocean. LN1, LN2 and LN3 also show significant westerly anomalies over the eastern Pacific Ocean and/or South America at 850 hPa as a result of diverging air caused by the descending limb of the Walker Circulation over the central Pacific Ocean. In contrast to El Niño, the La Niña SST conditions have a more significant influence on the upper tropospheric wind circulation, particularly over Africa and the Indian and Atlantic Oceans. This robust modification of the Walker Circulation explains the stronger SPEI signal over southern Africa during the La Niña SST conditions, compared to El Niño. All of the La Niña SST conditions show significant easterly anomalies globally in the upper troposphere, which result in a weakening of the subtropical westerly jet stream and strengthening of the TEJ. In the lower troposphere, there are cyclonic circulation anomalies over the Indian Ocean in both hemispheres. This results in a significant westerly anomaly along the equator and easterly anomalies in the subtropical regions, although more significant in the northern part of the ocean basin. This circulation anomaly is strongest in LN3, due to the presence of the negative IOD, and weakest in LN4. The tropical Atlantic Ocean shows lower tropospheric westerly anomalies in LN3 and LN4, although only significant in LN3, and easterly anomalies in LN2. Southern Africa is generally characterized by cyclonic circulation in the lower troposphere for all of the La Niña SST conditions, resulting in significant westerly flow over the tropical part of the region. In the upper troposphere, LN1 and LN2 are dominated by an easterly anomaly across southern Africa, whereas LN3 and LN4 show minimal circulation change over the southern region.

Each La Niña condition shows variations in the integrated moisture flux divergence over southern Africa, resulting in notable differences in the drought patterns. The La Niña SST conditions are generally characterized by lower tropospheric cyclonic moisture flux anomaly over the central part

of the region (Figure 5.14). This results in significant convergence and increased precipitation in the region, including Zambia, Zimbabwe and Botswana. This agrees with previous studies, which show that La Niña is generally associated with pluvial conditions (Tyson & Preston-Whyte, 2000; Ashok et al., 2007; Davis, 2011; Yuan et al., 2014; Hoell et al., 2015). The position of the convergence associated with the cyclonic anomaly is indicative of a southward shift of the ITCZ during La Niña. There are no notable changes in the size or position of the cyclonic anomaly between the La Niña SST conditions. However, there is variation in its intensity with LN1 showing the strongest and LN2 showing the weakest anomaly. This cyclonic anomaly is collocated with significant divergence to the north which varies with the position and intensity of the onshore moisture flux from the tropical Atlantic Ocean. LN3 and LN4 show significant onshore flux from the Atlantic Ocean throughout the tropical region (0º - 16ºS), with LN3 showing the strongest flux. This results in a divergence anomaly and drought conditions over the central and western equatorial region (Congo basin) and increased convergence over the eastern equatorial region (Tanzania). On the other hand, LN1 and LN2 show a weaker onshore moisture flux from the Atlantic Ocean, which is not as prevalent in the equatorial region. This results in divergent anticyclonic moisture flux and significant drought primarily over Angola, as well as divergence across the southern tropical region and Tanzania. This agrees with previous studies (e.g. Nicholson & Kim, 1997) that emphasize the influence of the Atlantic Ocean on southern Africa climate during the La Niña SST conditions, whilst the El Niño SST conditions are more strongly influenced by the Indian Ocean. All of the La Niña SST conditions show divergence along the western coast; however, only LN3 and LN4 result in significant drought in this region (seen in Figure 5.8). This is a result of the low moisture flux from the southern Indian Ocean, compared to the strong onshore flux during LN1 and LN2 which inhibits significant drought. LN3 also shows cyclonic moisture flux anomaly over the Mozambique Channel, resulting in significant wet conditions along the southern coast (Figure 5.8).

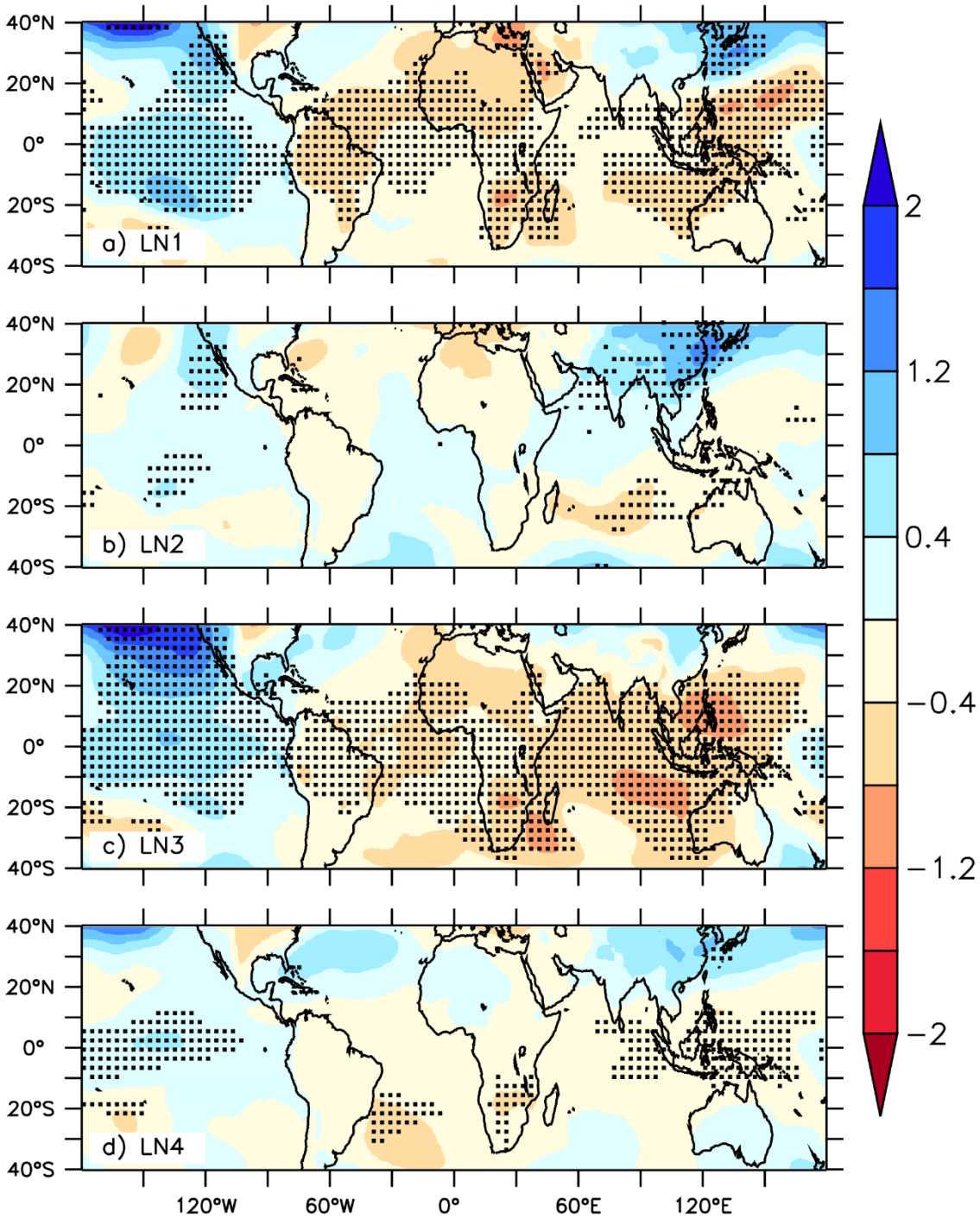

Figure 5.10 Same as figure 5.3, but for the La Niña SST conditions

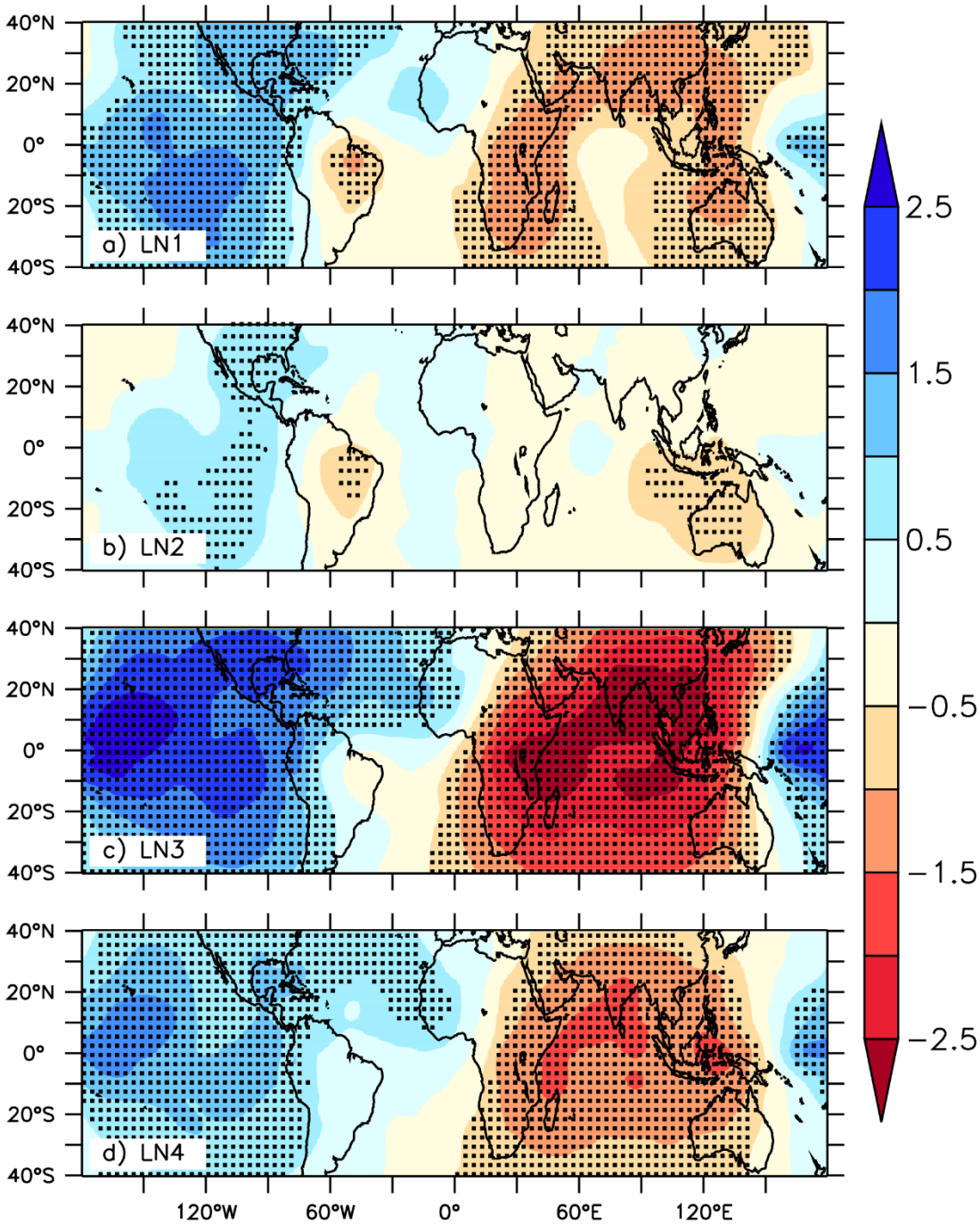

Figure 5.11 Same as figure 5.4, but for the La Niña SST conditions

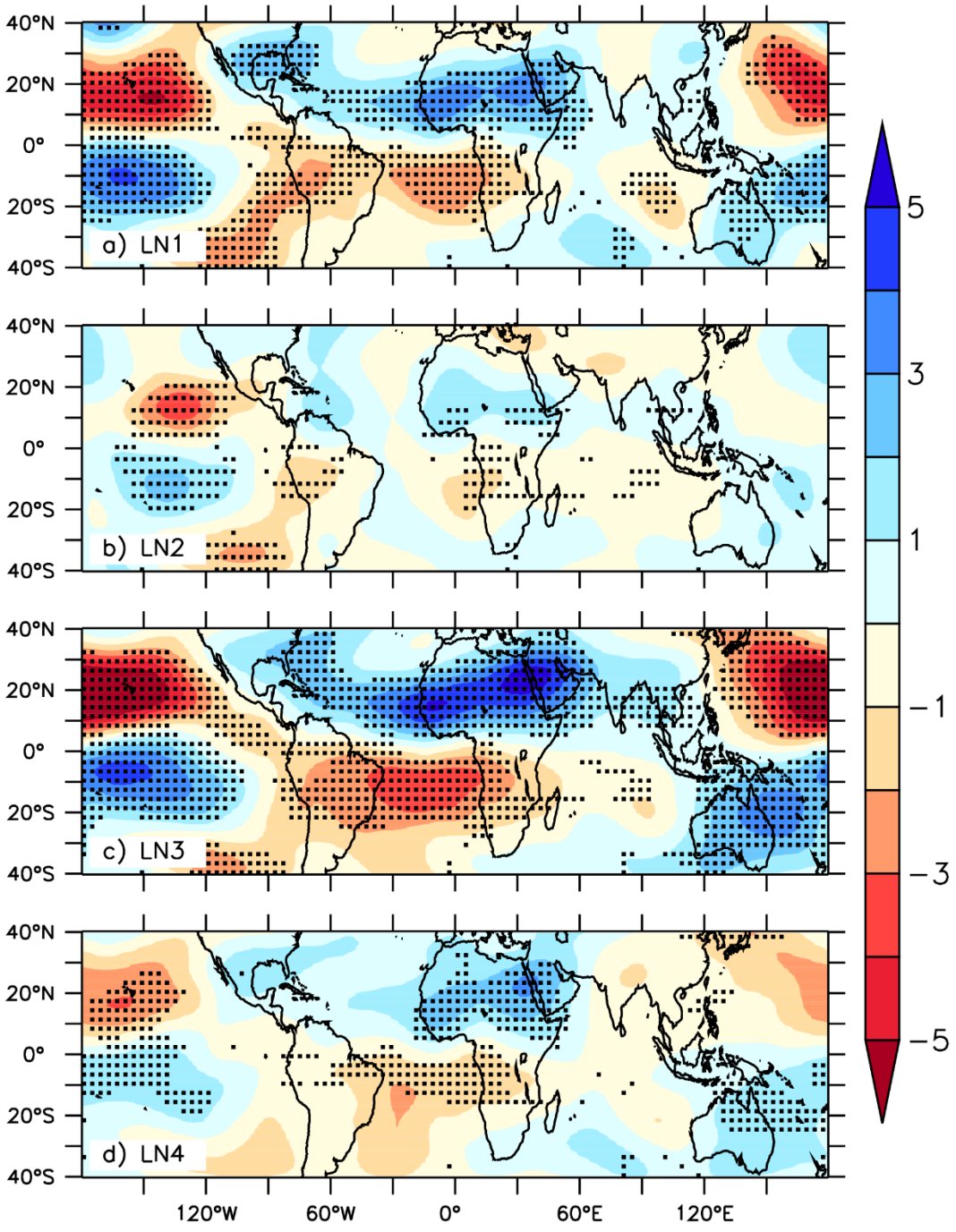

Figure 5.12 Same as figure 5.5, but for the La Niña SST conditions

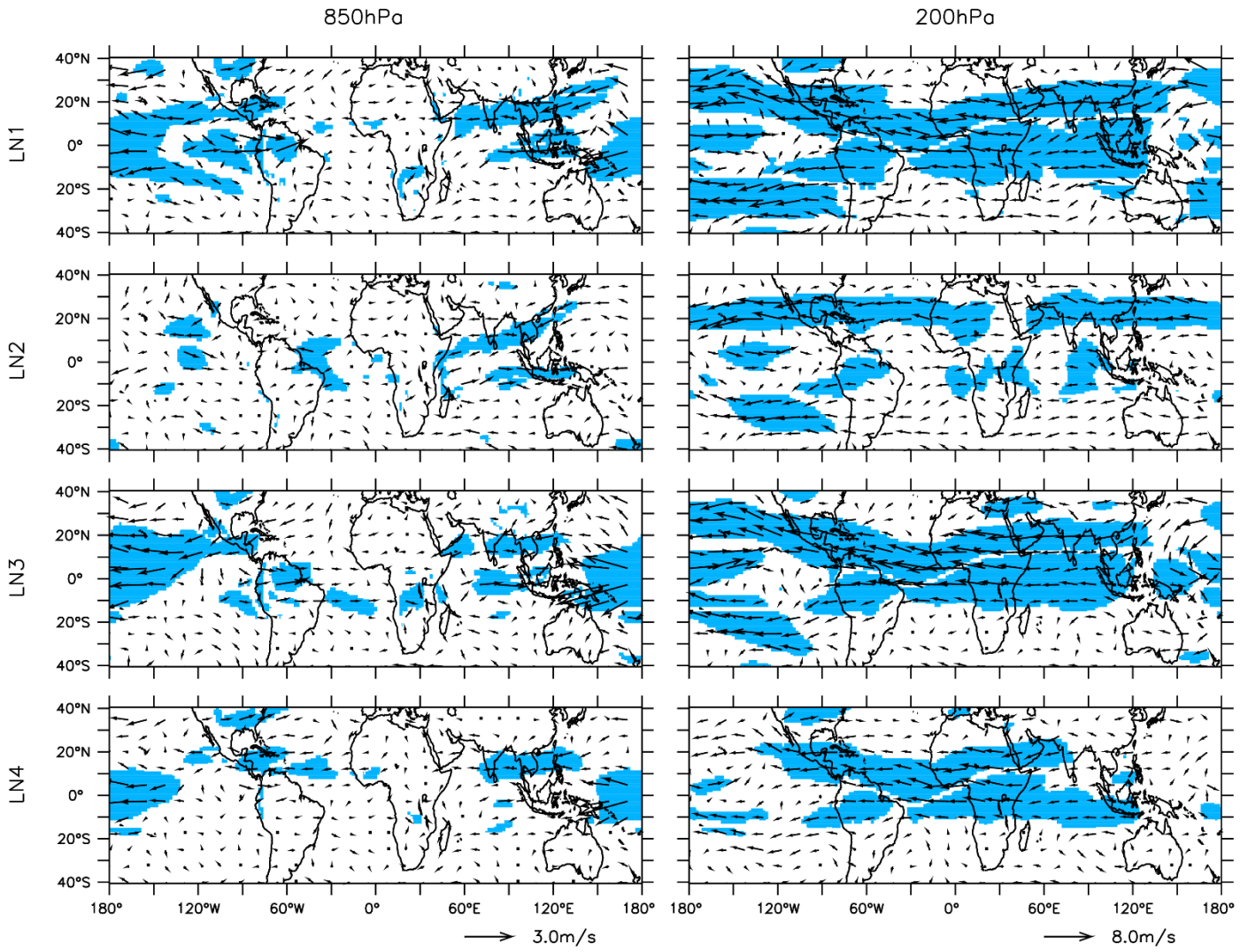

Figure 5.13 Same as figure 5.6, but for the La Niña SST conditions

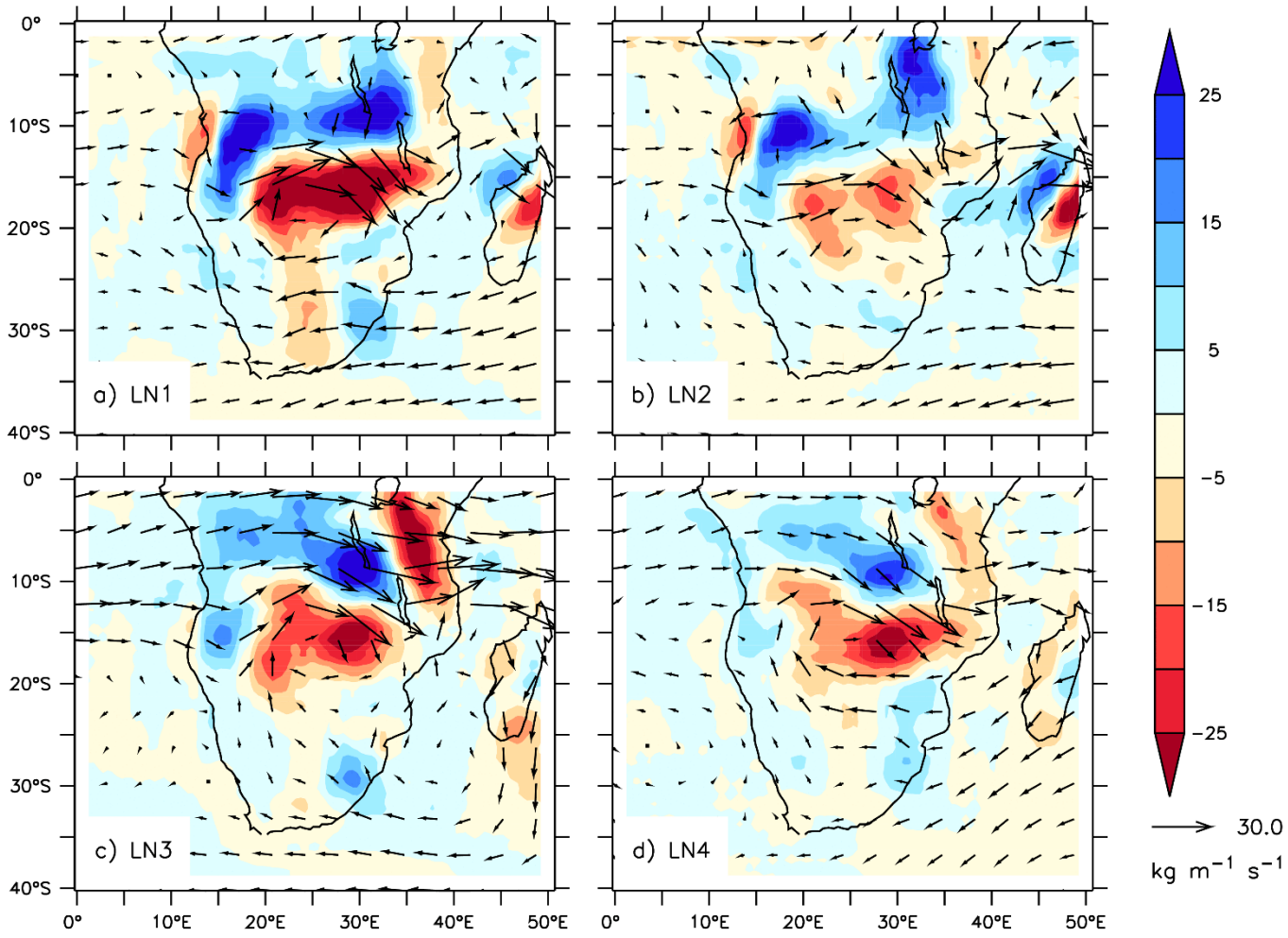

Figure 5.14 Same as figure 5.7, but for the La Niña SST conditions

Chapter 6: Conclusion

Chapter 6 provides a brief summary of this study as well as the key findings. Limitations and recommendations are also discussed.

In an effort to have a better understanding of the nonlinear impacts of ENSO on southern Africa climate, this study has investigated the relationship between southern Africa drought and eight ENSO SST patterns. We analyzed multi-forcing ensemble simulations from SPEEDY, an AGCM of intermediate complexity from the ICTP. SPEEDY simulations were forced with SST from each of the eight ENSO patterns previously identified by Johnson (2013). The capability of SPEEDY in reproducing southern Africa summer climate was evaluated by comparing the historical simulations (1979-2008) with CRU observation. The influence of each ENSO pattern on southern Africa drought was then explored in terms of the simulated drought indices (SPEI and SPI) and associated atmospheric dynamics.

Results of the study can be summarized as follows:

- SPEEDY generally captures characteristics of summer climate (DJF) over southern Africa well, albeit with warm and wet biases across the region. However, in most cases, these results are comparable with those from more complex atmospheric models.
- The SPEEDY simulation without the dynamic vegetation scheme tends to perform better than SPEEDY with dynamic vegetation in most instances, especially in the tropical and subtropical areas.
- The El Niño (La Niña) SST conditions typically result in negative (positive) SPEI and dry (wet) conditions over parts of southern Africa. However, the robustness of the SPEI signal varies across the different areas.
- The drought patterns are primarily driven by the weakening (strengthening) of the Walker circulation associated with the strength of the El Niño (La Niña) SST anomaly in the Pacific Ocean. However, variations in the Indian Ocean and Atlantic Ocean have a strong

moderating effect which alters the circulation, thereby influencing the spatial pattern and intensity of drought over the region.

- The El Niño SST conditions feature different characteristics of anticyclonic moisture flux over southern Africa which induce drought in different regions. EN1 and EN2 produce drought primarily in the tropical region whilst EN3 and EN4 show drought in the southwestern region.
- The La Niña SST conditions show a distinct dipole pattern in the drought, with significant wet conditions over the subtropical region driven by cyclonic moisture flux anomaly. Differences in the SPEI drought occur due to variations in the onshore flux from the southern Indian Ocean and tropical Atlantic Ocean, with LN1 and LN2 producing drought in the northern part, whilst LN3 and LN4 show drought along the western coast.

This study shows that accounting for the differences in ENSO patterns may improve drought predictions in southern Africa, however, these results have some limitations. Most notable is the warm and wet bias which SPEEDY produces over parts of southern Africa. This creates uncertainty in the results, particularly in areas (such as the subtropical region) where dry conditions are expected during El Niño phases, but SPEEDY simulates wet conditions. As seen in the model evaluation, climate models with higher resolution and complexity do produce more realistic simulations of the southern Africa climate, particularly precipitation, although they do also show some biases. Therefore, in order to improve these results, future research should consider using a more complex climate model with higher resolution, provided that such a model is accessible. Nevertheless, the flexibility and computational efficiency of SPEEDY was appropriate for this study and enabled multi-ensemble analysis of the relationship between southern Africa drought and different patterns of ENSO.

References

Abiodun, B.J., Makhanya, N., Petja, B., Abatan, A.A. and Oguntunde, P.G., 2018. Future projection of droughts over major river basins in Southern Africa at specific global warming levels. *Theoretical and Applied Climatology*, pp.1-15.

Angélil, O., Stone, D., Wehner, M., Paciorek, C.J., Krishnan, H. and Collins, W. 2017. An independent assessment of anthropogenic attribution statements for recent extreme temperature and rainfall events. *Journal of Climate*, *30*(1), pp.5-16.

Anyamba, A., Small, J. L., Britch, S. C., Tucker, C. J., Pak, E. W., Reynolds, C. A., Crutchfield, J., & Linthicum, K. J. 2014. Recent weather extremes and impacts on agricultural production and vector- borne disease outbreak patterns. *PloS one*, *9*(3), e92538.

Ash, K.D. and Matyas, C.J., 2012. The influences of ENSO and the subtropical Indian Ocean Dipole on tropical cyclone trajectories in the southwestern Indian Ocean. *International Journal of Climatology*, *32*(1), pp.41-56.

Ashok, K., Behera, S. K., Rao, S. A., Weng, H., & Yamagata, T. 2007. El Niño Modoki and its possible teleconnection. *Journal of Geophysical Research: Oceans (1978–2012)*, *112*(C11).

Bahaga, T.K., Mengistu Tsidu, G., Kucharski, F. and Diro, G.T., 2015. Potential predictability of the sea-surface temperature forced equatorial East African short rains interannual variability in the 20th century. *Quarterly Journal of the Royal Meteorological Society*, *141*(686), pp.16-26.

Beguería, S. and Vicente-Serrano, S.M., 2013. SPEI: calculation of the standardised precipitation-evapotranspiration index. *R package version*, *1*.

Beguería, S., Vicente-Serrano, S.M., Reig, F. and Latorre, B., 2014. Standardized precipitation evapotranspiration index (SPEI) revisited: parameter fitting, evapotranspiration models, tools, datasets and drought monitoring. *International Journal of Climatology*, *34*(10), pp.3001-3023.

Behera, S.K. and Yamagata, T., 2001. Subtropical SST dipole events in the southern Indian Ocean. *Geophysical Research Letters*, *28*(2), pp.327-330.

Bessafi, M. and Wheeler, M.C., 2006. Modulation of south Indian Ocean tropical cyclones by the Madden–Julian oscillation and convectively coupled equatorial waves. *Monthly Weather Review*, *134*(2), pp.638-656.

Boulard, D., Pohl, B., Crétat, J., Vigaud, N. and Pham-Xuan, T., 2013. Downscaling large-scale climate variability using a regional climate model: the case of ENSO over Southern Africa. *Climate dynamics*, *40*(5-6), pp.1141-1168.

Bourke, W., 1974. A multi-level spectral model. I. Formulation and hemispheric integrations. *Monthly Weather Review*, *102*(10), pp.687-701.

Bracco, A., Kucharski, F., Kallummal, R. and Molteni, F., 2004. Internal variability, external forcing and climate trends in multi-decadal AGCM ensembles. *Climate Dynamics*, 23(6), pp.659-678.

Bracco, A., Kucharski, F., Molteni, F., Hazeleger, W. and Severijns, C., 2007. A recipe for simulating the interannual variability of the Asian summer monsoon and its relation with ENSO. *Climate dynamics*, *28*(5), pp.441-460.

Bulić, I.H. and Kucharski, F., 2012. Delayed ENSO impact on spring precipitation over North/Atlantic European region. *Climate dynamics*, *38*(11-12), pp.2593-2612.

Calow, R.C., MacDonald, A.M., Nicol, A.L. and Robins, N.S., 2010. Ground water security and drought in Africa: linking availability, access, and demand. *Groundwater*, *48*(2), pp.246-256.

Chretien, J. P., Anyamba, A., Small, J., Britch, S., Sanchez, J. L., Halbach, A. C., Tucker, C., & Linthicum, K. J. 2015. Global Climate Anomalies and Potential Infectious Disease Risks: 2014-2015. *PLoS currents*, 7.

Christidis, N., Stott, P.A., Scaife, A.A., Arribas, A., Jones, G.S., Copsey, D., Knight, J.R. and Tennant, W.J. 2013. A new HadGEM3-A-based system for attribution of weather-and climate-related extreme events. *Journal of Climate*, *26*(9), pp.2756-2783.

Ciavarella, A., Christidis, N., Andrews, M., Groenendijk, M., Rostron, J., Elkington, M., Burke, C., Lott, F.C. and Stott, P.A. 2018. Upgrade of the HadGEM3-A based attribution system to high resolution and a new validation framework for probabilistic event attribution. *Weather and climate extremes*, *20*, pp.9-32.

ClimateSignals.org. Southern Africa Drought 2015. Available: http://www.climatesignals.org/events/southern-africa-drought-2015

Cook, K.H., 2000. The South Indian convergence zone and interannual rainfall variability over southern Africa. *Journal of Climate*, *13*(21), pp.3789-3804.

Cook, K.H., 2001. A Southern Hemisphere wave response to ENSO with implications for southern Africa precipitation. *Journal of the Atmospheric Sciences*, *58*(15), pp.2146-2162.

Davis, C. 2011. Climate risk and vulnerability: a handbook for Southern Africa.

Davis-Reddy, C.L. and Vincent, K. 2017. Climate Risk and Vulnerability: A Handbook for Southern Africa (2nd Ed), CSIR, Pretoria, South Africa.

Dieppois, B., Rouault, M. and New, M., 2015. The impact of ENSO on Southern African rainfall in CMIP5 ocean atmosphere coupled climate models. *Climate dynamics*, *45*(9-10), pp.2425-2442.

Dogar, M.M., Kucharski, F. and Azharuddin, S., 2017. Study of the global and regional climatic impacts of ENSO magnitude using SPEEDY AGCM. *Journal of Earth System Science*, 126(2), p.30.

Dutra, E., Giuseppe, F.D., Wetterhall, F. and Pappenberger, F., 2013. Seasonal forecasts of droughts in African basins using the Standardized Precipitation Index. *Hydrology and Earth System Sciences*, *17*(6), pp.2359-2373.

Encyclopaedia Britannica. Wind and rainfall patterns of the West African monsoon. Available: https://www.britannica.com/science/West-African-monsoon/images-videos/media/640047/126422

FAO. 2004. Drought impact mitigation and prevention in the Limpopo River basin. Available: http://www.fao.org/docrep/008/y5744e/y5744e00.htm#Contents.

Fauchereau, N., Pohl, B., Reason, C.J.C., Rouault, M. and Richard, Y., 2009. Recurrent daily OLR patterns in the Southern Africa/Southwest Indian Ocean region, implications for South African rainfall and teleconnections. *Climate Dynamics*, *32*(4), pp.575-591.

Feudale, L. and Kucharski, F., 2013. A common mode of variability of African and Indian monsoon rainfall at decadal timescale. *Climate dynamics*, *41*(2), pp.243-254.

FEWS NET, 2016. Illustrating the extent and severity of the 2015-16 drought. *Southern Africa Special Report*. Available: https://fews.net/sites/default/files/documents/reports/FEWS%20NET_Southern%20Africa%202015_16%20Drought%20Map%20Book_20160318_0.pdf

Florenchie, P., Lutjeharms, J.R., Reason, C.J.C., Masson, S. and Rouault, M., 2003. The source of Benguela Niños in the south Atlantic Ocean. *Geophysical Research Letters*, *30*(10).

Fuchs, B.A., Svoboda, M.D., Wilhite, D.A. and Hayes, H.J., 2014. Drought indices for drought risk assessment in a changing climate. *Handbook of Engineering Hydrology. Modeling, Climate Change and Variability*.

Garen, D.C., 1993. Revised surface-water supply index for western United States. *Journal of Water Resources Planning and Management*, *119*(4), pp.437-454.

Gibbs Maher, W.J., 1967. Rainfall deciles as drought indicators/by WJ Gibbs and JV Maher. *Melbourne: Bureau of Meteorology*.

Gillett, N.P., Kell, T.D. and Jones, P.D., 2006. Regional climate impacts of the Southern Annular Mode. *Geophysical Research Letters*, *33*(23).

Goddard, L., & Graham, N. E. 1999. Importance of the Indian Ocean for simulating rainfall anomalies over eastern and southern Africa. *Journal of Geophysical Research:* Atmospheres (1984– 2012), 104(D16), 19099-19116.

Hansingo, K. and Reason, C.J.C., 2009. Modelling the atmospheric response over southern Africa to SST forcing in the southeast tropical Atlantic and southwest subtropical Indian Oceans. *International Journal of Climatology: A Journal of the Royal Meteorological Society*, *29*(7), pp.1001-1012.

Hart, N.C.G., Reason, C.J.C. and Fauchereau, N., 2010. Tropical–extratropical interactions over southern Africa: Three cases of heavy summer season rainfall. *Monthly weather review*, *138*(7), pp.2608-2623.

Hart, N.C., Reason, C.J. and Fauchereau, N., 2013. Cloud bands over southern Africa: seasonality, contribution to rainfall variability and modulation by the MJO. *Climate dynamics*, *41*(5-6), pp.1199-1212.

Hayes, M.J., Svoboda, M.D., Wardlow, B.D., Anderson, M.C. and Kogan, F., 2012. Drought monitoring: Historical and current perspectives.

Held, I.M. and Suarez, M.J., 1994. A proposal for the intercomparison of the dynamical cores of atmospheric general circulation models. *Bulletin of the American Meteorological Society*, *75*(10), pp.1825-1830.

Hirst, A.C. and Hastenrath, S., 1983. Atmosphere-ocean mechanisms of climate anomalies in the Angola-tropical Atlantic sector. *Journal of Physical Oceanography*, *13*(7), pp.1146-1157.

Hoell, A., Funk, C., Magadzire, T., Zinke, J., & Husak, G. 2015. El Niño–Southern Oscillation diversity and Southern Africa teleconnections during Austral Summer. *Climate Dynamics*, 1-17.

Hoell, A., Funk, C., Zinke, J. and Harrison, L., 2017. Modulation of the southern Africa precipitation response to the El Niño Southern Oscillation by the subtropical Indian Ocean dipole. *Climate dynamics*, *48*(7-8), pp.2529-2540.

Howard, E. and Washington, R., 2018. Characterizing the synoptic expression of the Angola low. *Journal of Climate*, *31*(17), pp.7147-7165.

Johnson, N. C. 2013. How many ENSO flavors can we distinguish?*. Journal of Climate, 26(13), 4816-4827.

Joubert, A.M. and Hewitson, B.C., 1997. Simulating present and future climates of southern Africa using general circulation models. *Progress in physical geography*, *21*(1), pp.51-78.

Kao, H. Y., & Yu, J. Y. 2009. Contrasting eastern-Pacific and central-Pacific types of ENSO. *Journal of Climate*, *22*(3), 615-632.

Karl, T.R., 1986. The sensitivity of the Palmer drought severity index and Palmer's Z-index to their calibration coefficients including potential evapotranspiration. *Journal of Climate and Applied Meteorology*, *25*(1), pp.77-86.

Karl, T.R. and Koscielny, A.J., 1982. Drought in the united states: 1895–1981. *Journal of Climatology*, *2*(4), pp.313-329.

Klutse, N.A.B., Abiodun, B.J., Hewitson, B.C., Gutowski, W.J. and Tadross, M.A., 2016. Evaluation of two GCMs in simulating rainfall inter-annual variability over Southern Africa. *Theoretical and applied climatology*, *123*(3-4), pp.415-436.

Kucharski, F., Bracco, A., Barimalala, R. and Yoo, J.H., 2011. Contribution of the east–west thermal heating contrast to the South Asian Monsoon and consequences for its variability. *Climate dynamics*, *37*(3-4), pp.721-735.

Kucharski, F., Bracco, A., Yoo, J.H., Tompkins, A.M., Feudale, L., Ruti, P. and Dell'Aquila, A., 2009. A Gill–Matsuno-type mechanism explains the tropical Atlantic influence on African and Indian monsoon rainfall. *Quarterly Journal of the Royal Meteorological Society: A journal of the*

atmospheric sciences, applied meteorology and physical oceanography, *135*(640), pp.569-579.

Kucharski, F., Molteni, F., King, M.P., Farneti, R., Kang, I.S. and Feudale, L., 2013. On the need of intermediate complexity general circulation models: A "SPEEDY" example. *Bulletin of the American Meteorological Society*, *94*(1), pp.25-30.

Kucharski, F., Molteni, F. and Bracco, A., 2006. Decadal interactions between the western tropical Pacific and the North Atlantic Oscillation. *Climate dynamics*, 26(1), pp.79-91.

Kucharski, F., Zeng, N. and Kalnay, E., 2013. A further assessment of vegetation feedback on decadal Sahel rainfall variability. *Climate dynamics*, *40*(5-6), pp.1453-1466.

Landman, W.A. and Beraki, A., 2012. Multi-model forecast skill for mid-summer rainfall over southern Africa. *International Journal of Climatology*, *32*(2), pp.303-314.

Landman, W.A. and Goddard, L., 2002. Statistical recalibration of GCM forecasts over southern Africa using model output statistics. *Journal of Climate*, *15*(15), pp.2038-2055.

Larkin, N. K., & Harrison, D. E. 2005. Global seasonal temperature and precipitation anomalies during El Niño autumn and winter. *Geophysical Research Letters*, *32*(16).

Li, Y., Kalnay, E., Motesharrei, S., Rivas, J., Kucharski, F., Kirk-Davidoff, D., Bach, E. and Zeng, N., 2018. Climate model shows large-scale wind and solar farms in the Sahara increase rain and vegetation. *Science*, *361*(6406), pp.1019-1022.

Liebmann, B., Hendon, H.H. and Glick, J.D., 1994. The relationship between tropical cyclones of the western Pacific and Indian Oceans and the Madden-Julian oscillation. *Journal of the Meteorological Society of Japan. Ser. II*, *72*(3), pp.401-412.

Lindesay, J.A., 1988. South African rainfall, the Southern Oscillation and a Southern Hemisphere semi-annual cycle. *Journal of Climatology*, *8*(1), pp.17-30.

Macron, C., Pohl, B., Richard, Y. and Bessafi, M., 2014. How do tropical temperate troughs form and develop over southern Africa?. *Journal of Climate*, *27*(4), pp.1633-1647.

Malherbe, J., Dieppois, B., Maluleke, P., Van Staden, M. and Pillay, D.L., 2016. South African droughts and decadal variability. *Natural Hazards*, *80*(1), pp.657-681.

Madden, R.A. and Julian, P.R. 1971. Detection of a 40–50 day oscillation in the zonal wind in the tropical Pacific. *Journal of the atmospheric sciences*, *28*(5), pp.702-708.

Manatsa, D., Chingombe, W., Matsikwa, H. and Matarira, C.H., 2008. The superior influence of Darwin Sea level pressure anomalies over ENSO as a simple drought predictor for Southern Africa. *Theoretical and applied climatology*, *92*(1-2), pp.1-14.

Manatsa, D., Mukwada, G., Siziba, E. and Chinyanganya, T., 2010. Analysis of multidimensional aspects of agricultural droughts in Zimbabwe using the Standardized Precipitation Index (SPI). *Theoretical and Applied Climatology*, *102*(3-4), pp.287-305.

Manatsa, D., Mushore, T. and Lenouo, A., 2017. Improved predictability of droughts over southern Africa using the standardized precipitation evapotranspiration index and ENSO. *Theoretical and applied climatology*, *127*(1-2), pp.259-274.

Manhique, A.J., Reason, C.J.C., Rydberg, L. and Fauchereau, N., 2011. ENSO and Indian Ocean sea surface temperatures and their relationships with tropical temperate troughs over Mozambique and the Southwest Indian Ocean. *International Journal of Climatology*, *31*(1), pp.1-13.

Masih, I., Maskey, S., Mussá, F.E.F. and Trambauer, P., 2014. A review of droughts on the African continent: a geospatial and long-term perspective. *Hydrology and Earth System Sciences*, *18*(9), pp.3635-3649.

Mason, S.J. and Joubert, A.M., 1997. Simulated changes in extreme rainfall over southern Africa. *International Journal of Climatology: A Journal of the Royal Meteorological Society*, *17*(3), pp.291-301.

McKee, T.B., Doesken, N.J. and Kleist, J., 1993, January. The relationship of drought frequency and duration to time scales. In *Proceedings of the 8th Conference on Applied Climatology* (Vol. 17, No. 22, pp. 179-183). Boston, MA: American Meteorological Society.

Mendicino, G., Senatore, A. and Versace, P., 2008. A Groundwater Resource Index (GRI) for drought monitoring and forecasting in a Mediterranean climate. *Journal of Hydrology*, *357*(3-4), pp.282-302.

Meque, A. and Abiodun, B.J., 2015. Simulating the link between ENSO and summer drought in Southern Africa using regional climate models. *Climate Dynamics*, *44*(7-8), pp.1881-1900.

Mishra, A.K. and Singh, V.P., 2010. A review of drought concepts. *Journal of hydrology*, *391*(1-2), pp.202-216.

Molteni, F., 2003. Atmospheric simulations using a GCM with simplified physical

parametrizations. I: Model climatology and variability in multi-decadal experiments. *Climate Dynamics*, 20(2), pp.175-191.

Naik, M. and Abiodun, B.J., 2016. Potential impacts of forestation on future climate change in Southern Africa. *International Journal of Climatology*, *36*(14), pp.4560-4576.

Narasimhan, B. and Srinivasan, R., 2005. Development and evaluation of Soil Moisture Deficit Index (SMDI) and Evapotranspiration Deficit Index (ETDI) for agricultural drought monitoring. *Agricultural and Forest Meteorology*, *133*(1-4), pp.69-88.

Nicholson, S.E., 2000. The nature of rainfall variability over Africa on time scales of decades to millenia. *Global and planetary change*, *26*(1-3), pp.137-158.

Nicholson, S.E., 2011. *Dryland climatology*. Cambridge University Press.

Nicholson, S.E. and Entekhabi, D., 1987. Rainfall variability in equatorial and southern Africa: Relationships with sea surface temperatures along the southwestern coast of Africa. *Journal of Climate and Applied Meteorology*, *26*(5), pp.561-578.

Nicholson, S.E. and Kim, J., 1997. The relationship of the El Niño–Southern oscillation to African rainfall. *International Journal of Climatology*, *17*(2), pp.117-135.

Nicholson, S.E. and Selato, J.C., 2000. The influence of La Niña on African rainfall. *International Journal of Climatology: A Journal of the Royal Meteorological Society*, *20*(14), pp.1761-1776.

Ntale, H.K. and Gan, T.Y., 2003. Drought indices and their application to East Africa. *International Journal of Climatology*, *23*(11), pp.1335-1357.

Palmer, W.C., 1965. Meteorological drought, weather bureau research paper no. 45. *Washington, DC US Dep Commer*.

Palmer, W.C., 1968. Keeping track of crop moisture conditions, nationwide: The new crop moisture index.

Pohl, B., Fauchereau, N., Reason, C.J.C. and Rouault, M., 2010. Relationships between the Antarctic Oscillation, the Madden–Julian oscillation, and ENSO, and consequences for rainfall analysis. *Journal of Climate*, *23*(2), pp.238-254.

Pohl, B., Richard, Y. and Fauchereau, N., 2007. Influence of the Madden–Julian oscillation on

southern African summer rainfall. *Journal of Climate*, *20*(16), pp.4227-4242.

Ratna, S.B., Behera, S., Ratnam, J.V., Takahashi, K. and Yamagata, T., 2013. An index for tropical temperate troughs over southern Africa. *Climate dynamics*, *41*(2), pp.421-441.

Ratnam, J.V., Behera, S.K., Masumoto, Y., Takahashi, K. and Yamagata, T., 2012. Anomalous climatic conditions associated with the El Niño Modoki during boreal winter of 2009. *Climate dynamics*, *39*(1-2), pp.227-238.

Ratnam, J.V., Behera, S.K., Masumoto, Y. and Yamagata, T., 2014. Remote effects of El Niño and Modoki events on the austral summer precipitation of southern Africa. *Journal of Climate*, *27*(10), pp.3802-3815.

Reason, C.J.C., 2001. Subtropical Indian Ocean SST dipole events and southern African rainfall. *Geophysical Research Letters*, *28*(11), pp.2225-2227.

Reason, C.J.C., 2002. Sensitivity of the southern African circulation to dipole sea-surface temperature patterns in the south Indian Ocean. *International Journal of Climatology*, *22*(4), pp.377-393.

Reason, C. J. C., Allan, R. J., Lindesay, J. A., & Ansell, T. J. 2000. ENSO and climatic signals across the Indian Ocean basin in the global context: Part I, Interannual composite patterns. *International Journal of Climatology*, *20*(11), 1285-1327.

Reason, C. J. C., & Jagadheesha, D. 2005. A model investigation of recent ENSO impacts over southern Africa. *Meteorology and Atmospheric Physics*,*89*(1-4), 181-205.

Reason, C.J.C., Jagadheesha, D. and Tadross, M., 2003. A model investigation of inter-annual winter rainfall variability over southwestern South Africa and associated ocean-atmosphere interaction. *South African journal of science*, *99*(1-2), pp.75-80.

Reason, C.J.C., Landman, W. and Tennant, W., 2006. Seasonal to decadal prediction of southern African climate and its links with variability of the Atlantic Ocean. *Bulletin of the American Meteorological Society*, *87*(7), pp.941-956.

Reason, C.J.C. and Rouault, M., 2005. Links between the Antarctic Oscillation and winter rainfall over western South Africa. *Geophysical research letters*, *32*(7).

Reason, C.J. and Smart, S., 2015. Tropical south east Atlantic warm events and associated

rainfall anomalies over southern Africa. *Frontiers in Environmental Science*, *3*, p.24.

Richard, Y., Fauchereau, N., Poccard, I., Rouault, M. and Trzaska, S., 2001. 20th century droughts in southern Africa: spatial and temporal variability, teleconnections with oceanic and atmospheric conditions. *International Journal of Climatology*, *21*(7), pp.873-885.

Richard, Y., Trzaska, S., Roucou, P. and Rouault, M., 2000. Modification of the southern African rainfall variability/ENSO relationship since the late 1960s. *Climate Dynamics*, *16*(12), pp.883-895.

Rouault, M., Florenchie, P., Fauchereau, N. and Reason, C.J., 2003. South East tropical Atlantic warm events and southern African rainfall. *Geophysical Research Letters*, *30*(5).

Rouault, M., Illig, S., Lübbecke, J. and Koungue, R.A.I., 2018. Origin, development and demise of the 2010–2011 Benguela Niño. *Journal of Marine Systems*, *188*, pp.39-48.

Rouault, M. and Richard, Y., 2005. Intensity and spatial extent of droughts in southern Africa. *Geophysical Research Letters*, *32*(15).

SADC, 2016. Regional Situation Update on the El Niño-Induced Drought. *SADC Regional Situation Update*. Available: https://www.sadc.int/files/9514/7403/9132/SADC_Regional_Situation_Update_No-2_16-09-2016.pdf

SADC, 2018. Synthesis Report on the State of Food and Nutrition Security and Vulnerability I Southern Africa. *SADC Regional Vulnerability Assessment & Analysis (RVAA)* Available: https://www.sadc.int/files/1715/3114/9162/2018_SADC_RVAA_Synthesis_Report__060718.pdf

Saji, N.H., Goswami, B.N., Vinayachandran, P.N. and Yamagata, T., 1999. A dipole mode in the tropical Indian Ocean. *Nature*, *401*(6751), p.360.

Saji, N.H. and Yamagata, T., 2003. Possible impacts of Indian Ocean dipole mode events on global climate. *Climate Research*, *25*(2), pp.151-169.

Shafer, B.A. and Dezman, L.E., 1982. Development of surface water supply index-a drought severity indicator for Colorado. In *Proc. Western Snow Conference* (pp. 164-175).

Shannon, L.V., Boyd, A.J., Brundrit, G.B. and Taunton-Clark, J., 1986. On the existence of an El Niño-type phenomenon in the Benguela system. *Journal of Marine Research*, *44*(3), pp.495-520.

Shukla, S. and Wood, A.W., 2008. Use of a standardized runoff index for characterizing hydrologic drought. *Geophysical research letters*, *35*(2).

Shongwe, M.E., Van Oldenborgh, G.J., Van Den Hurk, B.J.J.M., De Boer, B., Coelho, C.A.S. and Van Aalst, M.K., 2009. Projected changes in mean and extreme precipitation in Africa under global warming. Part I: Southern Africa. *Journal of climate*, *22*(13), pp.3819-3837.

Stone, D.A., Christidis, N., Folland, C., Perkins-Kirkpatrick, S., Perlwitz, J., Shiogama, H., Wehner, M.F., Wolski, P., Cholia, S., Krishnan, H., Murray, D., Angélil, O., Beyerle, U., Ciavarella, A., Dittus, A., Quan, X. and Tadross, M. 2019. Experiment design of the international CLIVAR C20C+ detection and attribution project. *Weather and Climate Extremes*, *24*, p.100206.

Stone, D.A., Risser, M.D., Angélil, O.M., Wehner, M.F., Cholia, S., Keen, N., Krishnan, H., O'Brien, T.A. and Collins, W.D. 2018. A basis set for exploration of sensitivity to prescribed ocean conditions for estimating human contributions to extreme weather in CAM5. 1-1degree. *Weather and climate extremes*, *19*, pp.10-19.

Strengers, B.J., Müller, C., Schaeffer, M., Haarsma, R.J., Severijns, C., Gerten, D., Schaphoff, S., van den Houdt, R. and Oostenrijk, R., 2010. Assessing 20th century climate–vegetation feedbacks of land-use change and natural vegetation dynamics in a fully coupled vegetation–climate model. *International Journal of Climatology*, *30*(13), pp.2055-2065.

Thompson, D.W. and Wallace, J.M., 2000. Annular modes in the extratropical circulation. Part I: Month-to-month variability. *Journal of climate*, *13*(5), pp.1000-1016.

Trambauer, P., Maskey, S., Werner, M., Pappenberger, F., Van Beek, L.P.H. and Uhlenbrook, S., 2014. Identification and simulation of space–time variability of past hydrological drought events in the Limpopo River basin, southern Africa. *Hydrology and Earth System Sciences*, *18*(8), pp.2925-2942.

Trenberth, K.E., 1997. The definition of el Niño. *Bulletin of the American Meteorological Society*, *78*(12), pp.2771-2778.

Tyson, P. D., & Preston-Whyte, R. A. 2000. Weather and Climate of Southern Africa. Oxford University Press.

Ujeneza, E.L. and Abiodun, B.J., 2015. Drought regimes in Southern Africa and how well GCMs simulate them. *Climate Dynamics*, *44*(5-6), pp.1595-1609.

UNISDR, 2009. Drought Risk Reduction Framework and Practices: Contributing to the Implementation of the Hyogo Framework for Action. United Nations secretariat of the International Strategy for Disaster Reduction (UNISDR), Geneva, Switzerland, 213 pp.

USGS, 2016. Droughts: Questions and Answers. U.S. Geological Survey. Available: http://ga.water.usgs.gov/edu/qadroughts.html

Vicente-Serrano, S.M., Beguería, S. and López-Moreno, J.I., 2010. A multiscalar drought index sensitive to global warming: the standardized precipitation evapotranspiration index. *Journal of climate*, *23*(7), pp.1696-1718.

Vogel, C.H. and Drummond, J.H., 1993. Dimensions of drought: South African case studies. *GeoJournal*, *30*(1), pp.93-98.

Wang, G. and Eltahir, E.A., 2000a. Ecosystem dynamics and the Sahel drought. *Geophysical Research Letters*, *27*(6), pp.795-798.

Wang, G. and Eltahir, E.A., 2000b. Role of vegetation dynamics in enhancing the low-frequency variability of the Sahel rainfall. *Water Resources Research*, *36*(4), pp.1013-1021.

Wang, Q., Wu, J., Lei, T., He, B., Wu, Z., Liu, M., Mo, X., Geng, G., Li, X., Zhou, H. and Liu, D., 2014. Temporal-spatial characteristics of severe drought events and their impact on agriculture on a global scale. *Quaternary International*, *349*, pp.10-21.

Wells, N., Goddard, S. and Hayes, M.J., 2004. A self-calibrating Palmer drought severity index. *Journal of Climate*, *17*(12), pp.2335-2351.

Wilhite, D.A., 2000. Drought as a natural hazard: concepts and definitions.

Wilhite, D.A. and Glantz, M.H., 1985. Understanding: the drought phenomenon: the role of definitions. *Water international*, *10*(3), pp.111-120.

Wilson, A.B., Bromwich, D.H., Hines, K.M. and Wang, S.H., 2014. El Niño flavors and their simulated impacts on atmospheric circulation in the high southern latitudes. *Journal of Climate*, *27*(23), pp.8934-8955.

Yadav, R.K., Yoo, J.H., Kucharski, F. and Abid, M.A., 2010. Why is ENSO influencing northwest India winter precipitation in recent decades?. *Journal of Climate*, *23*(8), pp.1979-1993.

Yeh, S.W., Wang, X., Wang, C. and Dewitte, B., 2015. On the relationship between the North Pacific climate variability and the central Pacific El Niño. *Journal of Climate*, *28*(2), pp.663-677.

Yuan, C., Tozuka, T., Landman, W. A., & Yamagata, T. 2014. Dynamical seasonal prediction of Southern African summer precipitation. *Climate dynamics*, *42*(11-12), 3357-3374.

Zeng, N., Neelin, J.D., Lau, K.M. and Tucker, C.J., 1999. Enhancement of interdecadal climate variability in the Sahel by vegetation interaction. *Science*, *286*(5444), pp.1537-1540.

Zeng, N. and Yoon, J., 2009. Expansion of the world's deserts due to vegetation-albedo feedback under global warming. *Geophysical Research Letters*, *36*(17).

Zhao, T. and Dai, A., 2015. The magnitude and causes of global drought changes in the twenty-first century under a low–moderate emissions scenario. *Journal of climate*, *28*(11), pp.4490-4512.

Zou, X., Zhai, P. and Zhang, Q., 2005. Variations in droughts over China: 1951–2003. *Geophysical Research Letters*, *32*(4).

This research used science gateway resources of the National Energy Research Scientific Computing Center, a DOE Office of Science User Facility supported by the Office of Science of the U.S. Department of Energy under Contract No. DE-AC02-05CH11231.